CALIFA, the Calar Alto Legacy Integral Field Area survey. III. Second public data release

García-Benito, R.; Zibetti, S.; Sánchez, S. F.; Husemann, B.; de Amorim, A. L.; Castillo-Morales, A.; Cid Fernandes, R.; Ellis, S. C.; Falcón-Barroso, J.; Galbany, L.

Published in:
Astronomy and astrophysics

DOI:
10.1051/0004-6361/201425080

Publication date:
2015

A&A 576, A135 (2015)
DOI: 10.1051/0004-6361/201425080

Astronomy & Astrophysics

CALIFA, the Calar Alto Legacy Integral Field Area survey

III. Second public data release⋆,⋆⋆

R. García-Benito[1], S. Zibetti[2], S. F. Sánchez[3], B. Husemann[4], A. L. de Amorim[5], A. Castillo-Morales[6], R. Cid Fernandes[5], S. C . Ellis[7], J. Falcón-Barroso[8,9], L. Galbany[10,11], A. Gil de Paz[6], R. M. González Delgado[1], E. A. D. Lacerda[5], R. López-Fernandez[1], A. de Lorenzo-Cáceres[12], M. Lyubenova[13,14], R. A. Marino[15], D. Mast[16], M. A. Mendoza[1], E. Pérez[1], N. Vale Asari[5], J. A. L. Aguerri[8,9], Y. Ascasibar[17], S. Bekeraitė[18], J. Bland-Hawthorn[19], J. K. Barrera-Ballesteros[8,9], D. J. Bomans[20,21], M. Cano-Díaz[3], C. Catalán-Torrecilla[6], C. Cortijo[1], G. Delgado-Inglada[3], M. Demleitner[22], R.-J. Dettmar[20,21], A. I. Díaz[17], E. Florido[13,33], A. Gallazzi[2,24], B. García-Lorenzo[8,9], J. M. Gomes[25], L. Holmes[26], J. Iglesias-Páramo[1,27], K. Jahnke[14], V. Kalinova[28], C. Kehrig[1], R. C. Kennicutt Jr[29], Á. R. López-Sánchez[7,30], I. Márquez[1], J. Masegosa[1], S. E. Meidt[14], J. Mendez-Abreu[12], M. Mollá[31], A. Monreal-Ibero[32], C. Morisset[3], A. del Olmo[1], P. Papaderos[25], I. Pérez[23,33], A. Quirrenbach[34], F. F. Rosales-Ortega[35], M. M. Roth[18], T. Ruiz-Lara[23,33], P. Sánchez-Blázquez[17], L. Sánchez-Menguiano[1,23], R. Singh[14], K. Spekkens[26], V. Stanishev[36,37], J. P. Torres-Papaqui[38], G. van de Ven[14], J. M. Vilchez[1], C. J. Walcher[18], V. Wild[12], L. Wisotzki[18], B. Ziegler[39], J. Alves[39], D. Barrado[40], J. M. Quintana[1], and J. Aceituno[27]

(Affiliations can be found after the references)

Received 29 September 2014 / Accepted 24 February 2015

ABSTRACT

This paper describes the Second Public Data Release (DR2) of the Calar Alto Legacy Integral Field Area (CALIFA) survey. The data for 200 objects are made public, including the 100 galaxies of the First Public Data Release (DR1). Data were obtained with the integral-field spectrograph PMAS/PPak mounted on the 3.5 m telescope at the Calar Alto observatory. Two different spectral setups are available for each galaxy, (i) a low-resolution V500 setup covering the wavelength range 3745–7500 Å with a spectral resolution of 6.0 Å (FWHM); and (ii) a medium-resolution V1200 setup covering the wavelength range 3650–4840 Å with a spectral resolution of 2.3 Å (FWHM). The sample covers a redshift range between 0.005 and 0.03, with a wide range of properties in the color–magnitude diagram, stellar mass, ionization conditions, and morphological types. All the cubes in the data release were reduced with the latest pipeline, which includes improved spectrophotometric calibration, spatial registration, and spatial resolution. The spectrophotometric calibration is better than 6% and the median spatial resolution is 2.″4. In total, the second data release contains over 1.5 million spectra.

Key words. surveys – techniques: spectroscopic – galaxies: general

1. Introduction

The Calar Alto Legacy Integral Field Area (CALIFA) survey (Sánchez et al. 2012a, hereafter S12) is an ongoing large project of the Centro Astronómico Hispano-Alemán at the Calar Alto observatory (Almería, Spain) to obtain spatially resolved spectra for 600 galaxies in the local Universe by means of integral field spectroscopy (IFS). The CALIFA observations started in June 2010 with the Potsdam Multi Aperture Spectrograph (PMAS, Roth et al. 2005), mounted on the 3.5 m telescope, utilizing the large hexagonal field-of-view (FoV) offered by the PPak fiber bundle (Verheijen et al. 2004; Kelz et al. 2006). Each galaxy is observed using two different setups: one at intermediate spectral resolution (V1200, $R \sim 1650$) and the other at low resolution (V500, $R \sim 850$). A diameter-selected sample of 939 galaxies was drawn from the 7th data release of the Sloan Digital Sky Survey (SDSS DR7, Abazajian et al. 2009), which is described in Walcher et al. (2014, hereafter W14). From this mother sample, the 600 target galaxies are randomly selected.

Combining the techniques of imaging and spectroscopy through optical IFS provides a more comprehensive view of individual galaxy properties than any traditional survey. CALIFA-like observations were collected during the feasibility studies (Mármol-Queraltó et al. 2011; Viironen et al. 2012) and the PPak IFS Nearby Galaxy Survey (PINGS, Rosales-Ortega et al. 2010), a predecessor of this survey. First results based on those data sets already explored their information content (e.g., Sánchez et al. 2011, 2012b; Rosales-Ortega et al. 2011, 2012; Alonso-Herrero et al. 2012). The CALIFA survey can therefore be expected to make a substantial contribution to our understanding of galaxy evolution in various aspects, including (i) the relative importance and consequences of merging and secular processes; (ii) the evolution of galaxies across the color–magnitude diagram; (iii) the effects of the environment on galaxies; (iv) the AGN-host galaxy

⋆ Based on observations collected at the Centro Astronómico Hispano Alemán (CAHA) at Calar Alto, operated jointly by the Max-Planck-Institut für Astronomie (MPIA) and the Instituto de Astrofísica de Andalucía (CSIC).

⋆⋆ The second data release is available at http://califa.caha.es/DR2

connection; (v) the internal dynamical processes in galaxies; and (vi) the global and spatially resolved star formation history and chemical enrichment of various galaxy types.

Compared with previous IFS surveys, e.g., Atlas3D (Cappellari et al. 2011) or the Disk Mass Survey (DMS) (Bershady et al. 2010), CALIFA covers a much wider range of morphological types over a large range of masses, sampling the entire color–magnitude diagram for $M_r > -19$ mag. While the recently started SAMI (Croom et al. 2012; Bryant et al. 2015) and MaNGA (Law & MaNGA Team 2014) surveys have a broad scope similar to CALIFA and aim to build much larger samples, CALIFA still has an advantage in terms of spatial coverage and sampling. For 50% of the galaxies, CALIFA provides data out to 3.5 r_e, and for 80% out to 2.5 r_e. At the same time, the spatial resolution of ~1 kpc is typically better than in either SAMI or MaNGA, revealing several of the most relevant structures in galaxies (spiral arms, bars, bulges, giant H II regions, etc.). The spectral resolution of CALIFA is lower than these two surveys in the red wavelength range, but is comparable for the blue wavelength range.

So far, a number of science goals have been addressed using the data from the CALIFA survey: (i) new techniques have been developed to understand the spatially resolved star formation histories (SFH) of galaxies (Cid Fernandes et al. 2013, 2014). We found solid evidence that mass-assembly in the typical galaxies happens from the inside-out (Pérez et al. 2013). The SFH and metal enrichment of bulges and early-type galaxies are fundamentally related to the total stellar mass, while for disk galaxies it is more closely related to the local stellar mass density (González Delgado et al. 2014b,a); (ii) we developed new tools to detect and extract the spectra of H II regions (Sánchez et al. 2012b), building the largest catalog currently available (~6000 H II regions and aggregations). This catalog has been used to define a new oxygen abundance calibrator, anchored to electron temperature measurements (Marino et al. 2013). From these, we explored the dependence of the mass-metallicity relation with star formation rate (Sánchez et al. 2013), and the local mass-metallicity relation (Rosales-Ortega et al. 2012). We found that all galaxies in our sample present a common gas-phase oxygen abundance radial gradient with a similar slope, when normalized to the effective radius (Sánchez et al. 2014). This agrees with an inside-out scenario for galaxy growth. This characteristic slope is independent of the properties of the galaxies, and, in particular, of the presence or absence of a bar, contrary to previous results. More recently, this result has been confirmed by the analysis of the stellar abundance gradient in the same sample (Sánchez-Blázquez et al. 2014); (iii) we explored the origin of the low intensity, LINER-like, ionized gas in galaxies. These regions are clearly not related to star formation activity, or to AGN activity. They are probably most closely related to post-AGB ionization in many cases (Kehrig et al. 2012; Singh et al. 2013; Papaderos et al. 2013); (iv) we explored the aperture and resolution effects on the data. The CALIFA survey provides a unique tool to understand the aperture and resolution effects in larger single-fiber (e.g., SDSS) and IFS surveys (e.g., MaNGA, SAMI). We explored the effects of the dilution of the signal in different gas and stellar population properties (Mast et al. 2014), and proposed a new empirical aperture correction for the SDSS data (Iglesias-Páramo et al. 2013); (v) we analyzed the local properties of the ionized gas and stellar population of galaxies where supernovae (SNe) have exploded. Core collapse SNe are found closer to younger stellar populations, while SNe Ia show no correlation to stellar age (Galbany et al. 2014); (vi) CALIFA is the first IFS survey that allows gas and stellar kinematic studies for all morphologies with sufficient spectroscopic resolution to study (a) the kinematics of the ionized gas (García-Lorenzo et al. 2015); (b) the effects of bars in the kinematics of galaxies (Barrera-Ballesteros et al. 2014); (c) the effects of the interaction stage on the kinematic signatures (Barrera-Ballesteros et al., in prep.); (d) the bar pattern speeds in late-type galaxies (Aguerri et al. 2015); (e) the measurements of the angular momentum of galaxies to previously unexplored ranges of morphology and ellipticity (Falcón-Barroso et al., in prep.); and (vii) we explored the effects of a first stage merger on the gas and stellar kinematics, star formation activity and stellar populations of the Mice merging galaxies (Wild et al. 2014).

In this article, we introduce the second data release (DR2) of CALIFA, which grants public access to high-quality data for a set of 200 galaxies (400 datacubes). All the cubes in the data release have been reduced with the latest pipeline, which includes improved spectrophotometric calibration, spatial registration, and spatial resolution. This DR supersedes and increases he amount of data delivered in DR1 (Husemann et al. 2013, hereafter H13) by a factor of two.

The DR1 opened CALIFA to the community, and allowed for the exploration of several different scientific avenues not addressed by the collaboration (e.g., Holwerda & Keel 2013; De Geyter et al. 2014; Martínez-García et al. 2014; Davies et al. 2014). The properties of the galaxies in the DR2 sample are summarized in Sect. 2. We describe the observing strategy and setup (Sect. 3), processing (Sect. 4), structure (Sect. 5), and data (Sect. 6), which comprise essential information for any scientific analysis of the distributed CALIFA data. Several interfaces to access the CALIFA DR2 data are explained in Sect. 7.

2. The CALIFA DR2 sample

The CALIFA "mother sample" (MS) consists of 939 galaxies drawn from SDSS DR7. The main criteria for the target selection are: angular isophotal diameter ($45'' < isoA_r < 79.2''$) of the galaxies[1]; redshift range $0.005 < z < 0.03$; cut in Galactic latitude to exclude the Galactic plane ($|b| > 20°$); flux limit of $petroMag_r < 20$; and declination limit to $\delta > 7°$. Redshift limits were imposed so that the sample would not be dominated by dwarf galaxies and to keep relevant spectral features observable within a fixed instrumental spectral setup. Redshift information was taken from SIMBAD for all galaxies where SDSS DR7 spectra were unavailable. The cut in declination was chosen to reduce problems due to differential atmospheric refraction (DAR) and PMAS flexure issues, but was not applied to the SDSS Southern area because of the sparsity of objects in this region. A comprehensive characterization of the CALIFA MS and a detailed evaluation of the selection effects implied by the chosen criteria is provided in W14. From the CALIFA MS, 600 galaxies are randomly selected for observation, based purely on visibility.

The 200 DR2 galaxies, which include the first 100 galaxies of DR1, were observed in both spectral setups between the start of observations in June 2010 and December 2013. We list these galaxies in Table 1 together with their primary characteristics. The distribution of galaxies in the sky follows the underlying SDSS footprint (Fig. 1). The number of galaxies in DR2 is not homogeneous as a function of right ascension, α(J2000),

[1] The $isoA_r$ parameter is the isophote major axis at 25 mag per square arcsecond in the r-band. For the meaning of other SDSS pipeline parameters, refer to the DR7 webpage: http://skyserver.sdss.org/dr7/en/help/browser/browser.asp

Table 1. CALIFA DR2 galaxies and their characteristics.

Name	ID[a]	α(J2000)[b]	δ(J2000)[b]	z[c]	m_g[d]	m_z[d]	$m_u - m_z$[d]	Type[e]	Bar[f]	b/a[g]
IC 5376	001	00:01:19.779	+34:31:32.409	0.0168	14.24	12.60	3.48	Sb	A	0.27
UGC 00005	002	00:03:05.643	–01:54:49.804	0.0243	13.88	12.53	2.95	Sbc	A	0.54
NGC 7819	003	00:04:24.505	+31:28:19.228	0.0167	14.06	13.01	2.12	Sc	A	0.53
IC 1528	005	00:05:05.377	–07:05:36.204	0.0128	13.46	12.52	2.43	Sbc	AB	0.36
UGC 00036	007	00:05:13.882	+06:46:19.306	0.0210	14.12	12.46	3.55	Sab	AB	0.60
NGC 0001	008	00:07:15.860	+27:42:29.096	0.0151	13.46	12.01	2.97	Sbc	A	0.80
NGC 0036	010	00:11:22.298	+06:23:21.667	0.0203	13.46	12.01	3.23	Sb	B	0.65
MCG-02-02-030	013	00:30:07.309	–11:06:49.066	0.0118	13.41	12.08	2.91	Sb	AB	0.34
UGC 00312	014	00:31:23.922	+08:28:00.232	0.0145	13.76	13.07	1.52	Sd	B	0.35
UGC 00335NED02	017	00:33:57.323	+07:16:05.781	0.0183	14.27	12.82	3.42	E4(x)	A	0.63
NGC 0169	022	00:36:51.608	+23:59:27.501	0.0154	14.04	11.74	4.50	Sab(x)	A	0.42
NGC 0171	023	00:37:21.552	–19:56:03.210	0.0131	13.21	11.73	3.29	Sb	B	0.63
NGC 0180	025	00:37:57.703	+08:38:06.588	0.0177	13.51	11.98	3.00	Sb	B	0.64
NGC 0192	026	00:39:13.414	+00:51:50.968	0.0140	13.37	11.72	3.23	Sab	AB	0.31
NGC 0216	027	00:41:27.170	–21:02:40.826	0.0052	13.55	12.78	1.78	Sd	A	0.27
NGC 0237	030	00:43:27.841	–00:07:29.747	0.0139	13.52	12.38	2.44	Sc	B	0.57
IC 1652	037	01:14:56.277	+31:56:54.606	0.0173	14.08	12.72	3.13	S0a	A	0.31
NGC 0444	039	01:15:49.562	+31:04:50.245	0.0161	14.47	13.48	2.20	Scd	A	0.24
UGC 00809	040	01:15:51.837	+33:48:38.532	0.0140	14.81	13.74	2.52	Scd	A	0.19
UGC 00841	041	01:19:10.028	+33:01:50.248	0.0186	14.91	13.73	2.55	Sbc	A	0.25
NGC 0477	042	01:21:20.483	+40:29:17.332	0.0196	14.43	13.09	2.66	Sbc	AB	0.66
IC 1683	043	01:22:38.929	+34:26:13.654	0.0162	14.11	12.63	2.98	Sb	AB	0.59
NGC 0499	044	01:23:11.496	+33:27:36.683	0.0146	12.76	11.19	3.49	E5	A	0.61
NGC 0496	045	01:23:11.595	+33:31:45.386	0.0201	13.92	12.93	2.25	Scd	A	0.58
NGC 0528	050	01:25:33.571	+33:40:17.198	0.0161	13.51	11.89	3.58	S0	A	0.49
UGC 01057	053	01:28:53.253	+13:47:37.674	0.0212	14.54	13.26	2.66	Sc	AB	0.30
NGC 0774	072	01:59:34.729	+14:00:29.536	0.0154	13.52	11.88	3.50	S0	A	0.72
NGC 0776	073	01:59:54.525	+23:38:39.392	0.0164	13.52	12.06	3.19	Sb	B	0.69
NGC 0810	076	02:05:28.562	+13:15:05.867	0.0257	13.70	11.93	3.74	E5(x)	A	0.69
NGC 0825	077	02:08:32.329	+06:19:25.200	0.0113	13.63	12.04	3.29	Sa	A	0.33
UGC 01938	088	02:28:22.137	+23:12:52.655	0.0213	14.70	13.31	2.90	Sbc	AB	0.25
NGC 1056	100	02:42:48.312	+28:34:26.961	0.0052	13.00	11.41	3.02	Sa	A	0.57
UGC 02222	103	02:45:09.676	+32:59:22.935	0.0166	13.76	12.29	3.32	S0a(x)	AB	0.51
UGC 02229	104	02:45:27.567	+00:54:51.657	0.0244	14.16	12.48	3.49	S0a(x)	A	0.57
UGC 02403	115	02:55:57.257	+00:41:33.378	0.0137	14.15	12.41	3.44	Sb	B	0.28
NGC 1349	127	03:31:27.512	+04:22:51.241	0.0220	13.34	11.80	3.45	E6	A	0.89
NGC 1542	131	04:17:14.172	+04:46:54.239	0.0125	13.60	12.14	3.00	Sab	AB	0.38
UGC 03107	133	04:37:21.852	+09:32:40.747	0.0283	14.89	13.35	3.19	Sb	A	0.24
NGC 1645	134	04:44:06.400	–05:27:56.414	0.0163	13.46	11.97	3.38	S0a	B	0.64
IC 2095	141	04:48:45.881	–05:07:28.668	0.0095	15.59	15.23	1.28	Sc	AB	0.15
UGC 03253	146	05:19:41.885	+84:03:09.432	0.0138	13.69	12.27	3.07	Sb	B	0.62
NGC 2253	147	06:43:41.836	+65:12:22.950	0.0120	13.26	11.79	2.97	Sbc	B	0.87
UGC 03539	148	06:48:54.003	+66:15:41.885	0.0110	14.95	14.13	2.31	Sc	AB	0.19
NGC 2347	149	07:16:04.087	+64:42:40.776	0.0149	13.18	11.65	3.08	Sbc	AB	0.64
UGC 03899	150	07:32:37.749	+35:36:52.125	0.0130	14.99	14.46	1.47	Sd	A	0.43
NGC 2410	151	07:35:02.261	+32:49:19.566	0.0156	13.37	11.78	3.29	Sb	AB	0.32
UGC 03969	153	07:41:14.343	+27:36:50.635	0.0275	15.03	13.42	3.21	Sb	A	0.18
UGC 03995	155	07:44:09.128	+29:14:50.751	0.0159	13.48	11.92	3.58	Sb	B	0.46
NGC 2449	156	07:47:20.299	+26:55:48.708	0.0163	13.70	12.22	3.37	Sab	AB	0.50

Notes. [a] CALIFA unique ID number for the galaxy. [b] Equatorial coordinates of the galaxies as provided by NED. [c] Redshift of the galaxies based on SDSS DR7 spectra or complemented with SIMBAD information if SDSS spectra are not available. [d] Petrosian magnitudes as given by SDSS DR7 database corrected for Galactic extinction. [e] Morphological type from our own visual classification (see W14 for details). "(x)" indicates ongoing mergers. [f] Bar strength of the galaxy as an additional outcome of our visual classification. A stands for non-barred, B for barred and AB if unsure. [g] Ratio between the semi-minor and semi-major axis based on a detailed re-analysis of the SDSS images (see W14 for details). [h] Morphological classification of this particular galaxy NGC 4676B from Wild et al. (2014).

and has three clear peaks at around $\alpha \sim 15°$, 255°, and 345°. All three peaks are located in the same observing semester, in the period from April to October. As noted in H13, there was a downtime of the 3.5 m telescope from August 2010 until April 2011 due to operational reasons at the observatory, which delayed the survey roughly by eight months. In addition to this, because of scheduling matters, a large part of the granted time was allocated in summer seasons. Regardless of the observing time issue, the distribution of physical properties for DR2 is nearly random, as expected, and covers galaxies with a wide range of properties as discussed below.

Figure 2 shows the distribution of galaxies in the color–magnitude diagram. The DR2 sample covers nearly the full range of the CALIFA MS. On average, the DR2 targets

Table 1. continued.

Name	ID[a]	α(J2000)[b]	δ(J2000)[b]	z[c]	m_g[d]	m_z[d]	$m_u - m_z$[d]	Type[e]	Bar[f]	b/a[g]
UGC 04132	165	07:59:13.046	+32:54:52.822	0.0174	13.80	12.23	3.17	Sbc	AB	0.26
UGC 04722	231	09:00:24.130	+25:36:53.079	0.0058	15.16	15.07	1.25	Sdm	A	0.19
NGC 2730	232	09:02:15.824	+16:50:17.841	0.0128	13.93	13.13	1.95	Scd	B	0.64
NGC 2880	272	09:29:34.567	+62:29:26.052	0.0051	12.40	10.99	3.21	E7	AB	0.71
IC 2487	273	09:30:09.166	+20:05:27.042	0.0145	13.94	12.58	2.90	Sc	AB	0.22
IC 0540	274	09:30:10.338	+07:54:09.903	0.0069	14.24	12.76	3.17	Sab	AB	0.30
NGC 2906	275	09:32:06.218	+08:26:30.367	0.0071	12.89	11.46	3.37	Sbc	A	0.51
NGC 2916	277	09:34:57.601	+21:42:18.940	0.0124	13.37	11.86	3.16	Sbc	A	0.59
UGC 05108	278	09:35:26.279	+29:48:45.439	0.0271	14.35	12.73	3.35	Sb	B	0.77
UGC 05358	306	09:58:47.135	+11:23:19.318	0.0097	15.12	14.41	1.79	Sd	B	0.33
UGC 05359	307	09:58:51.647	+19:12:53.918	0.0283	14.74	13.43	2.93	Sb	B	0.37
UGC 05396	309	10:01:40.485	+10:45:23.140	0.0181	14.43	13.24	2.66	Sbc	AB	0.27
NGC 3106	311	10:04:05.251	+31:11:07.653	0.0207	13.41	12.01	3.31	Sab	A	0.93
UGC 05498NED01	314	10:12:03.658	+23:05:07.590	0.0210	14.65	12.95	3.48	Sa(x)	A	0.24
NGC 3160	319	10:13:55.115	+38:50:34.534	0.0229	14.64	12.92	3.63	Sab	AB	0.29
UGC 05598	326	10:22:14.004	+20:35:21.879	0.0188	14.80	13.52	2.77	Sb	A	0.30
NGC 3303	340	10:37:00.088	+18:08:09.194	0.0200	14.24	12.55	3.56	S0a(x)	AB	0.60
UGC 05771	341	10:37:19.340	+43:35:15.321	0.0248	14.10	12.43	3.58	E6	A	0.71
NGC 3381	353	10:48:24.818	+34:42:41.078	0.0054	13.41	12.68	1.82	Sd	B	0.71
UGC 06036	364	10:55:55.261	+36:51:41.468	0.0218	14.14	12.47	3.65	Sa	A	0.29
IC 0674	381	11:11:06.361	+43:37:58.812	0.0251	14.07	12.57	3.40	Sab	B	0.65
NGC 3614	388	11:18:21.332	+45:44:53.408	0.0077	13.60	12.37	2.90	Sbc	AB	0.72
NGC 3811	436	11:41:16.630	+47:41:26.920	0.0102	13.48	12.06	3.00	Sbc	B	0.62
NGC 3991	475	11:57:30.959	+32:20:13.289	0.0108	14.08	13.52	1.42	Sm	A	0.22
NGC 3994	476	11:57:36.866	+32:16:39.426	0.0103	13.46	11.98	2.87	Sbc	AB	0.47
NGC 4003	479	11:57:59.033	+23:07:29.636	0.0219	13.96	12.39	3.29	S0a	B	0.42
UGC 07012	486	12:02:03.146	+29:50:52.737	0.0102	14.41	13.81	1.73	Scd	AB	0.54
NGC 4149	502	12:10:32.849	+58:18:14.884	0.0103	13.86	12.30	3.10	Sa	AB	0.19
NGC 4185	515	12:13:22.192	+28:30:39.468	0.0130	13.27	12.01	3.03	Sbc	AB	0.64
NGC 4210	518	12:15:15.842	+65:59:07.156	0.0091	13.44	12.03	2.99	Sb	B	0.73
IC 0776	528	12:19:03.120	+08:51:22.153	0.0081	14.74	14.42	1.25	Sdm	A	0.56
NGC 4470	548	12:29:37.778	+07:49:27.129	0.0079	12.96	12.12	1.84	Sc	A	0.66
NGC 4644	569	12:42:42.664	+55:08:43.897	0.0165	14.41	13.02	3.00	Sb	A	0.45
NGC 4676A	577	12:46:10.107	+30:43:54.899	0.0222	14.78	13.08	2.99	Sdm(x)	AB	0.28
NGC 4874	592	12:59:35.709	+27:57:33.339	0.0239	12.89	11.37	3.42	E0	A	0.88
UGC 08107	593	12:59:39.778	+53:20:28.203	0.0277	14.30	12.71	3.45	Sa(x)	A	0.39
UGC 08231	606	13:08:37.555	+54:04:27.737	0.0083	14.44	13.97	1.45	Sd	AB	0.37
UGC 08234	607	13:08:46.505	+62:16:18.099	0.0270	13.45	12.23	2.92	S0	A	0.63
NGC 5000	608	13:09:47.487	+28:54:24.993	0.0187	13.94	12.50	2.97	Sbc	B	0.60
UGC 08250	609	13:10:20.138	+32:28:59.479	0.0176	15.17	14.03	2.39	Sc	A	0.19
UGC 08267	610	13:11:11.334	+43:43:34.787	0.0242	14.87	13.14	3.39	Sb	AB	0.20
NGC 5205	630	13:30:03.571	+62:30:41.624	0.0059	13.45	12.12	2.92	Sbc	B	0.67
NGC 5216	633	13:32:06.896	+62:42:02.392	0.0098	13.58	12.12	3.27	E0	A	0.91
UGC 08733	657	13:48:38.994	+43:24:44.830	0.0078	14.70	13.63	1.83	Sdm	B	0.49
IC 0944	663	13:51:30.868	+14:05:31.959	0.0234	13.67	11.95	3.59	Sab	A	0.30
UGC 08778	664	13:52:06.669	+38:04:01.273	0.0108	14.20	12.90	2.89	Sb	A	0.21
UGC 08781	665	13:52:22.745	+21:32:21.669	0.0253	13.92	12.49	3.31	Sb	B	0.52
NGC 5378	676	13:56:51.013	+37:47:50.055	0.0100	13.53	12.12	3.23	Sb	B	0.63
NGC 5394	680	13:58:33.201	+37:27:13.118	0.0114	14.39	13.59	2.29	Sbc(x)	B	0.74
NGC 5406	684	14:00:20.120	+38:54:55.528	0.0180	13.37	11.84	3.46	Sb	B	0.88
NGC 5485	708	14:07:11.349	+55:00:05.933	0.0064	12.41	10.88	3.42	E5	A	0.81
UGC 09067	714	14:10:45.458	+15:12:33.858	0.0262	14.29	13.09	2.61	Sbc	AB	0.45
NGC 5520	715	14:12:22.811	+50:20:54.309	0.0063	13.31	12.05	2.71	Sbc	A	0.57
NGC 5614	740	14:24:07.588	+34:51:31.869	0.0130	12.68	11.03	3.56	Sa(x)	A	0.95

comprise ~37% of each color–magnitude bin of the total 600 objects in the full CALIFA sample. The deficit of low-luminosity galaxies with intermediate colors, noted in DR1, has improved. Fluctuations can be explained by the effect of low-number statistics, especially within those color–magnitude bins in which the MS contains fewer galaxies. This point is highlighted in Fig. 2 and emphasizes the need to eventually observe the full CALIFA sample to obtain a sufficient number of galaxies in each bin for a meaningful multi dimensional statistical analysis.

Figure 3 compares the redshift distribution of the CALIFA galaxies in the DR2 and DR1, as a percentage of the CALIFA MS. Except for a few particular bins, the redshift distribution is homogeneous with respect to the MS.

One important test to be made is whether the number density of galaxies estimated from the DR2 sample is not biased with respect to the MS. Figure 4 shows the r-band luminosity function (LF) of the DR2 sample as compared to the MS and the reference SDSS sample of Blanton et al. (2005). We refer to W14 for all technical details on how the LFs are obtained and for the

Table 1. continued.

Name	ID[a]	α(J2000)[b]	δ(J2000)[b]	z[c]	m_g[d]	m_z[d]	$m_u - m_z$[d]	Type[e]	Bar[f]	b/a[g]
NGC 5630	749	14:27:36.610	+41:15:27.919	0.0089	13.60	13.04	1.62	Sdm	B	0.32
NGC 5682	758	14:34:44.978	+48:40:12.831	0.0076	14.39	13.64	1.74	Scd	B	0.31
NGC 5720	764	14:38:33.281	+50:48:54.874	0.0260	14.13	12.72	3.18	Sbc	B	0.65
UGC 09476	769	14:41:32.029	+44:30:45.978	0.0109	13.63	12.61	2.31	Sbc	A	0.63
NGC 5784	778	14:54:16.450	+42:33:28.452	0.0181	13.20	11.69	3.45	S0	A	0.81
UGC 09665	783	15:01:32.465	+48:19:10.928	0.0085	14.30	12.83	3.12	Sb	A	0.23
NGC 5888	789	15:13:07.372	+41:15:52.666	0.0291	13.84	12.25	3.47	Sb	B	0.54
NGC 5908	791	15:16:43.191	+55:24:34.461	0.0112	13.12	11.15	3.97	Sa	A	0.24
NGC 5930	795	15:26:07.950	+41:40:33.829	0.0088	13.53	11.76	3.27	Sab(x)	AB	0.84
UGC 09873	797	15:29:50.651	+42:37:44.104	0.0188	15.19	13.95	2.63	Sb	A	0.21
UGC 09892	798	15:32:51.947	+41:11:29.282	0.0189	14.80	13.51	2.78	Sbc	A	0.29
NGC 5966	806	15:35:52.108	+39:46:08.047	0.0151	13.24	11.76	3.36	E4	A	0.60
IC 4566	807	15:36:42.162	+43:32:21.545	0.0186	13.84	12.35	3.39	Sb	B	0.69
NGC 5987	809	15:39:57.356	+58:04:46.249	0.0100	12.76	11.07	3.62	Sa	A	0.39
NGC 6004	813	15:50:22.720	+18:56:21.386	0.0128	13.55	12.22	3.02	Sbc	B	0.94
NGC 6020	815	15:57:08.137	+22:24:16.492	0.0144	13.40	11.94	3.40	E4	A	0.73
NGC 6021	816	15:57:30.685	+15:57:21.766	0.0158	13.63	12.10	3.45	E5	A	0.78
NGC 6032	820	16:03:01.124	+20:57:21.330	0.0145	13.97	12.56	2.94	Sbc	B	0.30
UGC 10205	822	16:06:40.181	+30:05:56.651	0.0219	13.89	12.29	3.32	S0a	A	0.58
NGC 6063	823	16:07:12.993	+07:58:44.368	0.0095	13.63	12.53	2.56	Sbc	A	0.60
IC 1199	824	16:10:34.347	+10:02:25.322	0.0158	13.97	12.59	2.86	Sb	AB	0.41
NGC 6081	826	16:12:56.858	+09:52:01.580	0.0171	13.62	11.93	3.65	S0a	A	0.46
UGC 10331	828	16:17:21.123	+59:19:12.466	0.0152	14.50	13.60	2.11	Sc(x)	AB	0.26
NGC 6125	829	16:19:11.536	+57:59:02.899	0.0154	12.91	11.39	3.43	E1	A	0.91
NGC 6132	831	16:23:38.840	+11:47:10.459	0.0166	14.18	13.09	2.38	Sbc	A	0.36
NGC 6146	832	16:25:10.331	+40:53:34.325	0.0292	13.28	11.80	3.40	E5	A	0.77
NGC 6154	833	16:25:30.483	+49:50:24.934	0.0199	13.81	12.39	3.33	Sab	B	0.65
UGC 10380	834	16:25:49.911	+16:34:33.827	0.0292	14.89	13.18	3.57	Sb	AB	0.28
NGC 6150	835	16:25:49.966	+40:29:19.419	0.0292	13.92	12.35	3.49	E7	A	0.48
UGC 10384	837	16:26:46.685	+11:34:48.968	0.0165	14.70	13.22	2.82	Sb	A	0.22
UGC 10388	838	16:27:02.974	+16:22:56.031	0.0154	14.03	12.67	3.15	Sa	AB	0.40
NGC 6173	840	16:29:44.875	+40:48:41.965	0.0294	13.16	11.61	3.49	E6	A	0.65
NGC 6168	841	16:31:20.834	+20:11:08.298	0.0086	14.70	13.58	2.30	Sc	AB	0.18
UGC 10650	843	17:00:14.583	+23:06:22.839	0.0099	15.35	16.29	0.04	Scd	A	0.20
UGC 10693	845	17:04:53.020	+41:51:55.764	0.0280	13.45	12.00	3.41	E7	AB	0.68
UGC 10695	846	17:05:05.574	+43:02:35.360	0.0280	13.98	12.42	3.50	E5	A	0.67
UGC 10710	847	17:06:52.522	+43:07:19.961	0.0280	14.35	12.75	3.31	Sb	A	0.25
NGC 6310	848	17:07:57.480	+60:59:24.569	0.0114	13.72	12.29	3.24	Sb	A	0.22
NGC 6314	850	17:12:38.716	+23:16:12.297	0.0221	13.52	12.12	3.09	Sab	A	0.51
NGC 6338	851	17:15:22.976	+57:24:40.284	0.0274	13.33	11.70	3.66	E5	A	0.66
UGC 10796	852	17:16:47.725	+61:55:12.433	0.0102	14.28	13.74	1.44	Scd	AB	0.49
UGC 10811	854	17:18:43.726	+58:08:06.433	0.0291	14.55	13.02	3.30	Sb	B	0.42
IC 1256	856	17:23:47.285	+26:29:11.482	0.0159	13.91	12.70	2.60	Sb	AB	0.59
NGC 6394	857	17:30:21.423	+59:38:23.613	0.0284	14.53	13.06	3.05	Sbc	B	0.29
UGC 10905	858	17:34:06.438	+25:20:38.290	0.0265	13.68	12.15	3.37	S0a	A	0.53
NGC 6411	859	17:35:32.849	+60:48:48.255	0.0123	12.73	11.37	3.34	E4	A	0.68
NGC 6427	860	17:43:38.599	+25:29:38.178	0.0108	13.28	11.82	3.30	S0	AB	0.61
UGC 10972	861	17:46:21.921	+26:32:37.681	0.0155	14.10	12.78	2.91	Sbc	A	0.22
NGC 6478	862	17:48:37.742	+51:09:13.683	0.0227	14.16	12.83	2.59	Sc	A	0.42
NGC 6497	863	17:51:17.966	+59:28:15.149	0.0105	13.73	12.26	3.41	Sab	B	0.65
NGC 6515	864	17:57:25.195	+50:43:41.242	0.0228	13.52	12.10	3.27	E3	A	0.78
UGC 11228	865	18:24:46.260	+41:29:33.853	0.0194	13.78	12.26	3.43	S0	B	0.57
UGC 11262	866	18:30:35.698	+42:41:33.704	0.0186	14.89	13.75	2.65	Sc	A	0.39

explanation of the turnover of the LF at $M_r \approx -18.6$. The DR2 sample already reproduces the CALIFA MS LF very closely for most of the magnitude bins.

An important characteristic of the CALIFA MS is that it contains galaxies of all morphological types. Galaxy morphologies were inferred by combining the independent visual classifications of several collaboration members as described in W14. Figure 5 shows a histogram of bar strength as well as the percentage of DR2 galaxies with respect to the CALIFA MS distribution for different morphological types grouped into elliptical, lenticular, and spiral galaxies (and subtypes). A more detailed classification of ellipticals (from 0 to 7) is available, but we do not distinguish between them here because of the low number of galaxies per elliptical subtype within DR2. From 200 galaxies in DR2, 18 have been classified as ongoing mergers[2] (of any type). As clearly seen in Fig. 5, the percentage of DR2 galaxies with respect to the CALIFA MS is almost constant for all

[2] According to our visual classification.

Table 1. continued.

Name	ID[a]	α(J2000)[b]	δ(J2000)[b]	z[c]	m_g[d]	m_z[d]	$m_u - m_z$[d]	Type[e]	Bar[f]	b/a[g]
NGC 6762	867	19:05:37.090	+63:56:02.791	0.0098	13.81	12.37	3.29	Sab	A	0.49
MCG-02-51-004	868	20:15:39.858	–13:37:19.227	0.0188	13.88	12.47	2.93	Sb	A	0.37
NGC 6941	869	20:36:23.474	–04:37:07.459	0.0208	13.47	12.06	3.14	Sb	B	0.73
NGC 6978	871	20:52:35.435	–05:42:40.041	0.0199	13.48	11.95	3.27	Sb	AB	0.39
UGC 11649	872	20:55:27.620	–01:13:30.879	0.0127	13.47	12.06	3.19	Sab	B	0.88
NGC 7025	874	21:07:47.336	+16:20:09.224	0.0166	12.85	11.25	3.57	S0a	A	0.72
UGC 11717	877	21:18:35.413	+19:43:07.397	0.0212	14.20	12.45	3.60	Sab	A	0.47
MCG-01-54-016	878	21:25:59.971	–03:48:32.267	0.0098	14.90	14.26	1.56	Scd	A	0.13
UGC 11792	880	21:42:12.700	+05:36:55.333	0.0160	14.82	13.30	3.08	Sbc	A	0.20
NGC 7194	881	22:03:30.938	+12:38:12.414	0.0272	13.55	12.01	3.47	E3	A	0.79
UGC 11958	883	22:14:46.882	+13:50:27.132	0.0262	14.02	12.47	3.44	S0(x)	A	0.74
UGC 11982	884	22:18:52.939	–01:03:31.254	0.0162	15.24	14.09	2.68	Scd	A	0.23
UGC 12054	885	22:29:32.454	+07:43:33.685	0.0070	14.62	13.82	1.89	Sc	A	0.24
NGC 7311	886	22:34:06.797	+05:34:13.166	0.0150	12.60	11.18	3.25	Sa	A	0.49
NGC 7321	887	22:36:28.022	+21:37:18.354	0.0238	13.58	12.29	2.98	Sbc	B	0.69
UGC 12127	888	22:38:29.421	+35:19:46.894	0.0275	13.46	11.94	3.53	E1	A	0.85
UGC 12185	890	22:47:25.063	+31:22:24.672	0.0222	14.16	12.75	3.21	Sb	B	0.47
UGC 12224	891	22:52:38.364	+06:05:37.045	0.0118	13.89	12.86	2.60	Sc	A	0.83
NGC 7436B	893	22:57:57.546	+26:09:00.012	0.0246	13.40	11.80	3.59	E2(x)	A	0.90
UGC 12274	894	22:58:19.600	+26:03:42.974	0.0255	14.21	12.59	3.63	Sa	A	0.36
UGC 12308	895	23:01:18.684	+14:20:22.466	0.0076	14.69	14.01	1.82	Scd	A	0.25
NGC 7466	896	23:02:03.464	+27:03:09.342	0.0251	14.22	12.76	3.00	Sbc	A	0.53
NGC 7489	898	23:07:32.695	+22:59:53.127	0.0208	13.70	12.61	2.42	Sbc	A	0.55
NGC 7549	901	23:15:17.271	+19:02:30.437	0.0157	13.98	12.62	2.76	Sbc	B	0.75
NGC 7563	902	23:15:55.928	+13:11:46.040	0.0143	13.33	11.80	3.45	Sa	B	0.68
NGC 7562	903	23:15:57.495	+06:41:15.151	0.0120	12.10	10.56	3.43	E4	A	0.68
NGC 7591	904	23:18:16.260	+06:35:08.860	0.0165	13.39	11.80	3.24	Sbc	B	0.59
UGC 12519	909	23:20:02.769	+15:57:10.028	0.0146	14.24	12.90	2.87	Sc	AB	0.21
UGC 12518	910	23:20:12.737	+07:55:55.915	0.0093	14.74	12.91	3.67	Sb	A	0.23
NGC 7625	913	23:20:30.139	+17:13:32.034	0.0054	13.03	11.47	3.03	Sa	A	0.78
NGC 7631	914	23:21:26.675	+08:13:03.463	0.0125	13.40	12.05	3.00	Sb	A	0.44
NGC 7653	915	23:24:49.358	+15:16:32.165	0.0142	13.17	11.88	3.00	Sb	A	0.88
NGC 7671	916	23:27:19.336	+12:28:02.673	0.0135	13.14	11.56	3.56	S0	A	0.65
NGC 7683	917	23:29:03.823	+11:26:42.607	0.0124	13.00	11.38	3.61	S0	A	0.62
UGC 12688	922	23:35:26.096	+07:19:19.554	0.0174	14.53	13.47	2.29	Scd(x)	AB	0.29
NGC 7716	924	23:36:31.450	+00:17:50.179	0.0085	13.03	11.60	3.25	Sb	A	0.71
NGC 7738	927	23:44:02.058	+00:30:59.838	0.0228	13.94	12.17	3.56	Sb	B	0.31
UGC 12816	930	23:51:50.691	+03:04:57.909	0.0178	14.09	13.16	2.08	Sc	A	0.62
NGC 7783NED01	932	23:54:10.078	+00:22:58.299	0.0262	13.62	12.06	3.43	Sa(x)	A	0.46
UGC 12864	935	23:57:23.921	+30:59:31.456	0.0156	14.24	13.25	2.19	Sc	B	0.32
MCG-01-01-012	936	23:59:10.803	–04:11:29.763	0.0193	14.64	12.83	4.07	Sab	AB	0.26
NGC 7800	937	23:59:36.753	+14:48:25.043	0.0058	13.35	13.16	1.11	Ir	AB	0.40
NGC 5947	938	15:30:36.595	+42:43:01.732	0.0198	14.07	12.81	2.80	Sbc	B	0.83
NGC 4676B[h]	939	12:46:11.235	+30:43:21.871	0.0218	17.00	15.31	3.44	Sb(x)	B	0.82

types, implying that the DR2 coverage seems to be consistent with a random selection. Axis ratios (b/a) were measured from the SDSS *r*-band image using growth curve analysis, by calculating light moments after proper sky subtraction and masking of foreground stars (see W14 for details). The axis ratios can be used as a proxy of the inclination of spiral galaxies. Figure 6 shows that the DR2 sample covers the same range of axis ratios as the MS. A Kolmogorov-Smirnov test gives a <5% confidence that the DR2 sample is drawn from a different distribution than the underlying MS.

In Fig. 7, we present the distribution of stellar masses for the DR2 galaxies. Galaxy stellar masses are from González Delgado et al. (2014a), and they have been estimated following the process described in Pérez et al. (2013), Cid Fernandes et al. (2013, 2014), and González Delgado et al. (2014b). These masses account for spatial variations in both M/L ratio and stellar extinction. In short, we use the STARLIGHT code (Cid Fernandes et al. 2005) to fit each spectrum extracted from the datacube with a combination of SSP models from the Granada (González Delgado et al. 2005) and MILES (Vazdekis et al. 2010) libraries, that cover the full metallicity range of the MILES models ($\log Z/Z_\odot$ from −2.3 to +0.22), and ages from 0.001 to 14 Gyr. We assume a Salpeter IMF. The DR2 galaxies cover intermediate to high-mass galaxies, including at least ten galaxies per 0.25 dex bin between 10^{10} and $10^{11.75}$ $M_\odot$ and a median value close to 10^{11} $M_\odot$. The asymmetric distribution is expected from the distribution in absolute magnitudes (see Fig. 2) and is inherited from the CALIFA MS because of its selection criteria (see W14 for details).

A more general "*panoramic view*" of the DR2 sample characteristics is presented in Fig. 8. Several of the main properties observable in 2D are highlighted for 169 randomly-selected galaxies, shown individually in hexagons that together form the shape of a CALIFA-like FoV. The galaxies have been ordered by *r*-band absolute magnitude, from top right (brightest absolute magnitude) to bottom left (faintest absolute magnitude). The highlighted properties derive from several different analysis pipelines developed within the collaboration. Stellar properties,

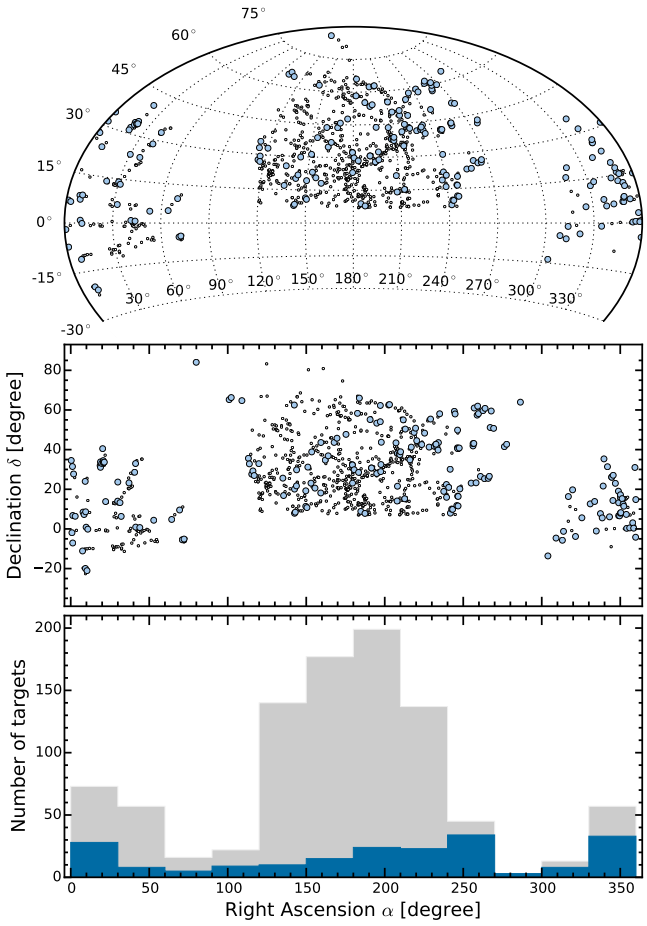

Fig. 1. Distribution on the sky of galaxies in the CALIFA mother sample (small open circles) and CALIFA DR2 sample (blue filled symbols). The *upper panel* shows the distribution in an Aitoff projection in J2000 Equatorial Coordinates (cut off at $\delta = -30°$, below which the sample does not extend), while the *middle panel is* plotted in the Cartesian system. The *lower panel* shows both samples as a function of right ascension. The number distribution in bins of 30° along the right ascension is shown for the mother sample (gray area) and the DR2 sample (blue area).

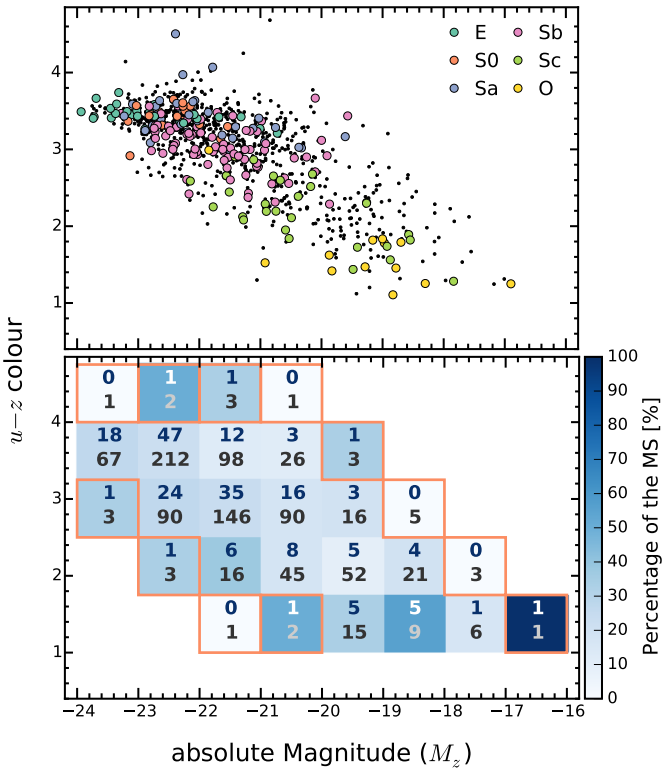

Fig. 2. *Upper panel*: distribution of CALIFA galaxies in the $u-z$ vs. M_z color–magnitude diagram. Black dots denote galaxies in the CALIFA mother sample (S12, W14) and colored symbols indicate CALIFA DR2 galaxies. Different colors account for the morphological classification, which range from ellipticals (E) to late-type spirals; group "O" includes Sd, Sdm, Sm, and I types. *Lower panel*: fraction of galaxies in the DR2 sample with respect to the CALIFA MS distribution (939 objects) in bins of 1 mag in M_z and 0.75 mag in $u-z$. The total number of galaxies per bin in the DR2 sample and the MS are shown in the upper and lower part of each bin, respectively. Bins for which the number of galaxies in the MS is less than 5 are prone to low-number statistics and enclosed by an orange square for better identification.

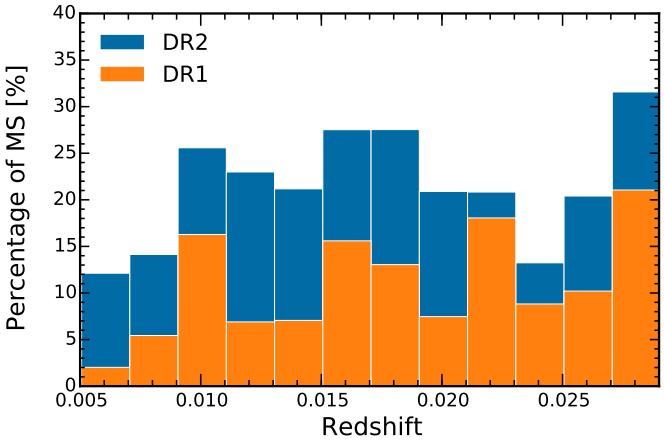

Fig. 3. Redshift distribution of the DR2 (blue) and DR1 (orange) as percentage of the CALIFA MS.

like ages and mass surface density, were measured with the STARLIGHT code (see references in the preceding paragraph describing the distribution of stellar masses in the sample) while gas properties and emission lines were measured using FIT3D (Sánchez et al. 2007). This plot is only intended to demonstrate the diversity of the DR2 sample.

3. Observing strategy and setup overview

For the sake of completeness, we provide here a brief summary of the instrument layout and observing strategy. All the details can be found in S12. The PPak fiber bundle of the PMAS instrument has a FoV of 74″ × 64″. There are 382 fibers in total, distributed in three different groups. The PPak Integral Field Unit (IFU) holds 331 "science" fibers in a hexagonal grid with a maximum diameter of 74″ while each fiber projects to 2.″7 in diameter on the sky. The fiber-to-fiber distance is 3.″2, which yields a total filling factor of 0.6. An additional set of 36 fibers devoted to measuring the surrounding sky background are distributed in six bundles of 6 fibers each, located in a ring 72″ from the center. Finally, there are 15 extra fibers connected to the calibration unit.

Every galaxy in the CALIFA sample is observed in the optical range using two different overlapping setups. The V500 low-resolution mode ($R \sim 850$) covers the range 3745–7500 Å,

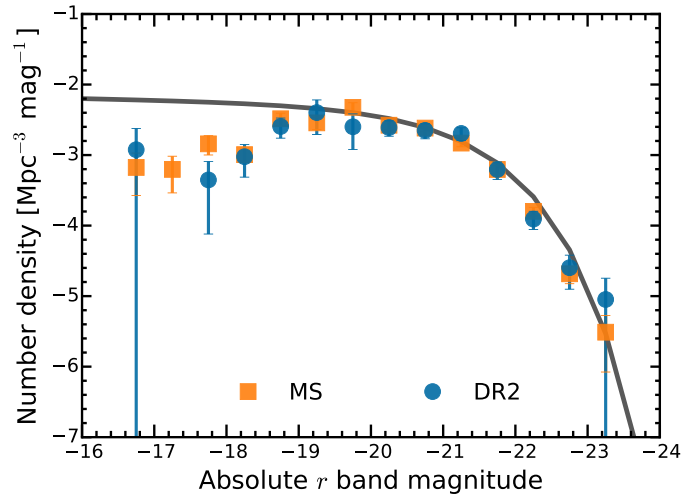

Fig. 4. Luminosity functions in the r band of the CALIFA mother sample (orange squares) and the DR2 sample (blue points). Error bars represent Poissonian uncertainties. The line shows the Schechter fit to the LF of Blanton et al. (2005).

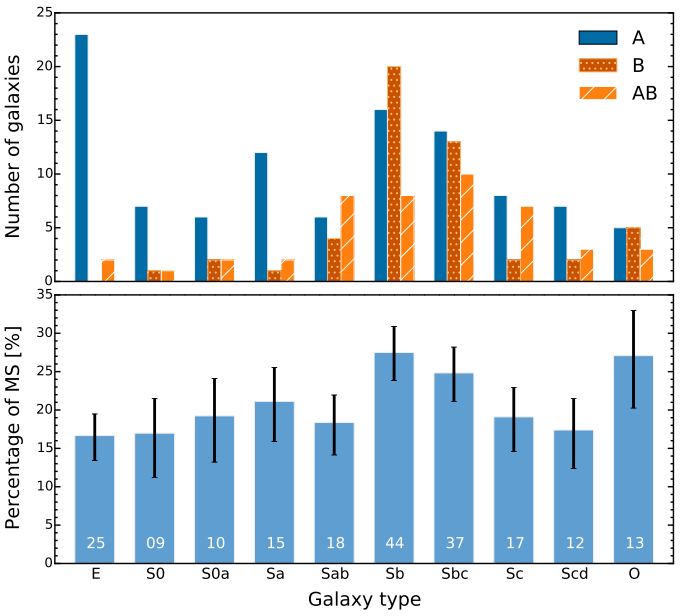

Fig. 5. Distribution of visually classified morphological types in the DR2 sample. We divide the galaxies into ellipticals (E), spirals (from S0 to Scd), and the *other* group "O", which includes Sd, Sdm, Sm, and I (only one) types. *Upper panel*: bar strength histogram, where A stands for non-barred, B for barred and AB if unsure. *Lower panel*: the percentage of galaxies in the DR2 sample with respect to the CALIFA MS distribution. The total number of galaxies in the DR2 for each morphology type is written on each bar. Error bars are computed from the binomial errors of the associated DR2 number counts (Wilson 1927). The morphological distribution of the DR2 sample is similar to that of the mother sample.

but it is affected by internal vignetting within the spectrograph giving an unvignetted range of 4240–7140 Å. The blue mid-resolution setup (V1200; $R \sim 1650$) covers the range 3400–4840 Å with an unvignetted range of 3650–4620 Å. The resolutions quoted are those at the overlapping wavelength range ($\lambda \sim 4500$ Å). To reach a filling factor of 100% across the FoV, a 3-pointing dithering scheme is used for each object.

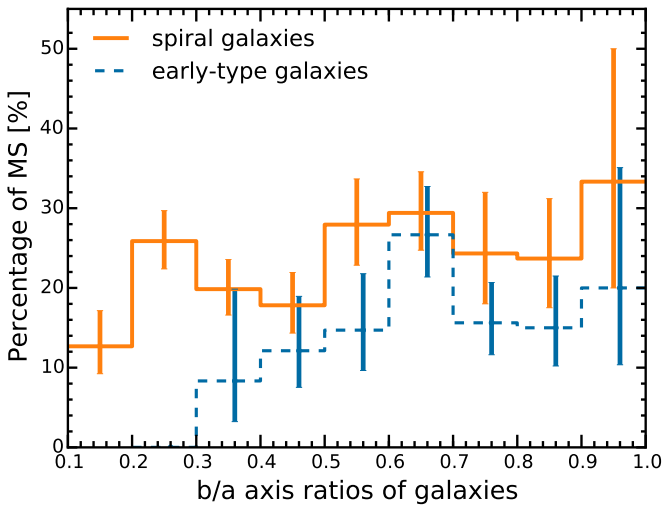

Fig. 6. Percentage of galaxies in the DR2 sample with respect to the CALIFA MS distribution, as a function of the light-weighted axis ratio (b/a). Galaxies were separated into early-type galaxies (E+S0) and spiral galaxies (Sa and later). The CALIFA mother sample does not include any elliptical galaxies with $b/a < 0.3$. Error bars are computed from the binomial errors of the associated DR2 number counts.

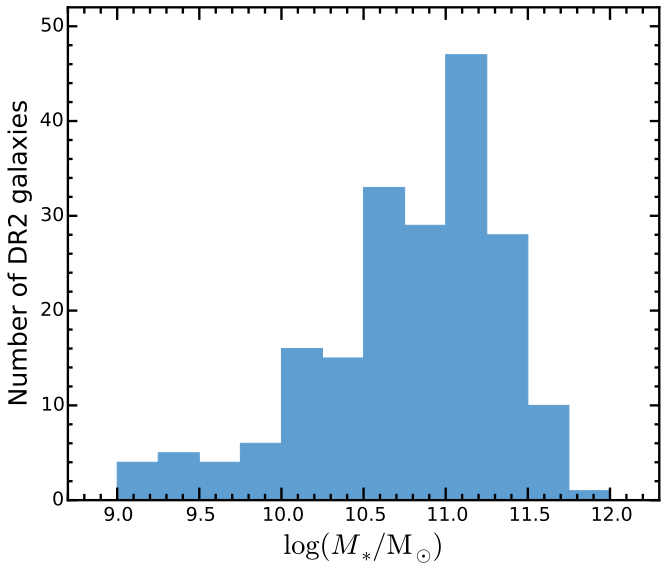

Fig. 7. Distribution of stellar masses in the DR2 sample. The stellar masses are determined from the CALIFA data using spectral fitting techniques (see text for details).

The exposure time per pointing is fixed. We carry out V1200 observations during dark nights with an exposure time of 1800 s per pointing (split in 2 or 3 individual exposures). We take V500 observations during gray nights with 900 s per pointing.

In the following section, we describe the improvements to the CALIFA data reduction pipeline used to produce the DR2 data.

4. Data processing and error propagation

4.1. Overview of the reduction scheme

As described in H13, since V1.3c the CALIFA pipeline has a `Python`-based architecture (`Py3D` package). Here we present a summary of the main steps of the reduction process. The

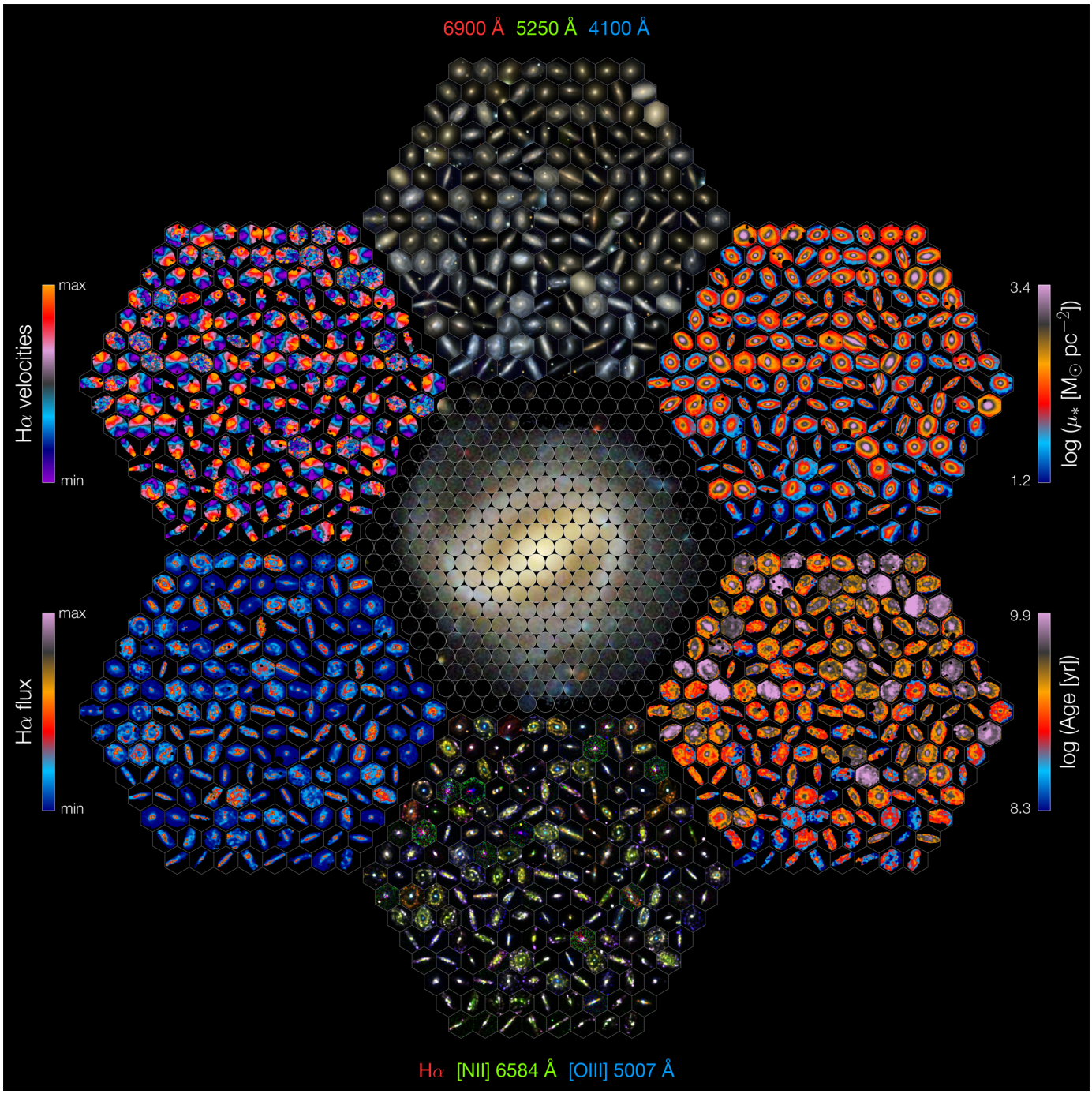

Fig. 8. CALIFA "*panoramic view*" (also CALIFA's "*Mandala*") representation, consisting of the basic physical properties (all of them derived from the CALIFA datacubes) of a subsample of 169 galaxies extracted randomly from DR2. We show 1) 3-color broadband images (*top center*; central wavelength 6900 Å, 5250 Å, and 4100 Å); 2) stellar mass surface densities (*upper right*); 3) ages (*lower right*); 4) narrowband images (*bottom center*; emission lines: Hα, [N II] 6584 Å, and [O III] 5007 Å); 5) Hα emission (*lower left*), and 6) Hα kinematics (*upper left*). The CALIFA logo is placed at the central hexagon.

particular improvements on the new CALIFA pipeline, V1.5, are described in Sect. 4.2.

Each raw frame is stored in four different FITS files, corresponding to each of the four amplifiers of the detector. As a first step, these four files are combined into a single frame and bias subtracted. We developed a new tool (Husemann et al. 2012) for the detection and clipping of cosmic rays, which uses a Laplacian edge detection scheme combined with a point spread function convolution approach. Relative flexure offsets are estimated with respect to the continuum and arc-lamp calibration frames and the wavelength solution is corrected for each individual science frame. The stray-light map is reconstructed using the gaps between the fiber traces and subtracted from the calibration and science exposures. For spectral extraction, the widths of the fiber profiles are measured using the position of the fibers obtained from the continuum lamp. An optimal extraction algorithm (Horne 1986) is used to extract the spectra based on the previous measurements of the position and widths. The extracted flux, for each pixel in the dispersion direction, is stored in a row-stacked-spectrum file (RSS). The wavelength

solution is obtained from the HeHgCd calibration lamp exposure for each CALIFA data set. The spectra are resampled to a linear grid in wavelength and the spectral resolution is homogenized to a common value along the dispersion axis using a Gaussian convolution. Flexure offsets in the dispersion direction are included at this step. The Poisson plus read-out noise (and bad pixel masks) are propagated in the reduction process. For the wavelength solution, errors are analytically propagated during the Gaussian convolution and a Monte Carlo approach is used to estimate the noise vector after the spline resampling of the spectra. Fiber transmission throughput is corrected by comparing the RSS science frames with the corresponding sky exposures taken during twilight.

In the V1.3c pipeline, standard star observations were used to derive the sensitivity curve to perform the flux calibration of the science exposures. Aperture losses were empirically corrected by comparing the CALIFA spectra with SDSS images. In the V1.5 pipeline, we follow a completely new approach described in Sect. 4.2. After flux calibration, frames are corrected for telluric lines. The sky spectrum is obtained by taking the mean of the 30 faintest sky fibers out of the 36 sky fibers of PPak, and then subtracted from the science frames.

The science spectra corresponding to the three dithered exposures are combined into a single frame of 993 spectra. In V1.3c, these three pointings were rescaled to a common intensity, by comparing the integrated spectra within an aperture of 30″/diameter. The new procedure followed in V1.5 is explained in Sect. 4.2. After correction for Galactic extinction, the RSS is ready for the spatial rearranging of the fibers and creation of the datacube. We use a flux-conserving inverse-distance weighting scheme to reconstruct a spatial image with a sampling of 1″. The pipeline V1.5 uses a new set of parameters (see Sect. 4.2) that improves the spatial resolution of the datacube. First, we reconstruct the datacube and estimate the differential atmospheric refraction (DAR) effect. In a second step, we reconstruct the cube again where the position of the fiber against the regular grid is changed according to the DAR offset measured in the first reconstruction. This two-stage iteration avoids another resampling step, important for accurate error propagation. Finally, a new procedure is applied for the absolute flux recalibration and astronomical registration, explained in the following section.

4.2. Improvements to the CALIFA data reduction scheme

The main improvements to the current pipeline, V1.5, are: i) a new sensitivity curve for the V500 setup obtained from a dedicated calibration program for several CALIFA elliptical galaxies (Husemann et al., in prep.); ii) a new registering method, comparing individual CALIFA pointings with SDSS images; and iii) an improved image reconstruction method (cube interpolation). Step ii) also improves the absolute photometric matching of the three dithered pointings.

The new version starts with the RSS files of the three individual pointings after sky subtraction produced by pipeline V1.3c. The V500 RSS files are spectrophotometrically recalibrated with the new sensitivity curve. A new estimate for the sensitivity curve was necessary because it was based on standard star observations in V1.3c, which result in significant uncertainties. Although this is a common procedure for optical spectroscopy, it is an issue for CALIFA because of the finite size of the fibers of PPak. Aperture losses can be very significant, and come in two flavors for PPak: 1) a global aperture loss that depends on the relative position of star with respect to its nearest fibers; and 2) a wavelength-dependent aperture loss caused by atmospheric dispersion, which leads to a smooth change in the apparent position of the star and the FWHM of the seeing as a function of wavelength. While the global aperture loss can be corrected for by renormalizing the spectra based upon photometry, the wavelength-dependent losses affect the shape of the sensitivity curve and are harder to correct.

The aperture losses of the stars are mainly introduced by their point-like nature. Wavelength dependent aperture losses are significantly reduced when an extended source with a smooth surface brightness distribution is observed. Bright nearby early-type galaxies, such as those observed by CALIFA, come close to a flat surface brightness distribution except for their very center. In addition, they are predominately composed of old stellar populations, so that the shape of their optical spectra only varies smoothly with radius.

For this reason, we decide to adopt smooth elliptical galaxies as secondary spectrophotometric calibrators from which the sensitivity curves for the CALIFA PMAS-PPak observations are derived. This, in turn, requires that we have this set of secondary calibrators calibrated against primary calibrators, i.e., standard spectrophotometric stars.

A dedicated calibration program was initiated to reobserve about two dozen elliptical CALIFA galaxies chosen as secondary calibrators and the standard stars with the PMAS Lens-Array (LArr) and the V300 grism. The LArr covers a continuous 16″×16″ FoV centered on the elliptical galaxies with a sampling of 1″. A robust and accurate spectrophotometric calibration is achieved for these observations because almost the entire flux of the star is captured within the large continuous field, except the flux in the broad wings of the PSF (Sandin et al. 2008). We mainly targeted the primary HST spectroscopic standard stars, which are DA white dwarfs, for which high spectral resolution reference spectra and very accurate model spectra exist. Special care was taken in monitoring the atmospheric extinction curve during the different observing runs by targeting the same standard star twice a night with an airmass difference of about ∼1.

During the data reduction we homogenized LArr data taken with the V300 grism to a common spectral resolution of 9 Å (FWHM) across the FoV and across the wavelength range. The sensitivity curve for the LArr data is the ratio of the observed counts in the standard star spectrum (corrected for atmospheric extinction at the given airmass) to the reference spectrum, smoothed to the adopted spectral resolution. Then we calibrate the early-type galaxy observations with the derived sensitivity curve and atmospheric extinction curve for each night comparing the photometry of the calibrated LArr data with aperture matched SDSS photometry in the g and r bands, we achieve an absolute spectrophotometric accuracy of <0.03 mag. Further details about the calibration program and its application to obtain a sensitivity curve for coarse fiber IFU spectrographs will be presented in a separate publication (Husemann et al., in prep.). Below we briefly outline how we processed the CALIFA data to determine the sensitivity curve based on the LArr observations of early-type galaxies.

We start with the reduced, but spectrophotometrically uncalibrated, RSS spectra for individual CALIFA pointings of the early-type galaxies. Again, we need to compare the count spectrum with the reference spectra in physical units to derive the sensitivity curve. Specifically, we smooth the RSS spectra to a spectral resolution of 9 Å (FWHM, significantly coarser than the public CALIFA data) to match the LArr V300 grism characteristics. In addition, we resample the spectra to the heliocentric frame. All CALIFA fibers that overlap with the LArr FoV

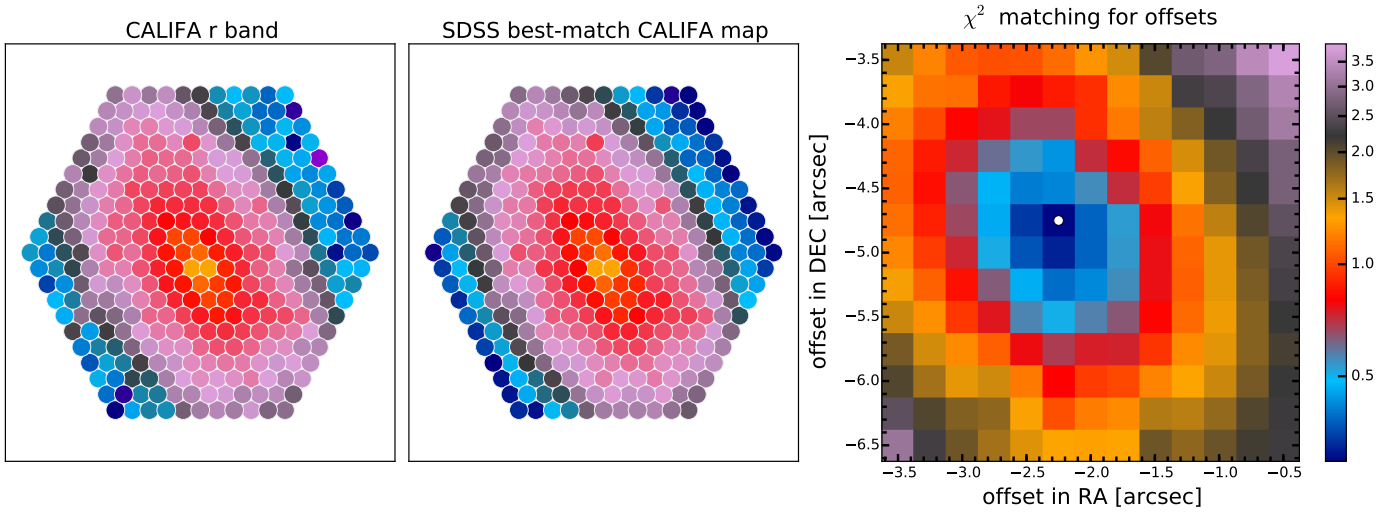

Fig. 9. Example of the registering method for pointing 1 of NGC 0496 (ID 45). *Left panel*: flux map in *r*-band for the PPak fibers. *Central panel*: predicted SDSS flux for each CALIFA fiber estimated using 2.7″ diameter apertures and adopting the PPak layout projected on the SDSS image for the best match according to the χ^2 map. Note that the PPak layout is not to scale, i.e., relative distances between adjacent fibers have been decreased for the sake of clarity. *Right panel*: χ^2 map of the offsets (best offset marked with a white dot).

and are more than 3″ away from the galaxy center are coadded. A corresponding reference spectrum is extracted from the LArr data based on the relative position and apertures of the CALIFA fibers considered. The ratio of the flux-calibrated LArr and uncalibrated CALIFA spectrum then corresponds to the instrumental sensitivity curve. In this case, we adopt the mean atmospheric extinction curve for Calar Alto presented by Sánchez et al. (2007) because the specific extinction curve for a given CALIFA observing night is not measured. Then we smooth the sensitivity curve by a high-order polynomial to obtain a noise-free representation, while masking out spectral regions suffering from telluric absorption. The final master sensitivity curve is computed as the average of all sensitivity curves independently derived from different reference early-type galaxies. We anticipate that most of the remaining systematic spectrophotometric uncertainty for CALIFA will be driven by the uncertainties in the wavelength-dependent atmospheric extinction at the time of each CALIFA observation.

The current pipeline also implements a new scheme for the registration of the images. First, sky-subtracted and calibrated images are created from SDSS DR7 (in the *r*-band for the V500 setup and the *g*-band for the V1200) based on the so-called "corrected frames" (`fpC`)[3]. Then, the magnitude in the corresponding SDSS filter is computed for each RSS spectrum. The predicted SDSS flux for each CALIFA fiber is estimated using 2.″7 diameter apertures, adopting the PPak layout projected on the SDSS image. This layout is displaced in steps in RA and Dec across a search box in the SDSS image. Then a χ^2 map is computed to obtain the best offsets for each pointing, taking errors in the flux measurements into account (only fibers with $S/N > 3.0$ are considered) and allowing for a photometric scaling factor between the SDSS and the CALIFA observations as an additional parameter. The minimum value of the χ^2 map is used to obtain the best-fitting RA and Dec for the center of the PPak IFU with respect to the center of the CALIFA galaxy seen by SDSS. Figure 9 shows an example of the described procedure. The photometric scale factor at the best matching position is used to rescale the absolute photometry of each particular RSS pointing to bring them onto the same flux scale.

The photometric anchoring to the SDSS images of the V1.5 data is more accurate than that of the previous version. However, there are a few datacubes where the new registering method does not return optimal results, particularly in low surface brightness edge-on galaxies or in the presence of bright foreground field stars[4]. This effect is more likely to occur in the V1200 setup, given its lower S/N on average compared to V500. In these cases, we apply the photometric SDSS matching of pipeline V1.3c described in H13 (to both setups, for the sake of consistency). We included a new "REGISTER" keyword in the header of the datacubes (see Sect. 5.4) and added a dagger symbol to the quality tables (Tables 6 and 7) to easily identify these galaxies.

The third step in the reduction sequence is the interpolation method used to convert from RSS to cube format, aimed at improving the spatial resolution. We use the position of each RSS pointing obtained in the previous step for the image reconstruction. In a series of tests, we found that an inverse-distance weighted image reconstruction scheme performs more favorably than, e.g., the drizzle method (Fruchter & Hook 2002). To increase the spatial resolution and reduce the correlation between nearby pixels, we have reduced the extent of the Gaussian kernel for the interpolation. We adopt 0.75″ for the dispersion of the Gaussian (instead of 1″ in V1.3c) and limit the kernel to a radius of 3.5″ (instead of 5″). This results in a much sharper image and a lower value for the correlated noise. In the previous pipeline V1.3c, a minimum number of 3 contributing fibers was imposed in the reconstruction of the image to achieve a homogeneous data quality across the field. With the new maximum radius in pipeline V1.5, this type of prescription results in the absence of data in the outer 2″ of the FoV, due to the wider fiber separation in the outer ring of the fiber bundle. Thus, we decided to lower this limit to 1 as the minimum number of fibers needed to fill

[3] SDSS pipeline frames that have been flat-fielded and bias-subtracted; bad columns and cosmic rays have been interpolated over and sky has been subtracted.

[4] Poor registration cases are confirmed by visual inspection of synthetic *B* and *V* broadband images and of the spectra.

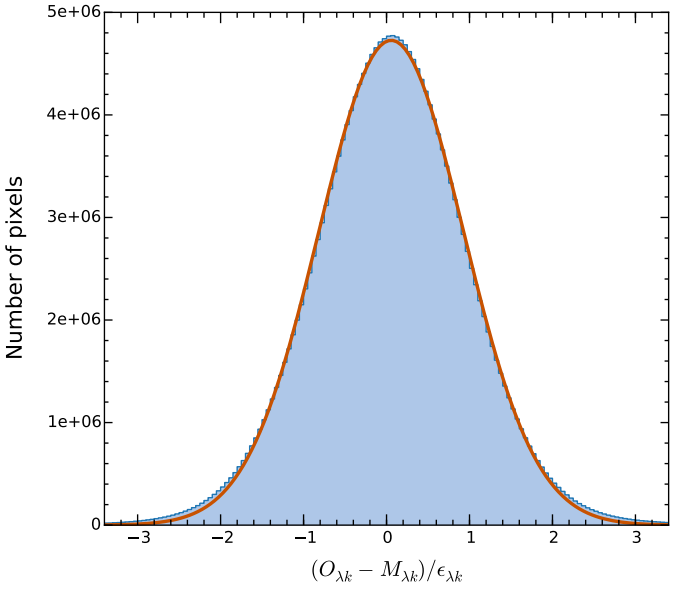

Fig. 10. Histogram of the reduced residuals $(O_{\lambda,k} - M_{\lambda,k})/\epsilon_{\lambda,k}$ for all λ's, all bins (k) and all galaxies in DR2 (209151086 points in total). The orange line shows the best Gaussian fit to the sample.

a spaxel. We have added a new header data unit (see Sect. 5.3) that records the number of fibers used to compute the total flux per spaxel. This allows the user to control which spaxels to include if a particular science case requires a minimum number of fibers for the reconstruction of the flux. The final sampling of the produced datacube is $1'' \times 1''$ per pixel.

4.3. Characterization of spatially correlated noise

Because of the interpolation procedure used to obtain a regular grid, the output pixels in the final datacube are not independent of one another. The Gaussian interpolation method distributes the flux from a given fiber between several pixels, which are combined with neighboring pixels within a certain radius, as described in Sect. 4.2. This causes the noise in the adjacent pixels to be correlated (in the spatial dimension). The correlation implies that a measurement of the noise in a stacked spectrum of N pixels will be underestimated (noise is underestimated on scales larger than pixel units). Characterizing this effect is essential for estimating the statistical errors when spectra in datacubes are coadded.

First of all, it is important to check that the error spectra derived from the pipeline for individual spaxels are reliable. Spectral fitting analysis can provide an approximate assessment of the accuracy of the error spectra. In Fig. 10 we update Fig. 9 of H13 for DR2 data. The plot shows the histogram of reduced residuals, i.e., the difference between the observed (O_λ) and synthetic (M_λ) spectra obtained with STARLIGHT in units of the corresponding error ϵ_λ (details on the fitting procedures can be found in 6.5). The distribution is very well described by a Gaussian centered at 0.03 with $\sigma = 0.87$, only slightly less than expected if residuals are purely due to uncorrelated noise.

The correlated noise can be taken into account by providing the spatial covariance (Sharp et al. 2015). However, a more practical approach consists of using the datacubes to calculate the expected rms noise[5], with the noise correlation ratio $\beta(N)$, as

[5] The noise is obtained from the detrended standard deviation in certain defined wavelength windows (see Sect. 6.6).

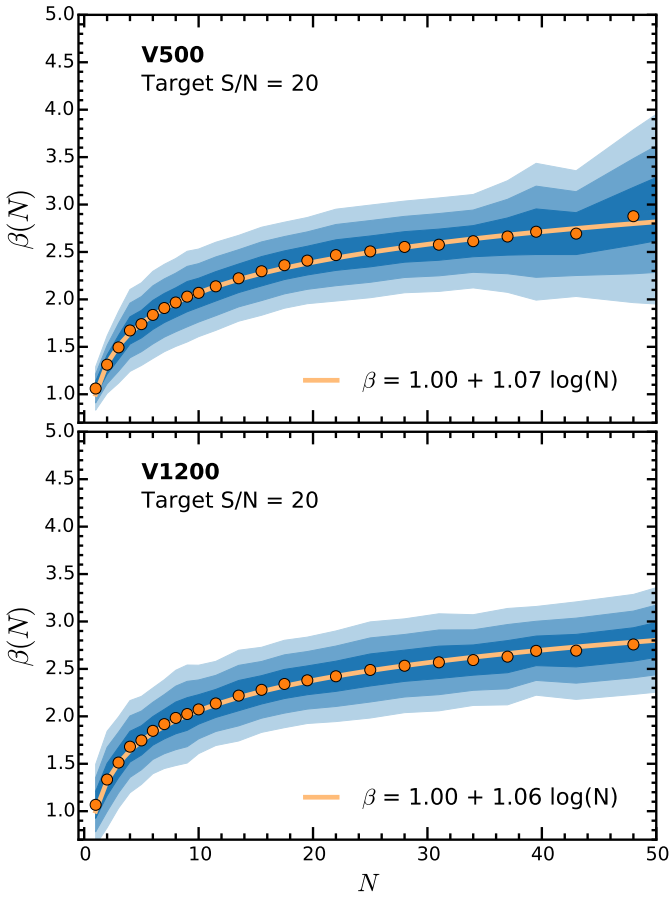

Fig. 11. Noise correlation ratio β (ratio of the real estimated error to the analytically propagated error) as a function of number of spaxels per bin for all the V500 (*upper panel*) and V1200 (*lower panel*) data of DR2 at a target S/N of 20. Shaded areas mark the 1σ, 2σ, and 3σ levels. The orange lines represent the best-fit logarithmic function with a slope $\alpha = 1.07$ and $\alpha = 1.06$, respectively.

a function of the number of pixels. To obtain a sample of coadded spaxels with different areas, we used the Voronoi adaptive binning method (implemented for optical IFS data by Cappellari & Copin 2003) with a target S/N of 20. We removed individual spaxels with $S/N < 5$ from the analysis, and coadded bins with areas larger than 60 spaxels. The β correlation ratio (or correction factor) is the ratio of the "real" or measured error to the analytically propagated error of the binned spectra as a function of bin size. The results obtained for all DR2 datacubes, shown in Fig. 11, can be well described by the logarithmic function

$$\beta(N) = 1 + \alpha \log N, \quad (1)$$

with N the number of spaxels per bin.

The values for the slope α are equal within the errors (0.01) in both setups, with a value of 1.06 for V1200 and 1.07 for V500. The slope is lower than the DR1 value (mean ~1.4), indicating that the noise in DR2 datacubes is less correlated than in DR1. This is expected since we changed the parameters in the interpolation (reducing the number of adjacent fibers contributing to a particular spaxel) and the registering method. In Appendix A we give some instructions on how to estimate the final coadded error spectrum and the limit of the application of Eq. (1).

Table 2. CALIFA FITS file structure.

HDU	Extension name	Format	Content
0	Primary	32-bit float	Flux density in units of 10^{-16} erg s^{-1} cm^{-2} Å^{-1}
1	ERROR	32-bit float	1σ error on the flux density
2	ERRWEIGHT	32-bit float	Error weighting factor
3	BADPIX	8-bit integer	Bad pixel flags (1 = bad, 0 = good)
4	FIBCOVER	8-bit integer	Number of fibers used to fill each spaxel

Table 3. Dimension and sampling of CALIFA datacubes.

Setup	N_α [a]	N_δ [a]	N_λ [a]	λ_{start} [b]	λ_{end} [c]	d_λ [d]	δ_λ [e]
V500	78	73	1877	3749 Å	7501 Å	2.0 Å	6.0 Å
V1200	78	73	1701	3650 Å	4840 Å	0.7 Å	2.3 Å

Notes. [(a)] Number of pixels in each dimension. [(b)] Wavelength of the first pixel on the wavelength direction. [(c)] Wavelength of the last pixel on the wavelength direction. [(d)] Wavelength sampling per pixel. [(e)] Homogenized spectral resolution (FWHM) over the entire wavelength range.

5. CALIFA data format and characteristics

The CALIFA data are stored and distributed as datacubes (three-dimensional data) in the standard binary FITS format and consist of several FITS Header Data Units (HDU). These datacubes contain, (1) the measured flux densities, corrected for Galactic extinction as described in S12, in units of 10^{-16} erg s^{-1} cm^{-2} Å^{-1} (primary datacube); (2) associated errors; (3) error weighting factors; (4) bad pixels flags; and (5) fiber coverage (Table 2). The last HDU is new added content absent in DR1, as explained in Sect. 4.2, but the others share the same properties as the previous data release. The first two axes of the cubes correspond to the spatial dimension along right ascension and declination with a $1'' \times 1''$ sampling. The third dimension represents the wavelength and is linearly sampled. Table 3 summarizes the dimensions of each datacube (N_α, N_δ, and N_λ), as well as the spectral sampling (d_λ) and constant resolution (δ_λ) along the entire wavelength range.

5.1. Error and weight datacubes

The 1σ noise level of each pixel as formally propagated by the pipeline can be found in the first FITS extension. Section 4.3 discusses the accuracy of the formal noise and the correlation, important when CALIFA data need to be spatially binned, and an empirical function is provided to account for the correlation effect. The second FITS extension (ERRWEIGHT) stores the error scaling factor for each pixel in the limiting case that all valid spaxels of the cube would be coadded (see also Appendix A). In the case of bad pixels, we assign an error value that is roughly ten orders of magnitude higher than the typical value.

5.2. Bad pixel datacubes

Bad pixel datacubes are stored in the third FITS extension (BADPIX). This information, in combination with the error vector, is essential to properly account for the potential problems in each spaxel. Pixels with flag =1 report the absence of sufficient information in the raw data due to cosmic rays, bad CCD colums, or the effect of vignetting[6]. These bad pixels have been interpolated over and we strongly suggest not to use them for any science analysis.

Finally, the uncovered corners of the hexagonal PPak FoV are filled with zeros and flagged as bad pixels for consistency. The residuals of bright night-sky emission lines are not flagged as bad pixels.

5.3. Fiber coverage datacubes

Pipeline V1.5 adds a new FITS extension (FIBCOVER) to the datacubes, not available in previous DR1 datacubes. As explained in Sect. 4.2 we have reduced the maximum distance of fibers that can contribute to the flux of a given spaxel. The outer hexagonal-ring of fibers do not have the same coverage as any other fiber inside the hexagon. In pipeline V1.3c we imposed a minimum of 3 fibers for computing the flux of given spaxel. In V1.5, with the new radius limit this would yield an empty outer hexagonal-ring of $\sim 2''$ in the FoV. Thus, we relax to 1 the minimum number of fibers. In order to control which spaxels have enough flux "resolution", we include a new HDU reporting the number of fibers used to account for the computed flux.

5.4. FITS header information

The FITS header contains the standard keywords that encode the information required to transform the pixel-space coordinates into sky and wavelength-space coordinates, following the World Coordinate System (WCS, Greisen & Calabretta 2002). Each CALIFA datacube contains the full FITS header information of all raw frames from which it was created. Information regarding observing and instrumental conditions such us sky brightness, flexure offsets, Galactic extinction or approximate limiting magnitude is also kept in the FITS header of each datacube. See Sect. 4.3 of H13 for nomenclature and their Table 4 for a summary of the main header keywords and meaning.

The most important new keyword added in DR2 datacubes is "REGISTER" and takes a boolean value. It indicates if a particular datacube has been successfully registered using the new method explained in Sect. 4.2 (*True*) or it has used the old V1.3c scheme (*False*). Datacubes with a *False* value are marked with a dagger in Tables 6 and 7.

6. Data quality

This second CALIFA data release (DR2) provides science-grade data for a sample of 200 galaxies, including the 100 galaxies released in the first data release (DR1), identified by an asterisk in Tables 6 and 7. As for DR1, we have run a careful quality control (QC) on the data products and selected only those

[6] The vignetting effect imprints a characteristic inhomogeneous pattern across the FoV on the bad pixels vector. See Fig. 11 of H13 for more details.

Table 4. Definition of CALIFA DR2 quality control flags for the V500 data.

QC flag	QC parameters involved	WARNING condition(s)	BAD condition(s)	Flag definition
FLAG_OBS_AM	OBS_AIRMASS_MEAN	>1.7	>2.0	Worst of the three parameters
	OBS_AIRMASS_MAX	>2.0	>2.5	
	OBS_AIRMASS_RMS	>0.15	...	
FLAG_OBS_SKYMAG	OBS_SKYMAG_MEAN	<20.5 mag_V arcsec^{-2}	<19.5	Worst of the two parameters
	OBS_SKYMAG_RMS	>0.1	...	
FLAG_OBS_EXT	OBS_EXT_MEAN	>0.30 mag	...	Worst of the three parameters
	OBS_EXT_MAX	>0.35	...	
	OBS_EXT_RMS	>0.10	...	
FLAG_RED_STRAYLIGHT	RED_MEANSTRAYLIGHT_MAX	>30 counts	>50	Worst of the three parameters
	RED_MAXSTRAYLIGHT_MAX	>50	>100	
	RED_RMSSTRAYLIGHT_MAX	>5	>10	
FLAG_RED_DISP	RED_DISP_MEAN	>5.5 Å (FWHM)	...	Worst of the three parameters
	RED_DISP_MAX	>10.0	...	
	RED_DISP_RMS	>0.5	>1.0	
FLAG_RED_CDISP	RED_CDISP_MEAN	>3.0 pixels (FWHM)	...	Worst of the three parameters
	RED_CDISP_MAX	≥4.0	...	
	RED_CDISP_RMS	>0.25	...	
FLAG_RED_SKYLINES	RED_RES5577_MIN	<−0.1 counts	...	Worst of the three parameters
	RED_RES5577_MAX	>0.1	...	
	RED_RMSRES5577_MAX	>1.0	...	
FLAG_RED_LIMSB	RED_LIMSB	<23.25 mag_V arcsec^{-2}	<22.50	
FLAG_CAL_SPECPHOTO	CAL_QFLUX_G	>0.06 dex	>0.097 dex	Worst of the three parameters
		<−0.06 dex	<−0.097 dex	combined with visual checks
	CAL_QFLUX_R	>0.06 dex	>0.097 dex	of the 30″-integrated spectrum:
		<−0.06 dex	<−0.097 dex	spectral shape and comparison
	CAL_QFLUX_RMS	>0.1	>0.2	with SDSS photometry
FLAG_CAL_WL	CAL_RMSVELMEAN	>2.0 km s^{-1}	>5.0	
FLAG_CAL_IMA	CAL_CHI2REG_MAX	>10	...	Combined parameter and visual inspection of registration and synthetic broadband image

galaxies that passed a series of QC checks in both setups (V500 and V1200), as we detail in this section. The QC checks are based on a set of measured parameters and/or visual inspection, resulting in a set of flags that allows one to quickly assess the quality of the data and their suitability for scientific use. Quantities and flags are organized into three distinct categories, related to: observing conditions (denoted by the OBS prefix); instrumental performance and effectiveness of the data reduction (RED); accuracy and quality of the final data products (CAL). The flags in each category are computed based on thresholds of measured quantities, possibly combined with flags given by human classifiers based on visual inspection, as detailed below and summarized in Tables 4 and 5. Thresholds are determined from the distribution of the parameters to exclude outliers and also to analyze the effects of anomalous parameters on the final quality of the datacubes. The tables of the relevant QC parameters, along with the QC flags, are available on the DR2 website.

Each flag can have one of the following values:

- −1 = undefined;
- 0 = good quality – OK;
- 1 = minor issues that do not significantly affect the quality – WARNING;
- 2 = significant issues affecting the quality – BAD.

By selection, DR2 excludes galaxies with BAD flags, with just a few minor exceptions affecting previously released DR1 galaxies: in these cases, the revised QC criteria adopted here would have prevented us from including these galaxies in the DR, but given the incremental nature of our data releases we keep them in the current sample.

In naming the QC parameters, we adopt the following convention: the first part is the category prefix (OBS, RED or CAL), followed by a measured parameter, and sometimes a final suffix indicating the statistics applied to combine the parameter as measured in different observations/pointings/fibers (i.e., MEAN, MIN, MAX, RMS).

In the following subsections, we describe the QCs in each of the above-mentioned categories.

6.1. Quality of the observing conditions (obs)

Three quantities are considered crucial in determining the quality of the observing conditions of the CALIFA data: the airmass, the brightness of the sky, and the atmospheric extinction. While seeing is in general an important parameter of the observing conditions, the imaging quality and spatial resolution of the CALIFA cubes is mostly limited by the sampling of the fibers on the plane of the sky and the resampling process (see Sect. 6.4.1 for more detail), rather than by the seeing. Moreover, the seeing measurement is only available for a small fraction of the objects (see Sect. 6.4.2), and therefore cannot be used as a reliable QC parameter.

For the airmass, we consider the average and the maximum airmass of the observations over all contributing pointings (OBS_AIRMASS_MEAN and OBS_AIRMASS_MAX) and its rms (OBS_AIRMASS_RMS). For each of these quantities, we defined two thresholds (the same for V500 and V1200, see Tables 6

Table 5. Definition of CALIFA DR2 quality control flags for the V1200 data.

QC flag	QC parameters involved	WARNING condition(s)	BAD condition(s)	Flag definition
FLAG_OBS_AM	OBS_AIRMASS_MEAN	>1.7	>2.0	Worst of the three parameters
	OBS_AIRMASS_MAX	>2.0	>2.5	
	OBS_AIRMASS_RMS	>0.15	...	
FLAG_OBS_SKYMAG	OBS_SKYMAG_MEAN	<21.5 mag_V arcsec^{-2}	<21.0	Worst of the two parameters
	OBS_SKYMAG_RMS	>0.1	...	
FLAG_OBS_EXT	OBS_EXT_MEAN	>0.30 mag	...	Worst of the three parameters
	OBS_EXT_MAX	>0.35	...	
	OBS_EXT_RMS	>0.10	...	
FLAG_RED_STRAYLIGHT	RED_MEANSTRAYLIGHT_MAX	>15 counts	>30	Worst of the three parameters
	RED_MAXSTRAYLIGHT_MAX	>20	>40	
	RED_RMSSTRAYLIGHT_MAX	>1.5	>2.0	
FLAG_RED_DISP	RED_DISP_MEAN	>2.0 Å (FWHM)	>2.5	Worst of the three parameters
	RED_DISP_MAX	>10.0	...	
	RED_DISP_RMS	>0.15	...	
FLAG_RED_CDISP	RED_CDISP_MEAN	>3.0 pixels (FWHM)	...	Worst of the two parameters
	RED_CDISP_RMS	>0.66	...	
FLAG_RED_SKYLINES	RED_RES4358_MIN	<−0.1 counts	...	Worst of the three parameters
	RED_RES4358_MAX	>0.1	...	
	RED_RMSRES4358_MAX	>0.7	...	
FLAG_RED_LIMSB	RED_LIMSB	<22.50 mag_B arcsec^{-2}	<22.00	
FLAG_CAL_SPECPHOTO				Visual checks on 30″-aperture integrated spectrum for spectral shape and mismatch with V500 spectrophotometry
FLAG_CAL_WL	CAL_RMSVELMEAN	>1.0 km s^{-1}	>2.0	
FLAG_CAL_IMA	CAL_CHI2 REG_MAX	>10	...	Combined parameter of visual inspection of registration and synthetic broadband image

and 7), above which the WARNING or the BAD flags, respectively, are raised. The combined FLAG_OBS_AM is the worst of the three cases.

The surface brightness of the sky in V-band during the observations is another critical parameter, which mainly limits the depth of the observations and the accuracy of the sky subtraction. The quantity SKYMAG is measured in each pointing from the sky spectrum obtained from the 36 sky fibers[7]. The mean and the rms over all pointings are considered to define the corresponding flags. Note that stricter requirements are applied to V1200 data (blue setup, high resolution) with respect to the V500 data.

The transparency of the sky during each pointing (EXT) is obtained from the monitored V band extinction at the time of the observation. We consider the following properties as symptoms of low/bad quality observations: large extinctions on average, a large maximum extinction or a large rms variation across the pointings (indicating inhomogeneous observing conditions).

6.2. Quality of the instrumental/data reduction performance (red)

The quality of the instrumental and data reduction performance is assessed via a series of four quantities measured on the reduced data *before* combining them into the final datacube: STRAYLIGHT, spectral DISPERSION, cross dispersion CDISP, and the residuals from the subtraction of bright skylines (namely, the 5577 Å O_2 line in the V500 setup and the 4358 Å HgI in the V1200 setup). In addition, we consider the limiting surface brightness corresponding to a 3σ detection per spaxel and spectral resolution element measured on the final cube.

The so-called straylight is an additional source of illumination internal to the instrument, possibly as a distributed scattered light component. Straylight, if not subtracted properly, introduces systematic errors and thus limits the final sensitivity and accuracy of the data reduction[8]. High mean levels of straylight in a frame (MEANSTRAYLIGHT), as well as high maximum values (MAXSTRAYLIGHT) and large rms (RMSSTRAYLIGHT), are indications of poor performance. Levels above the thresholds provided in Tables 4 and 5 in at least one of the exposures (_MAX suffix) raise a WARNING or a BAD FLAG_RED_STRAYLIGHT flag.

The spectral dispersion and cross dispersion are measured on individual fiber spectra as the FWHM of skylines and the FWHM of the spectral trace[9], respectively. Thresholds are set on the mean values to ensure that the typical parameters do not depart too much from the nominal target specifications, and on the maximum and rms to check for anomalies in the data. Any failure to comply with the thresholds reported in Tables 4 and 5 raises a FLAG_RED_DISP[10] or FLAG_RED_CDISP.

[7] See Appendix A.8 of H13.

[8] For a detailed description on the straylight subtraction, see Appendix A.3 of H13.

[9] The dispersed light from a fiber results in a trace with a finite extension in the spectral dispersion direction and in the spatial (cross-dispersion) direction, with a peaked, approximately Gaussian profile. We quantify the width of the trace in the spatial direction with its FWHM.

[10] The values we check for these quantities are obtained from all the fibers along the whole wavelength coverage in an intermediate step of the reduction, before final bad pixel masks are produced. It is therefore

To assess the performance of the sky subtraction, we consider the minimum and the maximum over all pointings of the average (over all fibers) flux residual of a bright skyline within an individual pointing (RED_RES4358_MIN and RED_RES4358_MAX, and RED_RES5577_MIN and RED_RES5577_MAX for the V1200 and the V500 setup, respectively). We also consider the maximum over all pointings of the rms residuals (over all fibers in an individual pointing), RED_RMSRES4358_MAX and RED_RMSRES5577_MAX. Average residuals that are too negative or too positive are indications of systematic bias in the sky subtraction. An rms that is too large can be regarded as a symptom of localized failures or noisy data. In these cases, the FLAG_RED_SKYLINES is set.

Finally, the 3σ continuum flux density detection limit per interpolated 1 arcsec^2-spaxel and spectral resolution element[11] for the faintest regions is used to identify cubes whose depth does not fulfill the survey requirements, which is reflected in the FLAG_RED_LIMSB flag. More about the depth of the final datacubes is discussed in Sect. 6.6.

6.3. Quality of the calibrated data products (cal)

The quality of the calibrated data products is determined by checks on the global spectrophotometry, on the stability of the wavelength calibration across the spectral range, and on the quality of the resulting 2D flux distribution (synthetic image) and its ability to match the SDSS broadband imaging.

The quality of global spectrophotometric calibration is assessed by comparing the photometric fluxes derived from spectra integrated within 30″-radius apertures with the corresponding fluxes derived from SDSS imaging, as explained below in Sect. 6.5. For the V500 setup, in particular, it is possible to derive the flux ratio between SDSS and CALIFA in g and r-bands (CAL_QFLUX_G and CAL_QFLUX_R, averaged over all pointings for a given galaxy): values of these ratios departing from 1 by more than the tolerances listed in Table 4 are flagged. Large rms variations of these values over the three V500 pointings (CAL_QFLUX_RMS, which combines g and r bands) are also considered symptoms of poor quality. In addition to these quantitative parameters, we visually check that the spectral energy distribution (SED) measured via SDSS photometry matches the CALIFA integrated spectrum. For this check we also consider the u and the i band data points: although the CALIFA spectra do not cover the full extent of these pass-bands, they prove helpful in judging the matching of spectral shapes. Five members of the collaboration performed these checks independently and assigned flags OK-WARNING-BAD: the second-to-worst classification is retained. This flag is then combined with the flags based on the quantitative flux ratios to create the final FLAG_CAL_SPECPHOTO flag.

to be expected that there are lower quality regions that do not comply with the requirements (i.e., spectral resolution lower than the final homogenized resolution). These regions will be eventually flagged as bad pixels. However, by how much they exceed the minimum requirement provides an indication on the overall quality of the data. By looking at the distribution of FLAG_RED_* quantities, we established a criterion to pinpoint bad cubes, where very large values of RED_DISP_MAX (and RED_DISP_MEAN, RED_DISP_RMS) occur: basically this criterion indicates when departures from nominal requirements are no longer emendable by just flagging bad pixels. Furthermore, we checked that in all the pixels that are not flagged as bad, and that the instrumental dispersion is lower than or equal to the homogenized value.

[11] See Sect. 6.6 for a definition of the wavelength range used to derive this quantity.

In order to check the stability of the wavelength calibration over the full spectral range we performed the same measurements presented in Sect. 5.3 of H13: for each galaxy and setup, the spectra within 5″ of the center of the galaxy are integrated and the systemic velocity is estimated first for the full spectrum and then for 3 (4) independent spectral ranges in V1200 (V500). The rms of these values with respect to the systemic velocity from the full spectrum (CAL_RMSVELMEAN) is an estimate of the stability of the wavelength calibration across the wavelength range and is used to set the corresponding quality flag FLAG_CAL_WL. In >97.5% of the cases, we obtain CAL_RMSVELMEAN well below 2 km s^{-1} for the V1200 and 3 km s^{-1} for the V500 grating.

Finally, the quality flag on the 2D flux distribution and plane-of-sky registration, FLAG_CAL_IMA, is defined by combining the information on the goodness of matching between SDSS images and synthetic images from the CALIFA datacube with a series of visual checks. The former is provided by the chi-squared of the registration procedure (see Sect. 4.2). The visual checks include: a check on possible artefacts in the synthetic broadband image from the final CALIFA cubes (e.g., mismatched features, elongated PSF); a comparison of the CALIFA fiber footprints of each pointing with the registered SDSS image, looking for apparent mismatched and miscomputed spatial offsets; a check of the chi-squared surface plot displaying the dependence of the registration procedure (see below) on the x and y spatial offsets, whereby irregular chi-square surfaces and lack of clear minima imply the possibility of an inaccurate registration. Out of five independent classifiers we chose the median value of the attributed flags and combine it with the flag corresponding to the chi-squared measurements. We note that a small number of objects already released as part of DR1 do not reach the imaging quality standards using the registration procedure adopted in the pipeline V1.5 (see Sect. 4.2), which uses cross-correlation with SDSS images: in these cases we revert to the old registration scheme adopted for DR1 (pipeline V1.3c) and mark the objects with a dagger in Tables 6 and 7.

6.4. Astrometric accuracy and spatial resolution

6.4.1. Astrometric registration accuracy

Pipeline V1.5 implements a new method (see Sect. 4.2) to register the absolute astrometry of the datacube coordinate system to the International Coordinate Reference System (ICRS). The previous pipeline, V1.3c, used tabulated coordinates of the galaxy V band photometric center that were assigned to the barycenter measured in the reconstructed image from the datacubes (just one point, instead of the global match applied in V1.5).

To check the accuracy of the new astrometric registration for V500 and V1200 datacubes, we performed independent tests using SDSS r and g-band images (DR10) for each galaxy. Synthetic r and g-band PPaK images were computed using the V1.5 reduced data. The coordinates of the peak centroid PPAK images are used as an approximate galactic center, and the corresponding peak was measured in the SDSS images. The offsets between the SDSS and CALIFA are less than 3″ (rms ∼1″) for the majority of the DR2 sample. Large offsets are mostly due either to edge-on galaxies, centers of the galaxies not well defined because of dust lanes, irregular morphologies or bright field star(s) near the center of the galaxy. Objects with offsets larger than 3″ measured in V500 setup are: IC1 652, NGC 0444, UGC 00809, UGC 00841, NGC 0477, IC 1683, NGC 0499, NGC 0496, NGC 0528, UGC 01938, NGC 1056, NGC 3991,

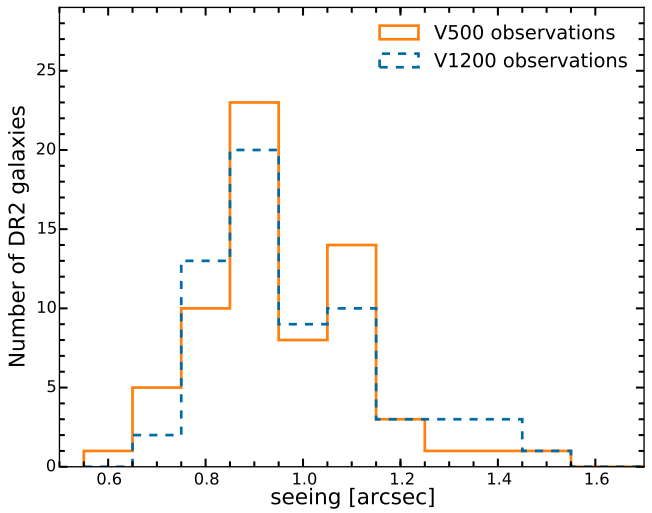

Fig. 12. Distribution of the seeing during the CALIFA observations as measured by the automatic Differential Image Motion Monitor (DIMM, Aceituno 2004).

MCG-01-01-012, and NGC 7800. For the V1200 setup: IC1 528, IC1 652, NGC 0444, UGC 00809, UGC 00841, NGC 0477, NGC 0499, NGC 0496, NGC 0528, UGC 02222, NGC 3991, UGC 11792, MCG-01-01-012, and NGC 7800.

6.4.2. Seeing and spatial resolution

To cover the complete FoV of the central bundle and to increase the final resolution of the CALIFA datacubes (PPak fibers have a diameter of 2.7″), we adopt a dithering scheme with three pointings, as described in S12. For imaging, in addition to the telescope aperture, instrumental and atmospheric seeing determine the final spatial resolution. This has to be added to the particular IFU characteristics.

The average atmospheric seeing conditions throughout CALIFA observations were derived from the measurements acquired by the DIMM (DIMM, Aceituno 2004), which operates fully automatically at the Calar Alto observatory during the night. The DIMM has different operational constraints from the 3.5 m telescope (humidity lower than 80% and wind speed less than 12 m s^{-1}). Thus seeing information is not available for every CALIFA observation and these values are missing from Tables 6 and 7, but the overall seeing distribution is not expected to be very different[12]. Figure 12 shows the DIMM seeing distribution for the DR2 sample, which has a median value of 0.″9 FWHM (the distribution is very similar to the DR1 sample), and therefore atmospheric seeing is not a limiting factor in the spatial resolution of the CALIFA cubes. At any rate, the final spatial resolution of the CALIFA data is mainly set by fiber size and the dithering and interpolation scheme.

We use the following approach to measure the PSF in the datacubes. Since January 2012 standard stars were observed using the same dithering pattern adopted for the science observations for the V500 setup. We observed a total of 107 nights in this period. Only 70% of the nights had weather conditions good enough to acquire a calibration star and 2/3 were observed adopting the dithering scheme, yielding a total of 45 datacubes. We reduced these data using the same procedure described before for the science objects. The PSF can be measured very precisely because the calibration stars have a very high S/N. We synthesize a SDSS g-band image simulated from the datacubes for each of these stars. For each of these images, we fit a 2D Moffat profile using the software IMFIT (Erwin 2015)[13]. Figure 13 shows the normalized distributions of FWHM and $\beta_{\rm M}$ parameters of the Moffat profile, weighted by the likelihood of the fit. We obtain a mean value and 1 σ scatter of the $FWHM = 2.39 \pm 0.26$ arcsec, with $\beta_{\rm M} = 1.73 \pm 0.11$. The ellipticity (1 − b/a, with a and b being the semimajor and semiminor axes, respectively) is also measured, with mean value and 1 σ scatter of 0.08 ± 0.06. Given the uncertainties, this value means the PSF can be considered effectively axisymmetric. The uncertainties in these measurements correspond to 1 σ of the distributions.

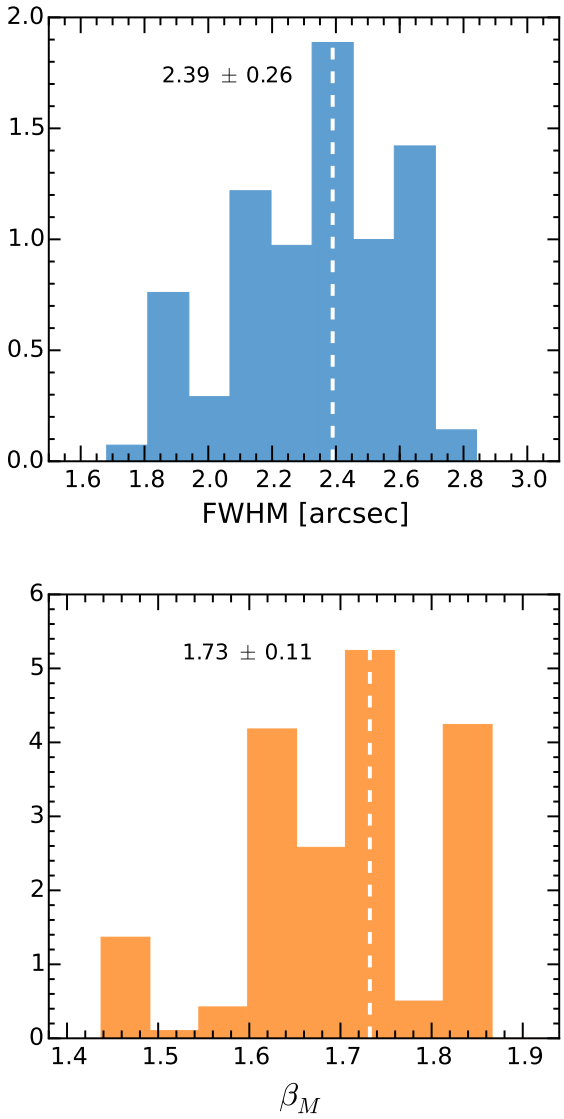

Fig. 13. Normalized distributions of PSF FWHM (*top*) and $\beta_{\rm M}$ (*bottom*) parameters of a 2D Moffat profile fitted to 45 calibration stars, weighted by the likelihood of the fit. The mean values of the distributions are marked with a white dashed line.

[12] Sánchez et al. (2008) have shown that the seeing distribution within the Dome under the standard observing conditions (i.e., with or without the DIMM monitor under operations) is very similar to the seeing distribution derived by the DIMM. In average the seeing is degradated by just 10% inside the Dome in comparison with the values provided by the DIMM.

[13] http://www.mpe.mpg.de/~erwin/code/imfit/

Table 6. CALIFA DR2 quality control parameters for the V500 data.

ID[a]	Airmass[b]	$\mu_{V,\mathrm{sky}}$[c]	A_V[d]	Seeing[e]	Flags(O)[f]	δ_λ[g]	$S/N(R_{50})$[h]	$I_{3\sigma}$[i]	Flags(R)[j]	$\left(\frac{g_{\mathrm{CALIFA}}}{g_{\mathrm{SDSS}}}\right)$[k]	$\left(\frac{r_{\mathrm{CALIFA}}}{r_{\mathrm{SDSS}}}\right)$[l]	Flags(C)[m]
001*	1.02 ± 0.01	21.4	0.18	...	000	4.68	24.8	24.0 | 0.9	00000	1.04	1.03	000
002	1.41 ± 0.05	20.9	...	...	00–	4.63	28.9	23.7 | 1.2	00000	0.96	0.98	000
003*	1.01 ± 0.01	20.8	0.23	0.8 ± 0.1	000	5.17	12.8	23.7 | 1.2	00100	0.92	0.97	100
005	1.40 ± 0.01	21.0	...	...	00–	4.65	24.3	23.6 | 1.3	00000	0.99	1.01	000
007*,†	1.34 ± 0.05	20.5	...	...	00–	5.21	27.6	23.5 | 1.4	10100	1.03	1.05	000
008	1.34 ± 0.07	21.0	0.20	...	000	4.63	29.1	23.7 | 1.1	00000	1.02	0.99	000
010*	1.31 ± 0.05	21.0	0.22	...	000	4.62	18.2	23.7 | 1.2	00000	1.01	0.98	000
013	1.57 ± 0.10	20.8	0.19	...	000	4.63	31.5	23.6 | 1.3	–00–0	0.96	1.01	001
014*	1.26 ± 0.04	21.0	0.21	...	000	4.62	22.0	23.8 | 1.1	00000	1.03	1.01	000
017	1.23 ± 0.03	21.1	...	...	00–	4.61	9.2	23.6 | 1.3	00000	1.00	1.00	000
022	1.18 ± 0.05	20.9	...	...	00–	4.76	24.8	23.6 | 1.3	10000	0.94	0.94	100
023	1.86 ± 0.03	19.7	0.15	...	110	4.87	14.6	22.8 | 2.7	10011	0.92	0.98	000
025	1.24 ± 0.04	21.0	0.17	...	000	4.63	17.9	23.6 | 1.3	00000	0.98	1.02	001
026	1.26 ± 0.02	20.9	0.13	...	000	4.82	26.3	23.8 | 1.1	00000	0.99	1.00	000
027	1.90 ± 0.01	20.1	0.20	...	110	4.71	30.3	23.5 | 1.5	00010	1.00	1.04	001
030	1.34 ± 0.04	20.9	0.20	...	000	4.65	30.1	23.9 | 1.0	00000	0.99	1.04	101
037	1.58 ± 0.11	20.8	0.17	...	000	4.68	34.7	24.0 | 0.9	00000	1.20	1.25	101
039*	1.03 ± 0.01	20.8	0.23	0.9 ± 0.1	000	5.21	15.6	23.8 | 1.1	01000	0.95	0.99	110
040	1.29 ± 0.06	21.1	0.17	...	000	4.69	24.4	24.0 | 0.9	00000	0.99	1.00	010
041	1.09 ± 0.03	21.1	0.14	...	000	4.95	21.0	23.8 | 1.1	00010	1.02	1.01	000
042*	1.10 ± 0.03	21.0	0.13	...	000	5.21	14.3	23.6 | 1.3	10000	1.08	1.09	101
043*	1.01 ± 0.01	21.3	0.19	...	000	4.79	29.5	23.9 | 1.0	–00–0	1.05	1.02	001
044	1.17 ± 0.04	21.0	...	...	00–	4.79	22.3	23.2 | 1.8	00001	0.96	0.96	000
045	1.28 ± 0.06	20.8	0.14	...	000	5.22	12.6	23.3 | 1.7	10000	0.98	1.03	001
050	1.43 ± 0.08	20.9	0.16	...	000	4.89	37.7	23.7 | 1.2	00000	0.99	1.02	000
053*	1.19 ± 0.04	20.7	...	0.8 ± 0.1	00–	5.25	27.4	23.7 | 1.2	00100	0.95	0.98	000
072	1.16 ± 0.03	21.1	0.15	...	000	4.84	27.3	23.8 | 1.1	00000	1.00	1.02	000
073*	1.04 ± 0.01	21.1	0.20	...	000	4.73	18.6	23.3 | 1.8	00000	1.01	1.01	000
076	1.15 ± 0.03	21.2	0.12	...	000	4.95	16.4	23.4 | 1.6	10000	0.96	0.97	111
077	1.43 ± 0.07	20.9	0.19	...	000	4.64	37.1	23.9 | 1.0	00000	1.05	1.11	101
088*	1.13 ± 0.03	20.8	...	1.0 ± 0.4	00–	5.43	23.7	23.4 | 1.5	01100	0.97	0.99	101
100*	1.37 ± 0.26	20.7	0.14	...	100	5.24	23.5	23.1 | 2.1	10001	0.99	1.00	001
103	1.42 ± 0.08	20.9	0.19	...	000	4.69	28.3	23.6 | 1.3	00000	1.01	1.05	001
104	1.62 ± 0.10	20.8	...	...	00–	4.73	9.4	23.6 | 1.3	00000	1.01	1.00	000
115	1.28 ± 0.02	20.6	...	...	00–	4.67	16.6	23.6 | 1.3	00010	0.98	0.99	000
127*	1.22 ± 0.02	20.6	0.28	0.9 ± 0.1	000	5.12	11.1	23.0 | 2.2	00001	0.93	0.98	000
131	1.20 ± 0.01	21.0	...	...	00–	4.72	22.2	23.3 | 1.8	00000	0.98	0.97	000
133	1.17 ± 0.02	20.6	0.28	0.8 ± 0.1	000	5.13	13.8	23.1 | 2.1	00001	0.88	0.95	100
134	1.47 ± 0.04	21.0	...	...	00–	5.26	20.9	23.2 | 1.9	10101	0.88	0.93	101
141	1.42 ± 0.03	21.0	...	...	00–	4.72	11.3	23.8 | 1.1	00000	1.01	0.97	111
146*,†	1.47 ± 0.00	20.7	0.12	...	000	5.79	15.4	23.0 | 2.2	01101	1.03	1.02	001
147	1.15 ± 0.01	21.2	0.14	...	000	5.63	22.7	23.2 | 1.8	01101	0.98	1.00	100
148	1.34 ± 0.04	20.9	0.11	...	000	5.01	17.0	23.6 | 1.2	10000	1.04	0.93	101
149	1.14 ± 0.01	21.4	...	...	00–	5.78	24.8	22.9 | 2.4	11101	0.86	0.91	101
150	1.01 ± 0.01	21.1	...	...	00–	4.76	24.0	23.8 | 1.1	00000	1.00	0.98	010
151*	1.07 ± 0.02	21.0	0.15	...	000	5.85	18.7	23.0 | 2.2	11001	0.88	0.91	101

Notes. We describe the meaning of each column, including the identifier of each column in the electronic table available on the DR2 web page. [(a)] IDs marked with an asterisk were already part of the DR1. A dagger indicates cubes that were registered with the old method of the pipeline V1.3c. [(b)] Mean airmass (OBS_AIR_MEAN) and rms (OBS_AIR_RMS) of the observations for the frames used to create the considered datacube. [(c)] Average night-sky surface brightness (OBS_SKY_MAG) in the V band during the observations in units of mag arcsec^{-2}. [(d)] Average night-sky attenuation (OBS_EXT_MEAN) in the V band during the observations in magnitudes. [(e)] Average natural seeing (OBS_SEEING_MEAN) in the V-band during the observations in arcsec (FWHM). [(f)] Observation quality flags, combining the three individual column flags (FLAG_OBS_AM, FLAG_OBS_SKYMAG, FLAG_OBS_EXT) as described in Sect. 6. [(g)] Average spectral resolution (RED_DISP_MEAN) in Å (FWHM), measured by fitting the night-sky emission lines with single Gaussian functions. [(h)] Average signal-to-noise ratio (CAL_SNR1HLR) estimated for the full wavelength range at one half-light radius from the center. [(i)] Average flux at the 3σ continuum detection limit in units of V-band mag arcsec^{-2} and in units of 10^{-18} erg s^{-1} cm^{-2}Å^{-1} arcsec^{-2}. [(j)] Reduction/instrumental performance quality flags, combining the five individual column flags (FLAG_RED_STRAYLIGHT, FLAG_RED_DISP, FLAG_RED_CDISP, FLAG_RED_SKYLINES, FLAG_RED_LIMSB) as described in Sect. 6. [(k)] Ratio between the SDSS g band flux derived from the datacube and the derived from the SDSS images for a 30″-diameter aperture (CAL_QFLUX_G). [(l)] Ratio between the SDSS r band flux derived from the datacube and the derived from the SDSS images for a 30″-diameter aperture (CAL_QFLUX_R). [(m)] Quality control flags, combining the three individual column flags (FLAG_CAL_SPECPHOTO, FLAG_CAL_WL, FLAG_CAL_IMA) as described in Sect. 6.

Table 6. continued.

ID[a]	Airmass[b]	$\mu_{V,\mathrm{sky}}$[c]	A_V[d]	Seeing[e]	Flags(O)[f]	δ_λ[g]	$S/N(R_{50})$[h]	$I_{3\sigma}$[i]	Flags(R)[j]	$\left(\frac{g_{\mathrm{CALIFA}}}{g_{\mathrm{SDSS}}}\right)$[k]	$\left(\frac{r_{\mathrm{CALIFA}}}{r_{\mathrm{SDSS}}}\right)$[l]	Flags(C)[m]
153	1.19 ± 0.04	21.1	...	...	00–	4.90	25.6	23.7 | 1.2	00000	0.98	0.99	000
155*	1.03 ± 0.01	21.1	0.16	...	000	5.61	14.8	23.1 | 2.0	11001	0.94	0.94	001
156*	1.12 ± 0.04	21.0	0.16	...	000	5.54	19.4	23.3 | 1.7	11000	0.99	1.00	001
165	1.03 ± 0.01	21.1	0.15	...	000	5.98	23.6	23.0 | 2.2	11001	0.92	0.93	100
231	1.03 ± 0.01	21.2	...	...	00–	4.89	8.7	23.9 | 1.0	00000	1.00	0.99	000
232	1.07 ± 0.00	21.1	...	...	00–	4.70	17.1	23.6 | 1.3	00010	1.02	1.01	000
272	1.15 ± 0.01	21.1	...	...	00–	5.19	27.3	23.3 | 1.7	10000	0.97	0.97	000
273*	1.06 ± 0.01	21.1	0.14	...	000	5.33	21.5	23.6 | 1.3	00000	0.98	1.00	001
274*	1.18 ± 0.02	20.9	...	...	00–	4.92	30.1	23.7 | 1.2	00000	1.02	1.03	001
275	1.14 ± 0.00	21.0	...	...	00–	4.93	35.7	23.7 | 1.2	01000	0.99	1.01	000
277*	1.60 ± 0.12	20.3	0.33	...	011	5.65	15.9	22.8 | 2.8	11101	0.95	1.01	101
278	1.32 ± 0.08	20.8	0.12	...	000	5.33	25.8	23.6 | 1.3	00100	1.04	1.05	000
306*	1.28 ± 0.08	20.6	0.17	1.0 ± 0.1	000	4.59	6.5	23.6 | 1.4	00010	1.01	0.96	101
307*	1.06 ± 0.01	21.2	0.16	...	000	5.64	14.3	23.5 | 1.4	01000	0.97	0.97	001
309*	1.27 ± 0.05	21.0	0.15	...	000	5.97	12.8	23.1 | 2.1	11001	0.99	0.99	001
311	1.03 ± 0.01	21.3	0.16	...	000	5.96	7.1	23.0 | 2.2	11001	0.87	0.86	101
314	1.13 ± 0.05	21.1	0.15	1.1 ± 0.1	000	4.99	31.1	24.0 | 0.9	00000	1.05	1.07	001
319*	1.11 ± 0.03	20.5	0.56	...	001	5.54	21.7	23.3 | 1.8	01100	0.91	1.00	001
326*	1.05 ± 0.01	20.8	...	...	00–	4.66	24.8	23.9 | 1.0	00000	1.00	1.02	000
340	1.27 ± 0.05	20.9	...	1.1 ± 0.2	00–	5.21	12.7	23.8 | 1.1	01000	0.93	0.95	100
341*	1.17 ± 0.03	...	0.17	1.5 ± 0.2	0–0	5.06	17.0	23.7 | 1.2	00000	1.01	1.03	000
353	1.03 ± 0.02	20.9	...	...	00–	4.74	20.8	23.3 | 1.7	00000	0.98	1.00	001
364*	1.33 ± 0.07	20.8	0.12	...	000	5.39	34.0	23.8 | 1.1	00100	1.01	1.05	000
381	1.01 ± 0.00	21.2	...	...	00–	4.77	32.5	23.9 | 1.0	00000	1.04	1.03	001
388	1.02 ± 0.01	21.1	...	0.2 ± 0.2	00–	5.18	7.8	23.2 | 1.9	00001	0.95	0.94	000
436	1.13 ± 0.03	21.1	0.19	...	000	...	21.7	23.1 | 2.1	0–011	0.97	0.98	000
475*,†	1.35 ± 0.07	20.8	0.12	...	000	5.36	21.2	23.7 | 1.2	00000	0.96	1.03	110
476	1.06 ± 0.02	20.8	...	...	00–	4.75	64.0	23.9 | 1.0	00010	1.01	1.03	100
479*	1.14 ± 0.03	20.8	...	...	00–	4.67	28.4	23.9 | 0.9	00010	1.02	1.03	000
486*	1.05 ± 0.03	...	0.16	1.2 ± 0.7	0–0	4.66	22.3	24.0 | 0.9	00000	0.99	0.98	000
502	1.11 ± 0.01	21.3	...	...	00–	5.04	40.3	24.0 | 0.9	00000	1.09	1.07	100
515*	1.01 ± 0.00	20.9	0.14	...	000	5.25	14.9	23.2 | 1.9	00001	0.95	0.98	000
518*	1.16 ± 0.01	20.9	0.15	...	000	5.64	18.6	23.3 | 1.7	01100	0.97	1.00	000
528*	1.14 ± 0.01	20.8	...	...	00–	4.71	7.5	23.7 | 1.2	00000	1.01	1.02	001
548*	1.16 ± 0.01	20.8	0.19	1.2 ± 0.1	000	4.64	43.6	23.8 | 1.1	00010	1.02	1.00	001
569	1.06 ± 0.01	21.2	...	...	00–	4.65	33.8	24.1 | 0.8	10000	0.96	1.01	000
577*,†	1.02 ± 0.01	21.0	0.15	...	000	4.95	13.3	24.0 | 0.9	01100	...	...	–0–
592	1.03 ± 0.01	20.9	...	...	00–	4.69	20.0	23.3 | 1.7	00000	0.82	0.84	101
593	1.11 ± 0.02	21.0	...	...	00–	4.73	19.5	23.9 | 1.0	00000	0.98	0.99	000
606	1.07 ± 0.01	21.4	...	...	00–	5.19	15.8	23.9 | 1.0	00000	0.95	1.00	101
607*	1.22 ± 0.03	21.3	0.16	...	000	5.39	41.2	23.6 | 1.3	10000	0.91	0.92	100
608*	1.31 ± 0.06	21.1	...	...	00–	5.87	11.3	23.3 | 1.7	11000	0.91	0.91	101
609*	1.07 ± 0.02	21.3	0.14	...	000	5.55	17.3	23.8 | 1.1	01000	0.99	0.97	100
610*	1.11 ± 0.03	21.2	...	...	00–	5.85	22.7	23.5 | 1.5	11000	0.96	0.97	000
630	1.36 ± 0.04	20.0	...	...	01–	4.64	17.6	23.4 | 1.6	00000	0.99	1.00	001
633	1.13 ± 0.01	21.0	...	...	00–	4.77	13.8	23.7 | 1.2	00000	0.93	0.96	000
657*	1.02 ± 0.01	21.2	0.19	1.1 ± 0.1	000	4.69	10.4	23.9 | 1.0	00000	1.01	1.00	000
663*	1.20 ± 0.04	20.9	...	...	00–	5.32	24.4	23.7 | 1.2	01000	1.01	1.02	100
664*	1.04 ± 0.02	21.2	...	1.1 ± 0.1	00–	5.21	35.6	23.9 | 0.9	00000	1.05	1.06	000
665*	1.06 ± 0.01	21.1	...	...	00–	5.21	18.8	23.7 | 1.2	00000	1.02	1.03	100
676*	1.03 ± 0.03	21.0	0.15	...	000	5.52	12.5	23.2 | 1.8	–10–1	0.96	0.97	100
680*	1.07 ± 0.02	21.0	...	...	00–	4.66	11.8	24.1 | 0.8	00010	1.00	1.03	000
684*	1.05 ± 0.02	21.0	...	...	00–	4.66	25.1	23.5 | 1.5	00000	0.97	0.99	000
708	1.18 ± 0.03	20.8	...	...	00–	4.76	18.8	23.0 | 2.2	00011	0.93	0.95	000
714	1.09 ± 0.01	20.6	0.14	...	000	4.66	28.1	23.8 | 1.0	00010	1.03	1.02	000
715	1.10 ± 0.06	21.1	0.21	...	000	4.74	35.9	24.0 | 0.9	–00–0	1.02	1.04	101
740	1.12 ± 0.03	21.0	...	...	00–	4.66	30.0	23.3 | 1.7	00000	0.96	0.99	001
749	1.08 ± 0.02	21.1	0.19	1.1 ± 0.1	000	4.90	28.9	24.0 | 0.9	00000	1.03	1.04	100
758*	1.02 ± 0.00	21.1	0.24	1.1 ± 0.1	000	4.72	12.2	24.0 | 0.9	00000	0.96	0.97	000
764*	1.29 ± 0.05	21.1	0.18	1.0 ± 0.1	000	4.62	20.0	24.0 | 0.9	00000	1.07	1.02	000
769*	1.02 ± 0.01	21.2	...	...	00–	5.47	18.7	23.6 | 1.3	01100	1.00	1.00	000
778	1.15 ± 0.04	21.2	...	0.9 ± 0.1	00–	4.77	25.3	23.6 | 1.4	00000	0.99	1.00	000

Table 6. continued.

ID[a]	Airmass[b]	$\mu_{V,\mathrm{sky}}$[c]	A_V[d]	Seeing[e]	Flags(O)[f]	δ_λ[g]	$S/N(R_{50})$[h]	$I_{3\sigma}$[i]	Flags(R)[j]	$\left(\frac{g_{\mathrm{CALIFA}}}{g_{\mathrm{SDSS}}}\right)$[k]	$\left(\frac{r_{\mathrm{CALIFA}}}{r_{\mathrm{SDSS}}}\right)$[l]	Flags(C)[m]
783*	1.08 ± 0.02	21.3	0.16	...	000	5.46	29.3	23.6 | 1.3	00010	0.98	0.98	000
789	1.15 ± 0.03	21.1	0.20	0.9 ± 0.1	000	4.64	27.3	24.0 | 0.9	00010	0.99	0.99	000
791	1.16 ± 0.03	20.9	...	...	00–	4.78	35.6	23.5 | 1.4	00000	0.99	1.01	001
795	1.01 ± 0.00	21.1	...	0.8 ± 0.1	00–	4.71	27.7	23.9 | 1.0	00000	0.97	1.00	000
797*	1.05 ± 0.07	21.0	0.15	...	000	5.11	17.6	24.0 | 0.9	01100	0.99	1.00	000
798*	1.05 ± 0.02	21.3	0.21	...	000	4.66	27.0	24.3 | 0.7	00000	0.97	1.00	000
806*	1.00 ± 0.00	21.1	0.25	1.1 ± 0.1	000	4.70	59.9	23.6 | 1.3	00000	0.85	0.86	101
807	1.16 ± 0.04	20.9	...	...	00–	4.67	18.3	23.4 | 1.5	00010	0.99	1.00	100
809	1.35 ± 0.05	21.0	...	1.0 ± 0.5	00–	4.85	16.2	23.3 | 1.8	00000	0.84	0.87	101
813	1.08 ± 0.01	20.9	0.22	1.4 ± 0.1	000	4.65	19.4	23.6 | 1.4	00010	0.98	0.99	000
815	1.21 ± 0.05	21.1	0.18	0.8 ± 0.1	000	4.82	11.6	23.6 | 1.3	00000	0.96	0.98	000
816	1.21 ± 0.04	20.7	...	0.8 ± 0.1	00–	4.67	34.2	23.8 | 1.1	00010	1.02	1.02	001
820*	1.07 ± 0.02	21.2	0.17	...	000	5.61	7.2	22.9 | 2.5	21001	1.03	1.03	101
822*	1.03 ± 0.01	21.2	...	...	00–	6.08	10.1	23.1 | 2.1	11001	0.96	0.96	101
823*	1.15 ± 0.00	20.9	0.19	...	000	4.62	21.3	23.8 | 1.1	10010	0.99	0.98	000
824*,†	1.14 ± 0.01	20.9	...	...	00–	4.72	22.9	23.9 | 1.0	00000	0.92	0.89	101
826*	1.18 ± 0.03	21.1	...	...	00–	5.32	26.4	23.7 | 1.2	00100	1.03	1.04	000
828*	1.21 ± 0.03	21.3	0.26	0.9 ± 0.1	000	4.64	27.2	24.0 | 0.9	00000	1.11	1.04	101
829*	1.09 ± 0.01	21.2	0.18	...	000	4.73	17.7	23.4 | 1.6	10000	0.95	0.93	101
831	1.42 ± 0.07	20.2	...	...	01–	4.65	22.3	23.3 | 1.7	00000	1.03	1.02	000
832*	1.01 ± 0.01	21.3	...	...	00–	5.49	23.4	23.5 | 1.5	00100	0.98	0.99	100
833*	1.12 ± 0.03	21.2	0.18	0.9 ± 0.1	000	5.00	18.1	23.8 | 1.1	00100	1.02	0.98	000
834	1.39 ± 0.07	20.5	0.29	...	010	4.70	28.0	23.9 | 1.0	00000	1.17	1.23	101
835*	1.00 ± 0.00	21.1	...	1.1 ± 0.2	00–	5.28	38.2	24.0 | 0.9	01000	0.98	1.01	000
837*	1.11 ± 0.00	21.1	0.17	0.9 ± 0.1	000	4.84	43.0	24.1 | 0.8	01000	1.07	1.03	001
838	1.46 ± 0.09	20.3	...	...	01–	4.65	25.7	23.6 | 1.4	00000	1.06	1.06	000
840*	1.18 ± 0.04	21.0	0.28	0.9 ± 0.1	000	4.65	3.0	23.5 | 1.4	00000	1.02	0.96	100
841	1.16 ± 0.04	21.2	...	0.9 ± 0.1	00–	4.71	24.0	23.6 | 1.3	00000	1.01	1.03	001
843*	1.45 ± 0.09	21.0	0.23	0.8 ± 0.1	000	4.60	9.3	23.8 | 1.1	00000	1.08	1.05	011
845*	1.03 ± 0.02	21.4	0.19	...	000	4.64	16.0	23.8 | 1.1	00000	0.93	0.95	100
846*	1.06 ± 0.02	21.0	0.39	0.8 ± 0.1	001	4.64	7.7	23.7 | 1.2	00000	0.97	0.98	000
847*	1.31 ± 0.09	21.3	0.15	0.7 ± 0.1	010	4.66	20.4	24.0 | 0.9	20000	1.16	1.25	101
848*	1.10 ± 0.00	21.0	0.38	0.9 ± 0.1	001	4.74	32.3	23.8 | 1.1	00000	1.02	1.01	000
850*	1.05 ± 0.01	21.0	0.29	...	000	4.66	29.6	23.7 | 1.2	00000	1.00	1.01	000
851*	1.32 ± 0.04	20.5	0.41	0.7 ± 0.1	001	4.66	9.5	23.3 | 1.7	00010	0.93	0.93	100
852*	1.12 ± 0.01	21.0	0.36	0.9 ± 0.1	001	4.76	8.1	23.8 | 1.1	00000	1.01	0.99	000
854*	1.18 ± 0.03	20.7	0.42	0.9 ± 0.1	001	4.68	20.3	23.6 | 1.3	00010	1.00	1.01	001
856*	1.05 ± 0.02	21.2	0.17	...	000	4.61	24.1	23.9 | 1.0	00000	0.99	0.99	000
857*	1.08 ± 0.00	21.5	0.16	0.9 ± 0.1	000	4.67	36.7	24.2 | 0.8	00000	0.98	1.01	000
858*	1.10 ± 0.03	21.2	0.15	1.3 ± 0.2	000	4.67	15.8	23.7 | 1.2	00000	1.01	0.98	000
859*	1.16 ± 0.02	21.2	0.15	0.7 ± 0.1	000	4.67	11.0	23.6 | 1.4	00000	0.92	0.95	000
860*	1.04 ± 0.02	21.2	0.29	1.0 ± 0.1	000	4.60	41.5	23.6 | 1.3	00000	1.10	1.06	101
861	1.08 ± 0.02	21.1	...	...	00–	4.62	22.4	23.5 | 1.4	00000	1.04	1.06	001
862	1.13 ± 0.03	20.8	...	1.1 ± 0.2	00–	5.19	20.3	23.4 | 1.6	00100	0.99	1.01	001
863*	1.09 ± 0.01	21.4	0.16	0.7 ± 0.1	000	4.67	29.4	24.1 | 0.8	00000	1.02	1.05	001
864*	1.06 ± 0.01	20.9	0.28	...	000	4.70	12.2	23.5 | 1.5	20010	0.99	0.98	100
865*	1.01 ± 0.01	21.2	0.25	...	000	4.71	32.4	23.9 | 1.0	10000	1.01	1.02	001
866*	1.04 ± 0.02	21.3	0.21	1.1 ± 0.1	000	4.64	12.6	24.0 | 0.9	20000	1.04	1.02	000
867*	1.13 ± 0.01	21.2	0.21	1.1 ± 0.1	000	4.69	39.2	24.0 | 0.9	10000	1.08	1.09	001
868	1.65 ± 0.04	20.1	...	...	01–	4.84	25.3	23.3 | 1.7	–00–0	0.96	0.99	001
869	1.41 ± 0.06	20.8	0.19	1.1 ± 0.1	000	4.66	16.4	23.5 | 1.5	00000	1.04	1.02	101
871	1.38 ± 0.01	20.6	0.17	0.9 ± 0.1	000	4.70	21.3	23.4 | 1.6	–00–0	0.99	1.02	100
872*	1.28 ± 0.01	20.9	0.15	0.6 ± 0.1	000	4.66	18.2	23.4 | 1.5	00010	0.98	0.98	000
874*	1.10 ± 0.02	21.0	0.22	...	000	4.75	24.4	23.2 | 1.9	00001	1.01	1.03	101
877*,†	1.24 ± 0.05	21.0	0.22	...	000	4.72	16.8	23.6 | 1.3	20000	1.23	1.23	101
878*	1.33 ± 0.01	20.9	0.22	0.9 ± 0.1	000	4.59	6.8	23.7 | 1.1	00010	1.01	0.99	101
880	1.24 ± 0.03	20.7	0.29	0.9 ± 0.1	000	4.63	24.2	23.6 | 1.3	00010	0.93	0.94	100
881*	1.10 ± 0.00	21.1	0.15	0.8 ± 0.1	000	4.67	18.2	23.8 | 1.1	00010	0.94	0.94	000
883*	1.10 ± 0.01	21.2	0.17	1.0 ± 0.2	000	4.63	10.1	23.6 | 1.3	00000	0.99	0.95	101
884	1.66 ± 0.10	20.4	...	...	01–	4.90	10.8	23.4 | 1.5	00000	0.97	0.98	110
885	1.25 ± 0.04	20.9	0.20	0.7 ± 0.1	000	4.88	25.4	23.7 | 1.2	00100	1.04	1.01	001
886	1.29 ± 0.04	21.0	0.17	0.9 ± 0.2	000	4.65	40.5	23.4 | 1.5	00000	1.01	1.00	000

Table 6. continued.

ID[a]	Airmass[b]	$\mu_{V,\mathrm{sky}}$[c]	A_V[d]	Seeing[e]	Flags(O)[f]	δ_λ[g]	$S/N(R_{50})$[h]	$I_{3\sigma}$[i]	Flags(R)[j]	$\left(\frac{g_{\mathrm{CALIFA}}}{g_{\mathrm{SDSS}}}\right)$[k]	$\left(\frac{r_{\mathrm{CALIFA}}}{r_{\mathrm{SDSS}}}\right)$[l]	Flags(C)[m]
887*	1.08 ± 0.02	21.3	0.17	0.9 ± 0.1	000	4.67	31.9	23.9 | 1.0	00000	1.01	0.98	001
888*	1.01 ± 0.01	20.9	0.22	...	000	4.68	2.5	23.5 | 1.5	00010	0.93	0.94	000
890*	1.08 ± 0.02	21.0	0.22	...	000	4.71	29.9	23.9 | 1.0	00010	1.00	1.01	000
891	1.37 ± 0.06	20.3	0.21	1.2 ± 0.2	010	5.23	9.2	23.1 | 2.0	00101	0.91	0.98	000
893*	1.35 ± 0.07	20.5	0.20	1.0 ± 0.1	000	5.32	6.9	22.9 | 2.6	20111	0.89	0.92	111
894	1.31 ± 0.06	20.5	...	0.9 ± 0.1	00–	4.74	21.3	23.6 | 1.3	00010	1.06	1.11	101
895	1.15 ± 0.03	20.5	0.22	1.1 ± 0.1	000	5.15	10.3	23.5 | 1.4	00000	0.94	0.97	100
896*	1.36 ± 0.08	20.8	0.18	0.9 ± 0.1	000	5.01	21.8	23.8 | 1.1	00100	1.04	1.02	001
898	1.60 ± 0.11	20.4	...	0.9 ± 0.1	01–	4.66	12.4	22.9 | 2.5	00011	0.97	1.00	000
901*	1.10 ± 0.03	21.3	0.14	1.0 ± 0.1	000	4.63	29.9	23.7 | 1.2	20000	0.97	1.03	101
902*	1.10 ± 0.00	21.2	0.17	0.8 ± 0.1	000	4.71	39.3	23.6 | 1.3	00000	1.06	1.01	001
903	1.45 ± 0.08	20.9	...	...	00–	4.64	30.5	23.3 | 1.8	00000	0.97	0.97	001
904*	1.20 ± 0.04	21.0	0.17	0.9 ± 0.1	000	4.71	21.5	23.6 | 1.4	00000	1.01	0.98	000
909	1.09 ± 0.02	20.8	...	...	00–	5.05	29.5	23.8 | 1.1	00000	1.02	1.00	000
910	1.22 ± 0.03	21.1	...	...	00–	4.62	18.7	23.4 | 1.6	00000	0.99	1.01	101
913	1.47 ± 0.09	21.1	...	...	00–	4.63	38.8	23.4 | 1.6	00000	0.96	1.01	100
914	1.18 ± 0.02	21.0	0.13	...	000	4.79	31.4	23.8 | 1.1	00000	0.98	1.00	000
915	1.28 ± 0.05	21.1	...	...	00–	4.61	25.4	23.4 | 1.6	00000	1.06	1.03	000
916	1.55 ± 0.10	20.8	...	...	00–	4.65	25.0	23.0 | 2.2	00001	0.95	0.99	101
917	1.21 ± 0.03	20.9	...	...	00–	4.69	31.5	23.5 | 1.4	00010	1.03	1.00	100
922	1.15 ± 0.00	20.8	0.14	...	000	5.20	16.8	23.5 | 1.5	00100	1.06	1.08	101
924	1.43 ± 0.12	20.6	...	...	00–	4.79	12.8	23.0 | 2.3	–00–1	1.01	1.00	000
927	1.29 ± 0.03	21.0	...	...	00–	4.64	14.7	23.8 | 1.1	00000	1.01	1.02	000
930	1.29 ± 0.03	20.8	...	...	00–	4.62	7.3	23.1 | 2.1	00011	1.03	1.04	010
932	1.27 ± 0.02	21.0	...	...	00–	4.71	33.5	23.7 | 1.2	00000	1.00	1.00	100
935*	1.04 ± 0.02	21.0	...	1.1 ± 0.1	00–	5.09	11.1	23.7 | 1.2	00000	0.96	1.00	000
936	1.42 ± 0.05	20.8	0.15	...	000	4.84	30.7	24.0 | 0.9	00000	1.06	1.11	101
937	1.13 ± 0.02	21.0	...	...	00–	4.62	13.8	23.7 | 1.2	00010	0.99	0.97	000
938	1.01 ± 0.01	...	0.16	...	0–0	4.74	31.5	24.0 | 0.9	00000	0.98	1.00	100
939*	1.11 ± 0.04	20.8	0.15	...	000	4.99	8.7	23.6 | 1.3	01110	1.05	1.03	100

As a consequence of the improvements in the interpolation scheme, the PSF FWHM has substantially decreased with respect to DR1 (pipeline V1.3c). The improvement in spatial resolution is illustrated on the Hα maps presented in Fig. 15. This figure shows Hα maps obtained using FIT3D on the CALIFA datacubes for NGC 5406 (ID 684) for DR1, DR2, and one image taken with the *William Herschel* Telescope (WHT) using a narrowband filter. The last image has also been degraded to the DR2 nominal resolution for the sake of comparison. This improvement impacts directly, for example, on the detection rate of H II regions. Using HIIEXPLORER (Sánchez et al. 2012b) on the V1.3c datacubes of the 200 galaxies, a total of 5878 are recovered, while this number rises to 7646 H II regions for the DR2 galaxies using pipeline V1.5, which represents an increase of ~30%.

6.5. Spectrophotometric accuracy

As mentioned in Sect. 4.2, the new registration scheme of the pipeline uses *r*-band for the V500 setup and *g*-band for the V1200 of the SDSS DR7. Each V500 datacube is rescaled in the absolute flux level to match the SDSS DR7 broadband photometry using the photometric scale factor at the best matching position for each pointing. On the other hand, the V1200 data is matched to the V500 data (S12). This procedure, together with the new recalibrated sensitivity curve (see Sect. 4.2 and Husemann et al., in prep.), improves the spectrophotometric calibration over DR1. This is clearly shown in Fig. 14. As part of the CALIFA pipeline V1.5, a 30″ diameter photometric aperture in r and g is measured both in the SDSS DR7 images and the equivalent synthetic CALIFA broadband images. The mean SDSS/CALIFA g and r band ratios in DR2 and their scatter are 1.00 ± 0.05 and 0.99 ± 0.06, respectively. In the right panel of Fig. 14 the distribution in $\Delta(g-r)$ color difference between the SDSS and CALIFA data shows that the spectrophotometric accuracy across the wavelength range is better that 3%, with a median value of 0.01 ± 0.03.

Spectral fitting methods can be used to perform useful tests of the data and their calibration, and this has been done before in CALIFA. H13 used STARLIGHT fits to evaluate the accuracy of the error estimates in DR1 datacubes, while Cid Fernandes et al. (2014) used these fits to map systematic features in the spectral residuals that may indicate calibration issues.

We repeated the same experiments for the DR2 datacubes. Results are shown in Fig. 16. The top panel shows in blue the mean spectrum of 170670 Voronoi bins of the 200 galaxies in DR2[14]. The average is taken after normalizing each spectrum by its median flux in the 5635 ± 45 Å window. The mean synthetic spectrum (overplotted orange line) as well as the mean residual (at the bottom of the upper panel, purple line) are also plotted. The middle panel zooms in on the residual spectrum, which now excludes emission lines and bad pixels, which are masked in the fitting process. Finally, the bottom panel shows what fraction of all spectra was used in the statistics at each λ.

[14] The spatial binning is used to guarantee a minimum S/N of 20 in the continuum at ~5635 Å. In practice, 88% of the Voronoi bins actually comprise a single spaxel.

Table 7. CALIFA DR2 quality control parameters for the V1200 data.

ID[a]	Airmass[b]	$\mu_{V,\mathrm{sky}}$[c]	A_V[d]	Seeing[e]	Flags(O)[f]	δ_λ[g]	$S/N(R_{50})$[h]	$I_{3\sigma}$[i]	Flags(R)[j]	Flags(C)[k]
001*	1.01 ± 0.02	...	0.26	...	0–0	1.90	9.0	23.2 | 3.3	00000	000
002	1.32 ± 0.04	21.8	0.13	...	000	1.94	12.4	23.3 | 3.0	00000	000
003*	1.08 ± 0.06	22.0	0.17	...	000	1.96	6.5	23.3 | 2.9	11000	000
005	1.44 ± 0.05	21.8	0.16	...	000	1.94	13.2	23.4 | 2.8	–00–0	100
007*†	1.18 ± 0.02	21.7	0.14	...	000	1.96	10.2	22.8 | 4.9	00000	001
008	1.04 ± 0.03	21.9	0.43	...	001	1.90	10.2	23.2 | 3.3	00010	000
010*	1.29 ± 0.09	22.2	...	...	00–	1.92	6.1	23.0 | 4.1	00000	001
013	1.53 ± 0.04	21.8	0.14	...	000	1.94	16.0	23.4 | 2.9	00010	100
014*	1.27 ± 0.08	22.2	0.19	...	000	1.90	11.4	23.3 | 3.0	00000	000
017	1.19 ± 0.03	21.9	...	...	00–	1.94	4.4	23.5 | 2.5	00000	001
022	1.12 ± 0.08	22.4	0.15	...	000	1.99	6.2	22.7 | 5.3	–00–0	001
023	1.89 ± 0.07	...	...	...	1–	1.96	8.7	22.9 | 4.3	10010	000
025	1.22 ± 0.06	22.0	0.15	...	000	1.94	8.5	23.1 | 3.5	00010	101
026	1.27 ± 0.03	21.8	...	...	00–	1.91	10.5	23.4 | 2.7	00010	000
027	1.93 ± 0.05	21.3	0.13	...	110	1.95	14.0	23.2 | 3.2	10000	101
030	1.28 ± 0.03	21.9	0.14	...	000	1.94	17.2	23.7 | 2.1	00000	001
037	1.02 ± 0.01	22.2	...	...	00–	1.93	15.7	23.7 | 2.0	00010	001
039*	1.07 ± 0.04	22.1	0.21	1.1 ± 0.2	000	1.96	9.3	23.6 | 2.3	01000	000
040	1.03 ± 0.03	22.2	0.21	...	000	1.93	11.0	23.5 | 2.5	00000	000
041	1.02 ± 0.02	22.3	...	...	00–	1.90	9.9	23.5 | 2.6	00000	000
042*	1.19 ± 0.09	22.3	0.15	0.9 ± 0.1	000	2.01	9.1	23.6 | 2.3	01000	101
043*	1.01 ± 0.01	22.3	0.27	...	000	1.90	11.1	23.4 | 2.7	00000	000
044	1.05 ± 0.04	22.4	0.11	...	000	1.97	7.4	22.7 | 5.3	00110	000
045	1.01 ± 0.01	22.4	0.14	1.2 ± 0.2	000	1.99	9.2	23.5 | 2.4	00000	001
050	1.14 ± 0.07	22.3	0.14	...	000	2.06	16.2	23.2 | 3.3	01000	101
053*	1.33 ± 0.17	21.9	0.16	...	100	2.13	10.3	23.1 | 3.5	01110	000
072	1.13 ± 0.04	21.9	0.12	...	000	1.94	11.4	23.4 | 2.8	00000	000
073*	1.08 ± 0.04	22.2	0.26	...	000	1.91	7.2	22.9 | 4.3	00000	001
076	1.23 ± 0.08	22.2	0.11	...	000	2.09	4.6	22.6 | 5.6	01100	001
077	1.17 ± 0.01	21.8	...	...	00–	1.94	17.3	23.6 | 2.3	00010	001
088*	1.31 ± 0.13	21.4	0.21	...	010	1.99	9.1	22.7 | 5.1	01100	011
100*	1.36 ± 0.14	21.8	0.15	1.1 ± 0.1	000	2.00	13.2	23.1 | 3.7	01000	001
103	1.09 ± 0.09	22.2	...	...	00–	2.01	11.3	22.8 | 4.8	01100	001
104	1.26 ± 0.03	21.9	0.14	...	000	1.94	5.0	23.5 | 2.6	00000	001
115	1.34 ± 0.09	22.1	0.15	...	000	2.01	5.3	22.7 | 5.2	01100	101
127*	1.37 ± 0.27	21.7	0.15	...	100	1.99	4.2	22.5 | 6.4	–00–1	000
131	1.19 ± 0.00	22.3	0.14	...	000	1.99	7.0	22.3 | 7.7	–00–1	000
133	1.13 ± 0.01	21.9	0.16	...	000	2.00	5.5	22.5 | 6.4	–10–1	101
134	1.37 ± 0.01	22.0	...	...	00–	2.00	10.0	23.1 | 3.5	01000	000
141	1.37 ± 0.02	22.0	0.15	...	000	1.98	5.1	23.0 | 4.1	00100	001
146*,†	1.48 ± 0.01	22.2	0.14	1.3 ± 0.2	000	2.00	10.7	23.3 | 2.9	01000	001
147	1.16 ± 0.02	22.3	0.14	1.1 ± 0.1	000	1.95	16.3	23.6 | 2.3	00010	001
148	1.29 ± 0.06	22.1	0.12	...	000	1.93	8.2	23.4 | 2.7	00000	001
149	1.27 ± 0.06	22.2	0.11	...	000	1.92	13.2	23.0 | 4.1	10000	001
150	1.06 ± 0.04	22.2	0.15	...	000	1.93	12.4	23.3 | 3.0	10000	000
151*	1.52 ± 0.19	21.4	...	...	11–	2.04	9.7	22.9 | 4.4	01100	001
153	1.09 ± 0.03	21.6	...	...	00–	1.97	10.7	23.1 | 3.4	–00–0	001
155*	1.09 ± 0.05	22.1	0.13	0.9 ± 0.1	000	2.33	4.8	22.5 | 6.2	21110	001
156*	1.08 ± 0.05	22.3	0.14	...	000	2.36	8.1	22.6 | 5.6	01100	001
165	1.25 ± 0.11	21.7	...	...	00–	1.94	15.7	23.1 | 3.5	00100	000

Notes. We describe the meaning of each column including the identifier of each column in the electronic table available on the DR2 web page. [(a)] IDs marked with an asterisk were already part of the DR1. A dagger indicates cubes that were registered with the old method of the pipeline V1.3c. [(b)] Mean airmass (OBS_AIR_MEAN) and rms (OBS_AIR_RMS) of the observations for the frames used to create the considered datacube. [(c)] Average night-sky surface brightness (OBS_SKY_MAG) in the V band during the observations in units of mag arcsec^{-2}. [(d)] Average night-sky attenuation (OBS_EXT_MEAN) in the V band during the observations in magnitudes. [(e)] Average natural seeing (OBS_SEEING_MEAN) in the V-band during the observations in arcsec (FWHM). [(f)] Observation quality flags, combining the three individual column flags (FLAG_OBS_AM, FLAG_OBS_SKYMAG, FLAG_OBS_EXT) as described in Sect. 6. [(g)] Average spectral resolution (RED_DISP_MEAN) in Å (FWHM), measured by fitting the night-sky emission lines with single Gaussian functions. [(h)] Average signal-to-noise ratio (CAL_SNR1HLR) estimated for the full wavelength range at one half-light radius from the center. [(i)] Average flux at the 3σ continuum detection limit in units of B-band mag arcsec^{-2} and in units of 10^{-18} erg s^{-1} cm^{-2}Å^{-1} arcsec^{-2}. [(j)] Reduction/instrumental performance quality flags, combining the five individual column flags (FLAG_RED_STRAYLIGHT, FLAG_RED_DISP, FLAG_RED_CDISP, FLAG_RED_SKYLINES, FLAG_RED_LIMSB) as described in Sect. 6. [(k)] Quality control CAL flags, combining the three individual column flags (FLAG_CAL_SPECPHOTO, FLAG_CAL_WL, FLAG_CAL_IMA) as described in Sect. 6.

Table 7. continued.

ID[a]	Airmass[b]	$\mu_{V,\mathrm{sky}}$[c]	A_V[d]	Seeing[e]	Flags(O)[f]	δ_λ[g]	$S/N(R_{50})$[h]	$I_{3\sigma}$[i]	Flags(R)[j]	Flags(C)[k]
231	1.06 ± 0.03	22.3	...	...	00–	1.92	5.4	23.5 | 2.5	10000	001
232	1.31 ± 0.12	21.9	0.11	...	000	1.96	9.8	23.5 | 2.4	00010	101
272	1.13 ± 0.03	22.1	...	...	00–	2.09	9.2	22.8 | 5.0	01010	000
273*	1.06 ± 0.01	22.2	0.14	1.1 ± 0.1	000	2.01	12.6	23.6 | 2.3	01000	000
274*	1.30 ± 0.09	22.0	...	...	00–	2.05	10.7	23.0 | 4.0	01100	000
275	1.16 ± 0.02	22.4	0.15	...	000	1.99	9.2	22.4 | 6.7	–00–1	000
277*	1.08 ± 0.04	21.7	0.15	...	000	2.13	12.0	23.0 | 4.0	01010	001
278	1.09 ± 0.05	22.5	0.11	...	000	2.24	7.4	22.8 | 4.8	01100	100
306*	1.14 ± 0.03	21.3	...	...	01–	2.02	3.5	23.2 | 3.4	21100	001
307*	1.20 ± 0.08	22.2	0.15	0.8 ± 0.1	000	2.33	4.8	22.7 | 5.2	11100	001
309*	1.25 ± 0.08	22.1	0.14	...	000	2.38	6.3	22.8 | 4.8	01100	000
311	1.03 ± 0.03	22.4	...	...	00–	2.02	4.2	22.9 | 4.3	01100	000
314	1.05 ± 0.01	22.4	0.12	...	000	1.92	11.5	23.2 | 3.3	–00–0	001
319*	1.07 ± 0.06	22.2	0.15	1.1 ± 0.1	000	1.99	12.5	23.6 | 2.3	–01–0	000
326*	1.29 ± 0.05	21.9	...	...	00–	2.02	5.4	22.7 | 5.0	01100	001
340	1.08 ± 0.02	22.5	...	...	00–	2.01	4.0	23.0 | 3.9	01100	001
341*	1.21 ± 0.08	22.0	0.16	1.2 ± 0.1	000	1.91	7.9	23.4 | 2.7	00100	001
353	1.04 ± 0.03	22.5	0.10	...	000	2.07	9.4	23.3 | 2.9	01010	001
364*	1.02 ± 0.02	22.1	...	0.9 ± 0.1	00–	2.03	15.8	23.3 | 2.9	11000	001
381	1.01 ± 0.01	22.2	...	...	00–	1.96	12.4	23.6 | 2.4	–00–0	000
388	1.33 ± 0.11	22.1	...	...	00–	2.15	2.3	22.4 | 6.7	01111	101
436	1.10 ± 0.03	21.4	...	...	01–	1.96	11.1	23.0 | 3.9	–00–0	001
475*,†	1.13 ± 0.07	22.1	...	...	00–	2.03	11.6	23.3 | 2.9	21010	101
476	1.40 ± 0.28	21.8	...	...	10–	2.02	25.5	22.9 | 4.5	01100	001
479*	1.16 ± 0.03	22.3	...	...	00–	2.05	7.2	22.7 | 5.3	01100	001
486*	1.21 ± 0.10	22.1	0.15	0.8 ± 0.1	000	1.99	8.6	23.5 | 2.5	10100	100
502	1.23 ± 0.08	21.9	...	...	00–	1.93	11.6	22.5 | 6.1	00000	001
515*	1.20 ± 0.09	22.3	0.15	0.9 ± 0.1	000	2.30	4.2	22.6 | 5.5	11110	000
518*	1.18 ± 0.03	22.6	0.13	...	000	2.03	12.6	23.3 | 2.9	01100	000
528*	1.48 ± 0.08	22.0	...	...	00–	2.10	2.0	22.7 | 5.5	01100	110
548*	1.21 ± 0.05	21.9	0.18	0.8 ± 0.1	000	2.00	14.6	23.2 | 3.3	10000	100
569	1.16 ± 0.05	22.0	0.15	...	000	1.95	15.0	23.5 | 2.4	00000	001
577*,†	1.06 ± 0.04	22.2	0.22	...	000	1.89	6.5	23.6 | 2.3	00100	00–
592	1.03 ± 0.02	22.3	...	...	00–	2.25	4.9	22.6 | 5.5	01100	000
593	1.15 ± 0.05	21.9	...	...	00–	1.95	8.3	23.5 | 2.6	00000	010
606	1.33 ± 0.09	22.1	0.17	...	000	1.94	10.4	23.6 | 2.3	00000	001
607*	1.25 ± 0.07	22.3	0.14	...	000	2.25	16.7	23.1 | 3.7	01000	000
608*	1.20 ± 0.10	21.9	0.16	...	000	1.92	6.3	23.2 | 3.3	00000	000
609*	1.08 ± 0.05	22.4	0.15	0.8 ± 0.1	000	2.28	6.8	23.0 | 3.9	11100	011
610*	1.17 ± 0.07	22.5	...	...	00–	2.14	8.9	23.0 | 4.1	11100	100
630	1.26 ± 0.06	22.4	...	...	00–	1.92	10.7	23.3 | 2.9	00000	000
633	1.55 ± 0.12	22.0	...	...	00–	1.92	4.3	23.2 | 3.3	00010	000
657*	1.09 ± 0.05	22.4	0.19	1.5 ± 0.2	000	1.90	5.3	23.7 | 2.1	00000	000
663*	1.10 ± 0.02	22.0	...	...	00–	1.98	11.8	23.3 | 2.9	01000	001
664*	1.07 ± 0.04	22.0	0.26	1.2 ± 0.1	000	1.96	16.2	23.4 | 2.7	00000	001
665*	1.17 ± 0.10	22.1	0.10	...	000	1.95	5.1	22.8 | 4.6	00000	001
676*	1.01 ± 0.02	22.5	0.17	0.8 ± 0.1	000	2.26	4.6	22.9 | 4.2	01100	001
680*	1.07 ± 0.05	22.4	0.10	...	000	1.95	5.4	23.7 | 2.0	00000	000
684*	1.06 ± 0.04	22.3	0.13	0.9 ± 0.1	000	1.96	13.0	23.4 | 2.8	00000	001
708	1.12 ± 0.04	22.2	...	...	00–	1.91	7.7	23.0 | 4.0	00010	000
714	1.43 ± 0.12	21.9	...	...	00–	1.93	12.6	23.4 | 2.7	–00–0	001
715	1.18 ± 0.06	21.9	0.22	...	000	2.00	18.7	23.6 | 2.3	00000	001
740	1.05 ± 0.04	22.8	...	...	00–	2.24	4.4	22.2 | 8.3	01011	001
749	1.07 ± 0.04	22.3	...	...	00–	2.06	13.2	23.4 | 2.7	11010	001
758*	1.18 ± 0.05	22.2	0.26	1.0 ± 0.1	001	1.89	5.5	23.4 | 2.7	–00–0	100
764*	1.11 ± 0.04	...	0.16	...	0–0	2.02	7.7	23.6 | 2.4	01100	001
769*	1.03 ± 0.02	22.2	...	...	00–	2.00	9.6	23.3 | 3.1	01000	000
778	1.02 ± 0.01	22.5	...	...	00–	2.13	8.8	23.2 | 3.3	01000	000
783*	1.20 ± 0.07	22.3	0.17	...	000	2.29	11.3	22.9 | 4.2	01000	000
789	1.10 ± 0.05	22.1	...	...	00–	1.95	12.4	23.5 | 2.6	00000	000
791	1.08 ± 0.02	22.6	...	...	00–	2.28	9.0	22.7 | 5.1	01110	001
795	1.23 ± 0.09	22.3	...	...	00–	1.92	12.3	23.5 | 2.6	00000	000
797*	1.06 ± 0.04	22.5	0.17	1.3 ± 0.2	000	1.89	8.4	23.6 | 2.4	00000	000
798*	1.13 ± 0.07	22.2	0.30	0.8 ± 0.1	001	1.93	8.1	23.4 | 2.8	00000	001

Table 7. continued.

ID[a]	Airmass[b]	$\mu_{V,\mathrm{sky}}$[c]	A_V[d]	Seeing[e]	Flags(O)[f]	δ_λ[g]	$S/N(R_{50})$[h]	$I_{3\sigma}$[i]	Flags(R)[j]	Flags(C)[k]
806*	1.06 ± 0.05	22.2	0.21	1.1 ± 0.1	000	1.90	29.0	23.5 | 2.4	00010	000
807	1.30 ± 0.19	22.0	...	...	10–	1.96	9.8	23.5 | 2.5	–00–0	001
809	1.30 ± 0.08	21.7	...	...	00–	1.95	8.2	23.2 | 3.2	00010	001
813	1.07 ± 0.02	22.3	...	...	00–	2.05	8.7	23.1 | 3.7	01010	000
815	1.15 ± 0.10	22.2	...	...	00–	2.05	3.8	23.1 | 3.7	–10–0	001
816	1.15 ± 0.06	22.2	...	...	00–	2.08	12.1	23.3 | 3.0	11010	001
820*	1.15 ± 0.10	22.3	0.15	0.7 ± 0.1	000	2.35	4.3	22.7 | 5.4	–11–0	101
822*	1.09 ± 0.05	22.1	0.16	0.8 ± 0.1	000	1.91	7.4	23.4 | 2.9	00000	000
823*	1.17 ± 0.03	22.0	0.26	0.9 ± 0.1	000	1.91	10.3	23.3 | 3.1	00000	001
824*,†	1.18 ± 0.04	21.6	0.24	1.1 ± 0.2	000	1.98	6.4	22.6 | 5.7	00000	001
826*	1.16 ± 0.04	22.0	...	...	00–	2.10	10.9	22.9 | 4.5	–11–0	001
828*	1.17 ± 0.04	22.6	0.16	1.0 ± 0.1	000	1.89	12.4	23.6 | 2.2	10000	000
829*	1.24 ± 0.07	22.0	0.17	1.4 ± 0.2	000	1.95	7.1	23.3 | 2.9	01110	000
831	1.18 ± 0.05	21.3	0.17	...	010	1.95	12.5	23.1 | 3.6	10000	000
832*	1.02 ± 0.02	22.1	...	...	00–	2.00	10.4	23.4 | 2.9	–10–0	001
833*	1.07 ± 0.03	22.2	0.10	...	000	1.95	4.6	22.9 | 4.4	00000	001
834	1.27 ± 0.10	22.3	0.23	...	000	2.04	10.5	23.5 | 2.5	01010	001
835*	1.04 ± 0.03	22.3	0.16	1.0 ± 0.1	000	1.95	16.8	23.6 | 2.2	00000	000
837*	1.15 ± 0.04	22.2	0.14	0.8 ± 0.1	000	1.98	22.1	23.6 | 2.3	00100	001
838	1.32 ± 0.12	21.9	...	...	00–	2.03	14.6	23.4 | 2.7	01010	001
840*	1.24 ± 0.09	22.1	0.10	...	000	1.95	1.8	23.2 | 3.2	00000	000
841	1.40 ± 0.09	21.8	0.15	...	000	1.94	9.5	23.1 | 3.6	–00–0	000
843*	1.11 ± 0.05	22.4	0.26	...	000	1.92	5.6	23.5 | 2.6	00000	001
845*	1.19 ± 0.15	21.7	0.28	0.8 ± 0.1	100	1.93	4.5	23.2 | 3.3	–00–0	000
846*	1.17 ± 0.07	22.0	0.25	...	000	1.95	3.3	23.3 | 2.9	00000	000
847*	1.03 ± 0.03	21.9	0.32	0.8 ± 0.1	001	1.93	7.9	23.1 | 3.5	00010	001
848*	1.24 ± 0.12	...	0.28	1.0 ± 0.1	0–1	1.88	13.9	23.2 | 3.3	–00–0	001
850*	1.05 ± 0.02	22.0	0.19	0.8 ± 0.1	000	1.93	12.3	23.3 | 3.0	00000	000
851*	1.12 ± 0.04	22.1	0.28	0.9 ± 0.1	000	1.89	5.0	23.2 | 3.4	00000	000
852*	1.38 ± 0.09	21.6	0.19	1.4 ± 0.2	000	1.99	3.6	23.4 | 2.7	01100	001
854*	1.20 ± 0.06	22.0	0.37	0.9 ± 0.1	001	1.88	9.0	23.2 | 3.3	20000	001
856*	1.05 ± 0.03	22.7	0.24	0.9 ± 0.1	001	1.91	7.0	22.8 | 4.7	–00–0	001
857*	1.10 ± 0.02	22.4	0.21	0.9 ± 0.1	000	1.95	14.8	23.5 | 2.6	00000	000
858*	1.25 ± 0.14	22.1	0.23	0.9 ± 0.1	000	1.98	5.5	23.1 | 3.7	–00–0	001
859*	1.18 ± 0.05	22.2	0.32	0.7 ± 0.1	001	1.93	3.7	23.0 | 3.9	00010	000
860*	1.04 ± 0.02	22.3	0.27	0.9 ± 0.3	001	1.91	20.4	23.1 | 3.4	00010	001
861	1.32 ± 0.13	22.2	...	...	00–	1.96	8.7	23.0 | 3.8	10010	001
862	1.09 ± 0.04	22.2	...	1.1 ± 0.1	00–	1.95	14.3	23.4 | 2.6	00000	001
863*	1.20 ± 0.06	22.3	0.19	0.9 ± 0.1	000	1.95	10.7	23.3 | 3.0	00010	001
864*	1.05 ± 0.02	22.4	0.20	...	000	1.96	6.7	23.5 | 2.6	00010	000
865*	1.02 ± 0.02	22.3	0.27	0.9 ± 0.1	000	1.93	13.0	23.4 | 2.8	00010	001
866*	1.08 ± 0.05	22.1	0.34	...	001	1.96	4.7	23.5 | 2.5	00000	101
867*	1.13 ± 0.01	22.1	0.39	...	001	1.96	16.4	23.2 | 3.3	00000	001
868	1.74 ± 0.13	21.5	0.15	...	110	2.01	12.2	23.0 | 4.1	01100	001
869	1.35 ± 0.01	22.0	0.22	...	000	1.92	5.8	22.9 | 4.4	00000	001
871	1.40 ± 0.04	21.7	...	...	00–	1.95	11.0	23.0 | 3.8	00110	000
872*	1.37 ± 0.05	21.7	0.22	1.0 ± 0.1	000	1.94	6.5	23.0 | 4.1	–00–0	001
874*	1.14 ± 0.05	21.8	0.31	0.8 ± 0.1	001	1.95	9.7	23.1 | 3.6	00010	001
877*,†	1.10 ± 0.05	...	0.22	1.0 ± 0.1	0–0	1.94	5.1	22.9 | 4.3	10010	001
878*	1.37 ± 0.07	22.1	0.18	1.1 ± 0.1	000	1.91	4.1	23.5 | 2.5	00000	001
880	1.25 ± 0.07	22.0	...	0.9 ± 0.1	00–	1.91	8.7	22.8 | 4.9	00000	001
881*	1.17 ± 0.11	22.0	0.30	0.9 ± 0.2	000	1.96	5.3	23.2 | 3.4	–00–0	000
883*	1.13 ± 0.04	22.1	0.31	0.9 ± 0.1	001	1.90	2.6	22.7 | 5.1	00000	001
884	1.49 ± 0.13	21.8	...	...	00–	2.01	5.8	23.0 | 3.9	01000	101
885	1.15 ± 0.00	22.1	...	...	00–	1.93	12.4	23.3 | 3.1	–00–0	000
886	1.32 ± 0.09	22.0	0.19	0.9 ± 0.1	000	1.99	13.8	22.3 | 7.3	00011	001
887*	1.05 ± 0.01	22.2	0.29	0.8 ± 0.1	000	1.89	10.4	23.1 | 3.8	–00–0	001
888*	1.08 ± 0.05	21.9	0.41	...	001	2.01	1.3	23.1 | 3.8	01000	000
890*	1.02 ± 0.01	21.8	0.23	0.9 ± 0.1	000	1.94	10.8	23.4 | 2.9	–00–0	000
891	1.20 ± 0.03	22.1	...	...	00–	1.94	4.1	23.0 | 4.1	10110	000
893*	1.40 ± 0.21	21.8	0.15	1.0 ± 0.1	100	1.95	3.2	22.8 | 4.6	–00–0	001
894	1.03 ± 0.01	22.5	...	...	00–	1.98	8.0	23.1 | 3.7	10100	101
895	1.12 ± 0.03	21.9	...	...	00–	1.99	5.2	23.2 | 3.4	–00–0	001
896*	1.03 ± 0.02	22.3	0.14	1.4 ± 0.3	000	2.13	8.3	23.2 | 3.3	01100	000

Table 7. continued.

ID[a]	Airmass[b]	$\mu_{V,\mathrm{sky}}$[c]	A_V[d]	Seeing[e]	Flags(O)[f]	δ_λ[g]	$S/N(R_{50})$[h]	$I_{3\sigma}$[i]	Flags(R)[j]	Flags(C)[k]
898	1.20 ± 0.09	22.2	0.24	...	000	1.97	6.1	22.6 | 5.9	00100	000
901*	1.20 ± 0.10	22.1	0.25	1.0 ± 0.2	000	2.02	10.7	22.9 | 4.5	01010	000
902*	1.38 ± 0.14	21.7	0.21	1.1 ± 0.1	000	1.97	17.0	23.2 | 3.3	00010	001
903	1.26 ± 0.07	21.9	0.12	...	000	1.95	12.6	22.8 | 4.6	00010	000
904*	1.27 ± 0.08	21.7	0.22	1.3 ± 0.3	000	1.99	9.2	23.0 | 3.9	00000	101
909	1.29 ± 0.11	21.9	0.12	...	000	1.95	7.6	22.5 | 6.1	00000	001
910	1.28 ± 0.06	21.8	...	...	00–	2.05	6.8	23.0 | 4.0	–10–0	000
913	1.24 ± 0.10	22.1	...	...	01–	2.24	13.4	22.9 | 4.3	01100	001
914	1.16 ± 0.02	22.0	...	...	00–	1.92	12.4	23.2 | 3.4	00010	101
915	1.30 ± 0.11	22.0	...	...	00–	1.90	12.2	23.3 | 3.1	00010	001
916	1.21 ± 0.07	22.2	0.13	...	000	2.00	12.0	22.9 | 4.4	01010	000
917	1.12 ± 0.01	22.4	0.20	...	000	1.93	11.6	23.0 | 3.9	00010	001
922	1.23 ± 0.06	22.0	0.14	...	000	1.94	11.0	23.4 | 2.7	00000	100
924	1.32 ± 0.06	21.9	...	...	00–	1.94	10.4	23.3 | 3.1	00000	101
927	1.29 ± 0.05	22.0	0.11	...	000	1.98	3.9	22.7 | 5.1	00000	001
930	1.27 ± 0.05	21.9	...	...	00–	1.90	7.8	23.5 | 2.4	00000	000
932	1.29 ± 0.05	21.8	0.12	...	000	1.95	10.6	23.3 | 3.0	00000	001
935*	1.09 ± 0.06	22.3	0.18	...	000	2.13	4.5	23.4 | 2.8	01100	000
936	1.45 ± 0.13	21.6	...	...	00–	1.94	7.0	23.0 | 3.9	–00–0	001
937	1.16 ± 0.04	22.1	0.19	...	000	1.98	7.1	23.2 | 3.2	–01–0	101
938	1.13 ± 0.07	...	0.23	1.0 ± 0.1	0–0	1.94	12.6	23.4 | 2.8	00000	000
939*	1.32 ± 0.08	21.9	0.28	0.9 ± 0.1	001	1.89	5.2	23.3 | 3.0	–00–0	000

The layout of Fig. 16 is identical to Fig. 13 of Cid Fernandes et al. (2014), to which it should be compared[15]. Focusing on the middle panel, one sees that from ∼5000 Å to the red the residuals are very similar, including the humps around 5800 Å associated with the imperfect removal of telluric features. Toward the blue however, the new reduction pipeline leads to smaller residuals. For instance, the broad feature around Hβ seen with V1.3c spectra is essentially eliminated by the new reduction. A systematic excess blueness persists for $\lambda < 3900$ Å, but overall the improvement is clear.

Residuals for the 200 DR2 nuclear spectra are shown in Fig. 17, where galaxies are sorted by redshift and stacked. This visualization facilitates the identification of telluric features, which appear as slanted lines in the image. Comparison with an identical plot in H13 (their Fig. 16) shows the improvements achieved with the new pipeline.

6.6. Limiting sensitivity and signal-to-noise

To assess the depth of the data, we estimated the 3σ continuum flux density detection limit per interpolated 1 arcsec^2-spaxel and spectral resolution element for the faintest regions. Figure 18 shows the limiting continuum sensitivity of the spectrophotometrically recalibrated CALIFA spectra. The depth is plotted against the average S/N per 1 arcsec^2 and spectral resolution element within an elliptical annulus of ±1″ around the galaxies' r-band half-light semimajor axis (HLR), with PA and radius values taken from W14. A narrow wavelength window at 4480–4520 Å for the V1200 and at 5590–5680 Å for the V500 was used to estimate both values[16]. These small windows are nearly free of stellar absorption features or emission lines. The 3σ continuum flux density detection limit per spaxel and spectral resolution element[17] for the V1200 data ($I_{3\sigma} = 3.2 \times 10^{-18}$ erg s^{-1} cm^{-2} Å^{-1} arcsec^{-2} in the median at 4500 Å) is a factor of ∼2–3 brighter than for the V500 data ($I_{3\sigma} = 1.2 \times 10^{-18}$ erg s^{-1} cm^{-2} Å^{-1} arcsec^{-2} in the median at 5635 Å) mainly because of the difference in spectral resolution. These continuum sensitivities can be transformed into equivalent limiting broadband surface brightnesses of 23.0 mag arcsec^{-2} in the g-band for the V1200 data and 23.4 mag arcsec^{-2} in the r-band for the V500. The variance of the sky brightness of each night might be one of the main factors causing the dispersion in the limiting continuum sensitivity. Dust attenuation, transparency of the night, and other atmospheric conditions might also affect the depth achievable at fixed exposure times.

The limiting sensitivity is a measure of the noise and thus it correlates mildly with the S/N. The mean S/N in the continuum per 1 arcsec^2 and spectral resolution element at the half-light semimajor axis (HLR) of all objects is ∼9.5 for the V1200 setup, while it is ∼22.2 for the V500 data. Thus, we achieve a $S/N \gtrapprox 10$ for a significant number of the objects even for the V1200 setup.

7. Access to the CALIFA DR2 data

7.1. The CALIFA DR2 search and retrieval tool

The public data are distributed through the CALIFA DR2 web page[18]. A simple web form interface, already in use for the first data release, allows the user to select data of a particular target galaxy, or a subsample of objects within some constraints on observing conditions or galaxy properties. Among the selection parameters, we include the instrument setup, galaxy coordinates, redshift, g-band magnitudes, observing date, Hubble type, bar strength, inclination estimated from axis ratio, V band atmospheric attenuation, airmass, and relative accuracy of the SDSS/CALIFA photometric calibration.

[15] Fig. 13 in Cid Fernandes et al. (2014) is in fact busier than our Fig. 16, as it shows results obtained with three different spectral bases. Here we adopt the same base described in González Delgado et al. (2014b), which is very similar to base *GM* in Cid Fernandes et al. (2014).

[16] The signal (also used for the surface brightness limit) is computed as the median value in the defined wavelength intervals, while the noise is the detrended standard deviation in the same windows.

[17] Note that this is a continuum flux density. See Note 5 of H13.

[18] http://califa.caha.es/DR2

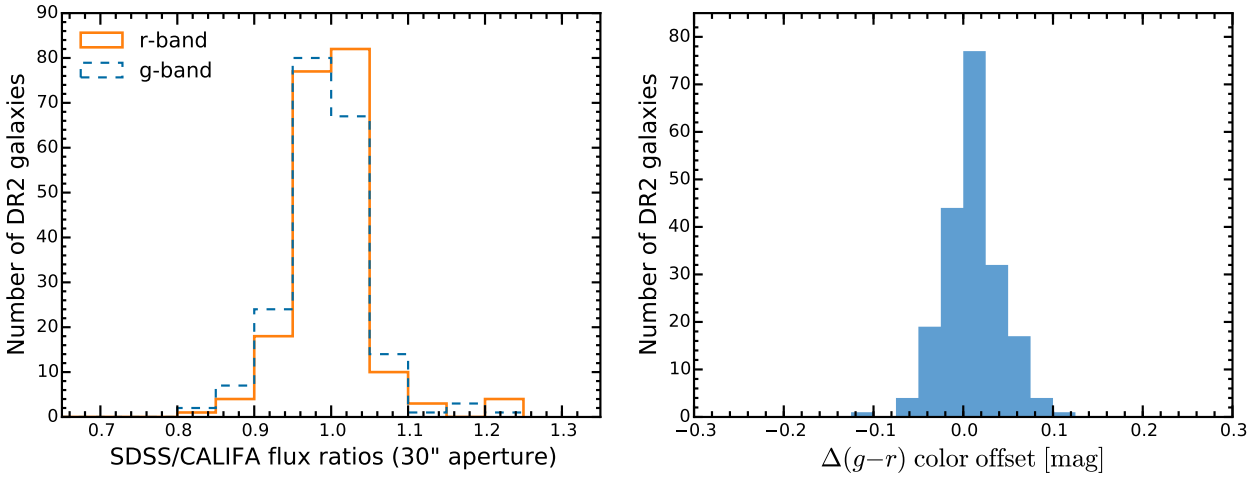

Fig. 14. *Left panel*: distribution of the 30″ aperture photometry scale factor between the SDSS DR7 images and recalibrated CALIFA data. We compare the photometry only for the *g* and *r* bands, which are both entirely covered by the V500 wavelength range. *Right panel*: distribution of the corresponding color offset between the SDSS DR7 images and the synthetic CALIFA broadband images.

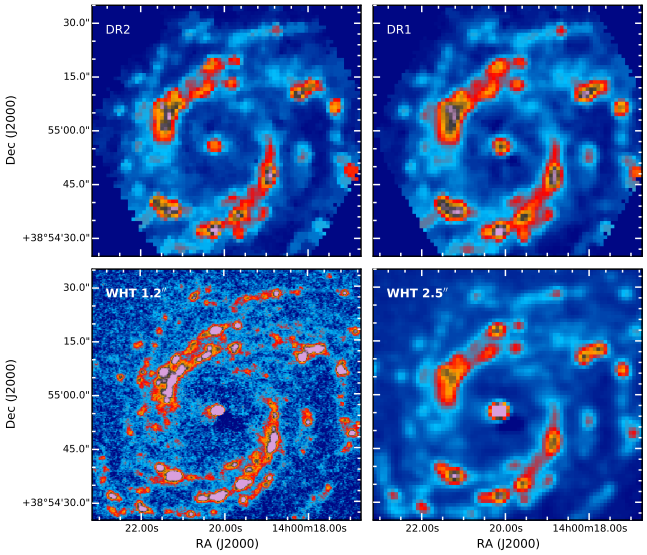

Fig. 15. DR2 spatial resolution comparison for NGC 5406 (ID 684). The *upper left panel* shows the DR2 image of the Hα map and the *upper right* the DR1 image. The *lower row* are Hα images taken with the 4.2 m *William Herschel* Telescope (Roque de los Muchachos Observatory, La Palma, Spain), using the AUXCAM detector (Sánchez-Menguiano et al., in prep.). The image, with an original resolution of 1.2″ (*bottom left*), has been degraded to a resolution of 2.5″ with the same pixel scale (*bottom right*) and the FoV has been reduced to match exactly the same WCS coordinates as CALIFA.

If any CALIFA data sets are available given the search parameters, they are listed in the follwing web page and can be selected to be downloaded. The download process requests a target directory on the local machine to store the data, after the downloading option is selected. The CALIFA data are delivered as fully reduced datacubes in FITS format separately for each of the two CALIFA spectral settings, i.e., the V500 and V1200 setup. Each DR2 data set is uniquely identified by their file name, *GALNAME*`.V1200.rscube.fits.gz` and *GALNAME*`.V500.rscube.fits.gz` for the V1200 and V500 setup respectively, where *GALNAME* is the name of the CALIFA galaxy listed in Table 1.

All the QC tables discussed throughout this article are also distributed in CSV and FITS-table formats in the same webpage. In addition, we distribute the more relevant tables discussed in W14 regarding the characterization of the MS, using similar formats. These tables could be useful in further science explorations of the cubes.

7.2. Virtual observatory services

CALIFA data is also available through several Virtual Observatory (VO) facilities:

1. The FITS files of the full cubes are accessible through GAVO's ObsCore (Louys et al. 2011) service, which is part of the TAP (Dowler et al. 2011) service[19]. ObsCore provides a homogeneous description of observational data products of all kinds and thus allows for a global data set discovery. The system already supports the upcoming IVOA DataLink standard for performing cutouts and similar server-side operations.
2. At the same TAP endpoint, the `califadr2.cubes` and `califadr2.objects` tables enable queries versus CALIFA-specific metadata, and in particular, the quality control parameters given in Tables 6 and 7.
3. Individual, cutout spectra can be located and retrieved from the CALIFA SSA service[20]; advanced SSAP clients like Splat (Draper 2014) also support server-side spectral cutouts on this service via a DataLink prototype.
4. The spaxels can also be queried in database tables via GAVO's TAP service mentioned above (the tables are called `califadr2.fluxv500` and `califadr2.fluxv1200`).

An overview of VO-accessible resources generated from CALIFA, possibly updated from what is reported here, is available at `http://dc.g-vo.org/browse/califa/q2`. This page also gives some usage scenarios for CALIFA VO resources.

8. Summary

In this article we have presented the main characteristics of the second public data release of the Calar Alto Legacy Integral

[19] `http://dc.g-vo.org/tap`
[20] SSA access URL `http://victor:8080/califa/q2/s/info`

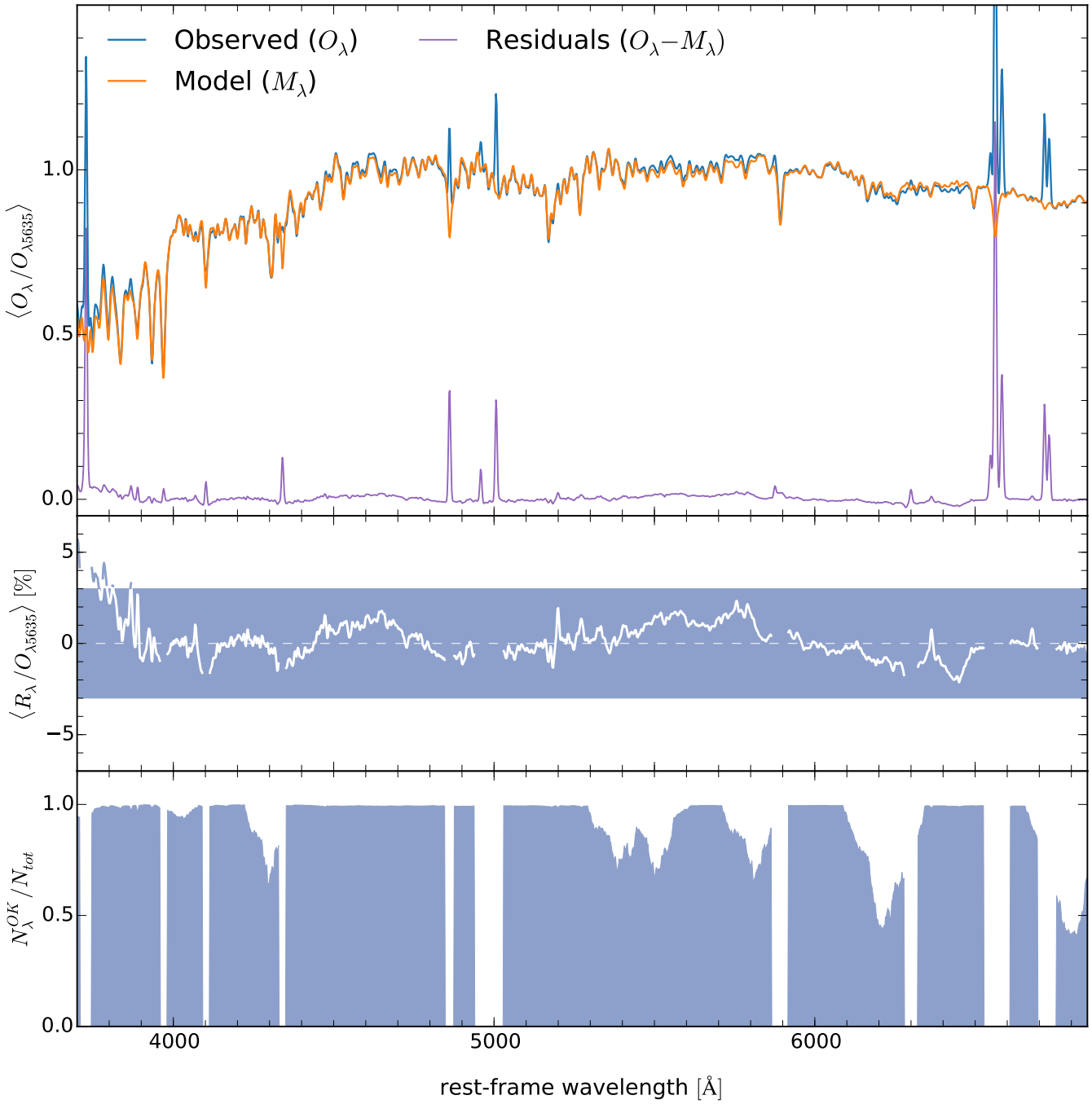

Fig. 16. Statistics of the spectral residuals (compare to Fig. 13 of Cid Fernandes et al. 2014). *Top*: the mean normalized spectrum of 170670 bins from 200 galaxies. The mean STARLIGHT fit is overplotted in orange, while the mean residual is plotted at the bottom of the panel (purple). *Middle*: zoom of the residual spectrum, with emission lines removed for clarity. The shaded rectangle encompasses the ±3% area. *Bottom*: fraction of the bins contributing to the statistics at each λ.

Field Area (CALIFA) survey. This data release comprises 200 galaxies (400 datacubes) containing more than 1.5 million spectra[21], covering a wide range of masses, morphological types, colors, etc. This subset of randomly selected objects comprises a statistically representative sample of the galaxies in the Local Universe. The CALIFA DR2 provides science-grade and quality-checked, integral-field spectroscopy publicly distributed to the community[22].

We described in detail the main quality parameters analyzed in the validation process, which are provided to the users with complete tables to select the objects for their science cases. We reduced the data using a new version of the pipeline (V1.5), which considerably improves the quality of the data in terms of: (i) the spatial resolution; (ii) the covariance between the adjacent spectra; and (iii) the spectrophotometric calibration.

Compared with other ongoing major surveys, CALIFA offers a similar spatial resolution. The PSF of the datacubes has been improved considerably, with a mean value of ~2.5″ (Sect.6.4.2), similar to SAMI (Sharp et al. 2015). In the case of MaNGA, the

[21] Obtained from ~400 000 independent spectra from the RSS files.
[22] http://califa.caha.es/DR2

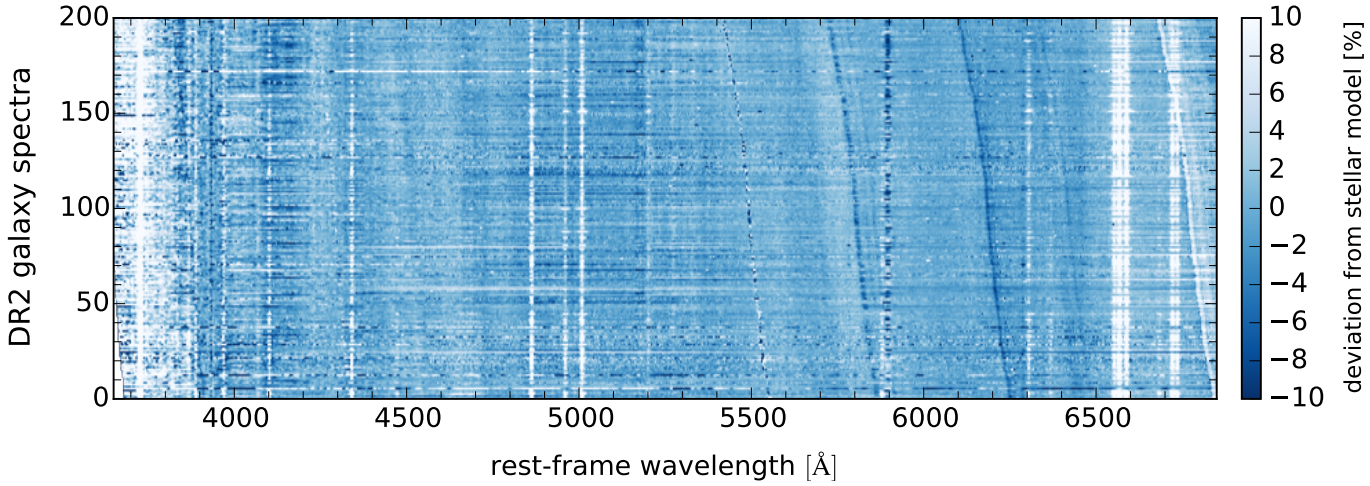

Fig. 17. Relative spectral deviations, $(O_\lambda - M_\lambda)/O_\lambda$, where O and M denote the observed and the model spectra, for the nuclear regions of all DR2 galaxies, vertically sorted by redshift. Unlike in Fig. 16, emission lines and bad pixels are not masked in this plot. Systematic deviations from the STARLIGHT model appear as vertical stripes (rest-frame mismatches, e.g., imperfect stellar model or emission lines), while slanted stripes trace observed-frame mismatches (e.g., imperfect sky model). Compare to Fig. 16 of H13.

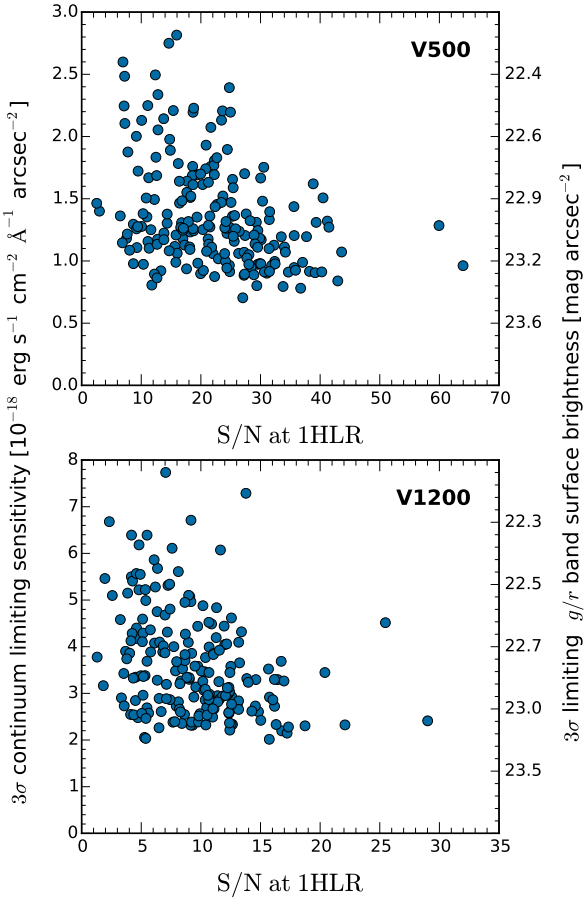

Fig. 18. Limiting 3σ continuum sensitivity per spaxel and spectral resolution element as a function of the average continuum S/N at the half-light radius (HLR). The corresponding broadband surface brightness limits in r (V500) and g (V1200) are indicated on the right y-axis. The limiting continuum sensitivity and the S/N were computed from the median signal and noise in the wavelength region 4480–4520 Å and 5590–5680 Å for the V1200 and V500 data, respectively.

combination of an average seeing at the Sloan Telescope (~1.5″) and the fiber size (2″), would produce a PSF with a very similar FWHM. The redshift range of SAMI and MaNGA surveys is considerably larger than CALIFA, reaching up to $z \sim 0.1$. This means that only galaxies at the lowest redshift range in SAMI and MaNGA will offer a similar physical resolution. On the other hand, the spatial coverage of CALIFA is larger than any of those surveys, both in physical and in projected terms (five times larger than SAMI and two times larger than MaNGA). In summary, CALIFA is the survey that samples the galaxies with the largest number of spatial elements for the largest FoV. The penalty for this wider coverage is the lower number of galaxies observed (6 times lower than SAMI and 15 times lower than MaNGA), and a lower spectral resolution of CALIFA over the full wavelength range.

The dataset analysed so far have produced significant advances in our knowledge of the stellar and gas composition in galaxies, their kinematical structure, and the overall star formation history and chemical enrichment (as reviewed in the introduction). We have uncovered new local relations within galaxies, tightly connected to the global relations described using classical spectroscopic surveys. With this new DR, we open to the astronomical community the possibility to futher analyze the spatially resolved properties of galaxies, presenting a panoramic view of the galaxy properties.

Acknowledgements. CALIFA is the first legacy survey being performed at Calar Alto. The CALIFA collaboration would like to thank the IAA-CSIC and MPIA-MPG as major partners of the observatory, and CAHA itself, for the unique access to telescope time and support in manpower and infrastructures. The CALIFA collaboration thanks also the CAHA staff for the dedication to this project. R.G.B., R.G.D., and E.P. are supported by the Spanish *Ministerio de Ciencia e Innovación* under grant AYA2010-15081. S.Z. is supported by the EU Marie Curie Integration Grant "SteMaGE" Nr. PCIG12-GA-2012-326466 (Call Identifier: FP7-PEOPLE-2012 CIG). J.F.B. acknowledges support from grants AYA2010-21322-C03-02 and AIB-2010-DE-00227 from the Spanish Ministry of Economy and Competitiveness (MINECO), as well as from the FP7 Marie Curie Actions of the European Commission, via the Initial Training Network DAGAL under REA grant agreement number 289313. Support for L.G. is provided by the Ministry of Economy, Development, and Tourism's Millennium Science Initiative through grant IC12009, awarded to The Millennium Institute of Astrophysics, M.A.S. L.G. also acknowledges support by CONICYT through FONDECYT grant 3140566. A.G. acknowledges support from the FP7/2007-2013 under grant agreement n. 267251 (AstroFIt). J.M.G. acknowledges support from the Fundação para a Ciência e a Tecnologia (FCT) through the Fellowship SFRH/BPD/66958/2009 from FCT (Portugal) and research grant PTDC/FIS-AST/3214/2012. RAM was funded by the Spanish programme of International Campus of Excellence Moncloa (CEI). J.M.A. acknowledges support from the

European Research Council Starting Grant (SEDmorph; P.I. V. Wild). I.M., J.M. and A.d.O. acknowledge the support by the projects AYA2010-15196 from the Spanish Ministerio de Ciencia e Innovación and TIC 114 and PO08-TIC-3531 from Junta de Andalucía. AMI acknowledges support from Agence Nationale de la Recherche through the STILISM project (ANR-12-BS05-0016-02). M.M. acknowledges financial support from AYA2010-21887-C04-02 from the Ministerio de Economía y Competitividad. P.P. is supported by an FCT Investigador 2013 Contract, funded by FCT/MCTES (Portugal) and POPH/FSE (EC). P.P. acknowledges support by FCT under project FCOMP-01-0124-FEDER-029170 (Reference FCT PTDC/FIS-AST/3214/2012), funded by FCT-MEC (PIDDAC) and FEDER (COMPETE). T.R.L. thanks the support of the Spanish Ministerio de Educación, Cultura y Deporte by means of the FPU fellowship. PSB acknowledges support from the Ramón y Cajal program, grant ATA2010-21322-C03-02 from the Spanish Ministry of Economy and Competitiveness (MINECO). C.J.W. acknowledges support through the Marie Curie Career Integration Grant 303912. V.W. acknowledges support from the European Research Council Starting Grant (SEDMorph P.I. V. Wild) and European Career Re-integration Grant (Phiz-Ev P.I. V. Wild). Y.A. acknowledges financial support from the *Ramón y Cajal* programme (RyC-2011-09461) and project AYA2013-47742-C4-3-P, both managed by the *Ministerio de Economía y Competitividad*, as well as the "Study of Emission-Line Galaxies with Integral-Field Spectroscopy" (SELGIFS) programme, funded by the EU (FP7-PEOPLE-2013-IRSES-612701) within the Marie-Sklodowska-Curie Actions scheme. We thank the referee David Wilman for very useful comments that improved the presentation of the paper.

Appendix A: Computing the error spectrum for co-added spectra

Some science cases require a minimum S/N in the spectra, especially in the outer parts of the galaxies. This is achieved by spatially coadding spaxels in the datacubes, often by means of an adaptive binning method, such as the Voronoi-binning scheme, implemented for optical IFS data by Cappellari & Copin (2003). However, the final error spectrum of the coadded spectra cannot be simply quadratically summed since the spectra are not independent of each other. As described in Sect. 4.2, we adopt an inverse-distance weighted image reconstruction which, like many other image resampling schemes, introduces a correlation between spaxels in the final datacube. In Sect. 4.3, we provide an equation that relates the analytically propagated error recorded in the datacubes with the final "real" error of the coadded spectrum[23].

Let B be a bin of size N spectra, i.e., we want to coadd N spectra and compute the corresponding error spectrum for that bin. Since we are adding the flux to obtain an integrated spectrum, first we need to add the errors of each individual spectra in quadrature,

$$\epsilon_B^2 = \sum_{k=1}^{N} \epsilon_k^2 \, .$$

This would be the error spectrum of the bin B if the spaxels where completely independent. To account for the correlated noise, we simply need to multiply by the corresponding "correlation factor" (Eq. (1)) for a given number of spectra in a particular bin,

$$\epsilon_{\mathrm{real},B}^2 = \beta(N)^2 \times \epsilon_B^2,$$

when the bin B contains a large number of spaxels ($N \gtrapprox 80$), the use of Eq. (1) is not recommended. In this case, the ERRWEIGHT HDU extension of the CALIFA FITS file datacube should be used (see Table 2) as a correction factor for each spaxel,

$$\epsilon_B^2 = \sum_{k=1}^{N} w_k^2 \times \epsilon_k^2 \, ,$$

where w_k is the error weight of each individual spaxel. The error weighting factor is estimated for each pixel such that the formal error of the coadded spectrum of the entire cube is identical at the obtained by coadding the individual 993 fibers of the RSS.

[23] See also Sects. 3.2 and 3.3 of Cid Fernandes et al. (2013) for a detailed disquisition on error propagation and correlated noise for IFS.

References

Abazajian, K. N., Adelman-McCarthy, J. K., Agüeros, M. A., et al. 2009, ApJS, 182, 543
Aceituno, J. 2004, Calar Alto Newsletter No. 8, http://www.caha.es/newsletter/news04b/Aceituno/Newsletter.html
Aguerri, J. A. L., Méndez-Abreu, J., Falcón-Barroso, J., et al. 2015, 576, A102
Alonso-Herrero, A., Rosales-Ortega, F. F., Sánchez, S. F., et al. 2012, MNRAS, 425, L46
Barrera-Ballesteros, J. K., Falcón-Barroso, J., García-Lorenzo, B., et al. 2014, A&A, 568, A70
Bershady, M. A., Verheijen, M. A. W., Swaters, R. A., et al. 2010, ApJ, 716, 198
Blanton, M. R., Schlegel, D. J., Strauss, M. A., et al. 2005, AJ, 129, 2562
Bryant, J. J., Owers, M. S., Robotham, A. S. G., et al. 2015, MNRAS, 447, 2857
Cappellari, M. & Copin, Y. 2003, MNRAS, 342, 345
Cappellari, M., Emsellem, E., Krajnović, D., et al. 2011, MNRAS, 413, 813
Cid Fernandes, R., Mateus, A., Sodré, L., Stasińska, G., & Gomes, J. M. 2005, MNRAS, 358, 363
Cid Fernandes, R., Pérez, E., García Benito, R., et al. 2013, A&A, 557, A86
Cid Fernandes, R., González Delgado, R. M., García Benito, R., et al. 2014, A&A, 561, A130
Croom, S. M., Lawrence, J. S., Bland-Hawthorn, J., et al. 2012, MNRAS, 421, 872
Davies, R. L., Kewley, L. J., Ho, I.-T., & Dopita, M. A. 2014, MNRAS, 444, 3961
De Geyter, G., Baes, M., Camps, P., et al. 2014, MNRAS, 441, 869
Dowler, P., Rixon, G., & Tody, D. 2011, ArXiv e-prints [arXiv:1110.0497]
Draper, P. W. 2014, Astrophysics Source Code Library, [record ascl: 1402.007]
Erwin, P. 2015, ApJ, 799, 226
Fruchter, A. S. & Hook, R. N. 2002, PASP, 114, 144
Galbany, L., Stanishev, V., Mourão, A. M., et al. 2014, A&A, 572, A38
García-Lorenzo, B., Márquez, I., Barrera-Ballesteros, J. K., et al. 2015, A&A, 573, A59
González Delgado, R. M., Cerviño, M., Martins, L. P., Leitherer, C., & Hauschildt, P. H. 2005, MNRAS, 357, 945
González Delgado, R. M., Cid Fernandes, R., García-Benito, R., et al. 2014a, ApJ, 791, L16
González Delgado, R. M., Pérez, E., Cid Fernandes, R., et al. 2014b, A&A, 562, A47
Greisen, E. W., & Calabretta, M. R. 2002, A&A, 395, 1061
Holwerda, B. W., & Keel, W. C. 2013, A&A, 556, A42
Horne, K. 1986, PASP, 98, 609
Husemann, B., Kamann, S., Sandin, C., et al. 2012, A&A, 545, A137
Husemann, B., Jahnke, K., Sánchez, S. F., et al. 2013, A&A, 549, A87 (H13)
Iglesias-Páramo, J., Vílchez, J. M., Galbany, L., et al. 2013, A&A, 553, L7
Kehrig, C., Monreal-Ibero, A., Papaderos, P., et al. 2012, A&A, 540, A11
Kelz, A., Verheijen, M. A. W., Roth, M. M., et al. 2006, PASP, 118, 129
Law, D. R., & MaNGA Team 2014, Am. Astron. Soc. Meet. Abstr., 223, 254.31
Louys, M., Bonnarel, F., Schade, D., et al. 2011, ArXiv e-prints [arXiv:1111.1758]
Marino, R. A., Rosales-Ortega, F. F., Sánchez, S. F., et al. 2013, A&A, 559, A114
Mármol-Queraltó, E., Sánchez, S. F., Marino, R. A., et al. 2011, A&A, 534, A8
Martínez-García, E. E., Puerari, I., Rosales-Ortega, F. F., et al. 2014, ApJ, 793, L19
Mast, D., Rosales-Ortega, F. F., Sánchez, S. F., et al. 2014, A&A, 561, A129
Papaderos, P., Gomes, J. M., Vílchez, J. M., et al. 2013, A&A, 555, L1
Pérez, E., Cid Fernandes, R., González Delgado, R. M., et al. 2013, ApJ, 764, L1
Rosales-Ortega, F. F., Kennicutt, R. C., Sánchez, S. F., et al. 2010, MNRAS, 405, 735
Rosales-Ortega, F. F., Díaz, A. I., Kennicutt, R. C., & Sánchez, S. F. 2011, MNRAS, 415, 2439
Rosales-Ortega, F. F., Sánchez, S. F., Iglesias-Páramo, J., et al. 2012, ApJ, 756, L31
Roth, M. M., Kelz, A., Fechner, T., et al. 2005, PASP, 117, 620
Sánchez, S. F., Cardiel, N., Verheijen, M. A. W., Pedraz, S., & Covone, G. 2007, MNRAS, 376, 125
Sánchez, S. F., Thiele, U., Aceituno, J., et al. 2008, PASP, 120, 1244

Sánchez, S. F., Rosales-Ortega, F. F., Kennicutt, R. C., et al. 2011, MNRAS, 410, 313
Sánchez, S. F., Kennicutt, R. C., Gil de Paz, A., et al. 2012a, A&A, 538, A8 (S12)
Sánchez, S. F., Rosales-Ortega, F. F., Marino, R. A., et al. 2012b, A&A, 546, A2
Sánchez, S. F., Rosales-Ortega, F. F., Jungwiert, B., et al. 2013, A&A, 554, A58
Sánchez, S. F., Rosales-Ortega, F. F., Iglesias-Páramo, J., et al. 2014, A&A, 563, A49
Sánchez-Blázquez, P., Rosales-Ortega, F. F., Méndez-Abreu, J., et al. 2014, A&A, 570, A6
Sandin, C., Schönberner, D., Roth, M. M., et al. 2008, A&A, 486, 545
Sharp, R., Allen, J. T., Fogarty, L. M. R., et al. 2015, MNRAS, 446, 1551
Singh, R., van de Ven, G., Jahnke, K., et al. 2013, A&A, 558, A43
Vazdekis, A., Sánchez-Blázquez, P., Falcón-Barroso, J., et al. 2010, MNRAS, 404, 1639
Verheijen, M. A. W., Bershady, M. A., Andersen, D. R., et al. 2004, Astron. Nachr., 325, 151
Viironen, K., Sánchez, S. F., Marmol-Queraltó, E., et al. 2012, A&A, 538, A144
Walcher, C. J., Wisotzki, L., Bekeraité, S., et al. 2014, A&A, 569, A1 (W14)
Wild, V., Rosales-Ortega, F., Falcón-Barroso, J., et al. 2014, A&A, 567, A132
Wilson, E. B. 1927, J. Am. Statis. Assoc., 22, 209

[1] Instituto de Astrofísica de Andalucía (IAA/CSIC), Glorieta de la Astronomía s/n Aptdo. 3004, 18080 Granada, Spain, e-mail: rgb@iaa.es
[2] INAF–Osservatorio Astrofisico di Arcetri, Largo Enrico Fermi 5, 50125 Firenze, Italy
[3] Instituto de Astronomía, Universidad Nacional Autonóma de México, A.P. 70-264, 04510 México, D.F., Mexico
[4] European Southern Observatory, Karl-Schwarzschild-Str. 2, 85748 Garching b. München, Germany
[5] Departamento de Física, Universidade Federal de Santa Catarina, PO Box 476, 88040-900 Florianópolis, SC, Brazil
[6] Departamento de Astrofísica y CC. de la Atmósfera, Universidad Complutense de Madrid, 28040 Madrid, Spain
[7] Australian Astronomical Observatory, PO Box 915, North Ryde, NSW 1670, Australia
[8] Instituto de Astrofísica de Canarias, vía Láctea s/n, 38205 La Laguna, Tenerife, Spain
[9] Departamento de Astrofísica, Universidad de La Laguna, 38205 La Laguna, Tenerife, Spain
[10] Millennium Institute of Astrophysics, Universidad de Chile, Santiago, Chile
[11] Departamento de Astronomía, Universidad de Chile, Casilla 36-D, Santiago, Chile
[12] School of Physics and Astronomy, University of St Andrews, SUPA, North Haugh, KY16 9SS, St Andrews, UK
[13] Kapteyn Astronomical Institute, University of Groningen, Postbus 800, 9700 AV Groningen, The Netherlands
[14] Max-Planck-Institut für Astronomie, Königstuhl 17, 69117 Heidelberg, Germany
[15] CEI Campus Moncloa, UCM-UPM, Departamento de Astrofísica y CC. de la Atmósfera, Facultad de CC. Físicas, Universidad Complutense de Madrid, Avda. Complutense s/n, 28040 Madrid, Spain
[16] Instituto de Cosmologia, Relatividade e Astrofísica – ICRA, Centro Brasileiro de Pesquisas Físicas, Rua Dr.Xavier Sigaud 150, CEP 22290-180, Rio de Janeiro, RJ, Brazil
[17] Departamento de Física Teórica, Facultad de Ciencias, Universidad Autónoma de Madrid, 28049 Madrid, Spain
[18] Leibniz-Institut für Astrophysik Potsdam (AIP), An der Sternwarte 16, 14482 Potsdam, Germany
[19] Sydney Institute for Astronomy, School of Physics, University of Sydney, NSW 2006, Australia
[20] Astronomisches Institut, Ruhr-Universität Bochum, Universitätsstr. 150, 44801 Bochum, Germany
[21] RUB Research Department Plasmas with Complex Interactions, Germany
[22] Universität Heidelberg, Zentrum für Astronomie, Astronomisches Rechen-Institut, Mönchhofstraße 12-14, 69120 Heidelberg, Germany
[23] Departamento de Física Teórica y del Cosmos, University of Granada, Facultad de Ciencias (Edificio Mecenas), 18071 Granada, Spain
[24] Dark Cosmology Center, University of Copenhagen, Niels Bohr Institute, Juliane Maries Vej 30, 2100 Copenhagen, Denmark
[25] Instituto de Astrofísica e Ciências do Espaço, Universidade do Porto, CAUP, Rua das Estrelas, 4150-762 Porto, Portugal
[26] Department of Physics, Royal Military College of Canada, PO box 17000, Station Forces, Kingston, Ontario, K7K 7B4, Canada
[27] Centro Astronómico Hispano Alemán de Calar Alto (CSIC-MPG), C/ Jesús Durbán Remón 2-2, 4004 Almería, Spain
[28] Department of Physics 4-181 CCIS, University of Alberta, Edmonton AB T6G 2E1, Canada
[29] Institute of Astronomy, University of Cambridge, Madingley Road, Cambridge CB3 0HA, UK
[30] Department of Physics and Astronomy, Macquarie University, NSW 2109, Australia
[31] CIEMAT, Avda. Complutense 40, 28040 Madrid, Spain
[32] GEPI, Observatoire de Paris, CNRS, Université Paris Diderot, Place Jules Janssen, 92190 Meudon, France
[33] Instituto Universitario Carlos I de Física Teórica y Computacional, Universidad de Granada, 18071 Granada, Spain
[34] Landessternwarte, Zentrum für Astronomie der Universität Heidelberg, Königstuhl 12, 69117 Heidelberg, Germany
[35] Instituto Nacional de Astrofísica, Óptica y Electrónica, Luis E. Erro 1, 72840 Tonantzintla, Puebla, Mexico
[36] CENTRA – Centro Multidisciplinar de Astrofísica, Instituto Superior Técnico, Av. Rovisco Pais 1, 1049-001 Lisbon, Portugal
[37] Department of Physics, Chemistry and Biology, IFM, Linköping University, 581 83 Linköping, Sweden
[38] Departamento de Astronomía, Universidad de Guanajuato, Apartado Postal 144, 36000 Guanajuato, Mexico
[39] University of Vienna, Department of Astrophysics, Türkenschanzstr. 17, 1180 Vienna, Austria
[40] Centro de Astrobiología (CSIC-INTA), Depto. Astrofísica, ESAC Campus, 28691 Villanueva de la Cañada, Madrid, Spain